INFORMATION TO USERS

This manuscript has been reproduced from the microfilm master. UMI films the text directly from the original or copy submitted. Thus, some thesis and dissertation copies are in typewriter face, while others may be from any type of computer printer.

The quality of this reproduction is dependent upon the quality of the copy submitted. Broken or indistinct print, colored or poor quality illustrations and photographs, print bleedthrough, substandard margins, and improper alignment can adversely affect reproduction.

In the unlikely event that the author did not send UMI a complete manuscript and there are missing pages, these will be noted. Also, if unauthorized copyright material had to be removed, a note will indicate the deletion.

Oversize materials (e.g., maps, drawings, charts) are reproduced by sectioning the original, beginning at the upper left-hand corner and continuing from left to right in equal sections with small overlaps.

Photographs included in the original manuscript have been reproduced xerographically in this copy. Higher quality 6" x 9" black and white photographic prints are available for any photographs or illustrations appearing in this copy for an additional charge. Contact UMI directly to order.

EXTRACTION OF POINT DEFECT PARAMETERS BY QUANTITATIVE TRANSMISSION ELECTRON MICROSCOPY

By

SUSHIL BHARATAN

A DISSERTATION PRESENTED TO THE GRADUATE SCHOOL
OF THE UNIVERSITY OF FLORIDA IN PARTIAL FULFILLMENT
OF THE REQUIREMENTS FOR THE DEGREE OF
DOCTOR OF PHILOSOPHY

UNIVERSITY OF FLORIDA

1999

UMI®

Copyright 1999

by

Sushil Bharatan

ACKNOWLEDGMENTS

I would like to thank my advisor and committee chairman, Professor Kevin S. Jones, for his guidance and support. His enthusiasm for materials science and constant encouragement helped me maintain my motivation for this work and made my graduate student experience an extremely rewarding one. I would like to thank Professor Mark E. Law for patiently answering my seemingly never-ending questions, especially on FLOOPS and MARLOWE. I am also grateful to the other members of my supervisory committee - Professors R. T. DeHoff, S. J. Pearton, and C. R. Abernathy - for their advice and interest.

I am indebted to a number of people who helped supply the various samples used during the course of my research and assisted with sample preparation and analysis: Dr. Per Kringhoj, of the University of Aarhaus, for supplying the boron DSL samples; Lenny Rubin and John Jackson, of Eaton Corporation for carrying out most of the ion implants; Dr. Brad Herner for assistance with the RTA; and Dr. Fred Stevie of Lucent Technologies and Rich Brindos for doing the SIMS analysis.

I must also thank Dr. V. Krishnamoorthy and the students of the SWAMP Center, both past and present for their assistance and for making

iii

these past few years the best of my life. Lastly, I thank my parents for their continued support and love during a long college career.

TABLE OF CONTENTS

LIST OF FIGURES

viii

LIST OF TABLES

xii

Abstract of Dissertation Presented to the Graduate School
of the University of Florida in Partial Fulfillment of the
Requirements for the Degree of Doctor of Philosophy

EXTRACTION OF POINT DEFECT PARAMETERS BY QUANTITATIVE
TRANSMISSION ELECTRON MICROSCOPY

By

Sushil Bharatan

December 1999

Chairman: Professor Kevin S. Jones
Major Department: Materials Science and Engineering

Some of the key parameters used in process simulators are formation

energy, diffusivity, and the concentration of Si self-interstitials.

Unfortunately, experimental verification of these parameters is lacking. The

experiments presented in this dissertation are designed to improve our

understanding of the intrinsic point defect population and the role of the

surface on excess point defect behavior.

In order to compute the formation energy for self-interstitials in Si the

equilibrium concentration of self-interstitials at various temperatures has

been determined. Samples with thin (10 nm) buried boron layers were grown

by molecular beam epitaxy (MBE) and samples with a buried type II

dislocation loop layer were produced by Ge^+ ion implantation into undoped

MBE grown silicon. These samples were subjected to a 40 keV 1e14 /cm^2 Si$^+$ implant followed by anneals at temperatures between 685°C and 815°C for varying times. The loop layer was investigated to monitor the total flux of the interstitials as a function of time while the broadening of the boron layer profile was analyzed by secondary ion mass spectroscopy (SIMS) to determine the interstitial supersaturation. A combination of these two values provides an estimate of the equilibrium concentration of the Si interstitials. The results at various temperatures are then used to extract the enthalpy of formation of the Si interstitial.

For the formation of p-n junctions required for 0.18 μm and smaller technologies, the effects of implant damage on dopant diffusion and extended defect formation become increasingly important. Surface effects on transient enhanced diffusion (TED) and the formation and evolution of extended defects has been studied as a function of varying implant parameters like implant temperature, dose rate and the thickness of the amorphous layer formed. The results presented have been explained by proposing an empirical model for defect evolution.

CHAPTER 1
INTRODUCTION

1.1 Motivation and Objective

Ion implantation is the preferred technique for introducing dopants into silicon during the circuit fabrication process. Ion implantation is capable of precisely controlling the dopant concentrations and profiles and thus the junction depths in devices. However, implantation introduces large supersaturations of point defects. Upon annealing at elevated temperatures, these defects interact with the dopants and cause transient enhanced diffusion (TED),[1] which alters the expected shape of the dopant profile and thus the junction depth. With the scaling down of devices dimensions, the need to accurately predict and control dopant spatial distribution during fabrication becomes very important. Accurate prediction and simulation of dopant profiles requires quantitative knowledge of [2]:

1. the distribution of dopants and point defects (Si self-interstitials and Si vacancies) as a function of position within the sample after implantation.

2. the interaction of a dopant with point defects as well as extended defects and among dopants atoms themselves.

3. the properties of intrinsic defects, i.e., the interstitial and vacancy equilibrium concentration and their diffusivites, as well as their recombination coefficient.

1

4. effect of the surfaces and interfaces on point defect population which is becoming increasing important as implant energies are being scaled back leading to the dopant and damage profiles lying very close to the surface.

Therefore, in order to accurately describe the diffusion processes, a thorough understanding of the formation and evolution of point and extended defects, both intrinsic and caused during the processing steps (e.g., ion implantation) is required.

Over the years, considerable experimental work has been carried out to study the energetics and migration of point defects in silicon(Taylor et al.[3] and references therein), but direct methods of quantifying the point defect parameters are not possible. Consequently, most of the defect parameters, diffusivities, formation energies, recombination rates etc., are obtained by "reverse engineering" diffusion behaviors. The experiments mainly focus on determining the value of D_I by studying the diffusion or gettering of metals such as Au and Pt or by studying the effect of oxidation enhanced diffusion on defect evolution and dopant diffusion. The experiments have produced conflicting results leading to controversy regarding the point defect diffusivities and their equilibrium concentrations.

On the other hand, theory has made significant progress using first principles calculations[4,5] and atomistic simulations based on empirical interatomic potentials.[6] Despite this, the controversy remains regarding the fundamental properties of point defects. The experimental procedure

described in Chapter 3 of this dissertation is designed to verify these previous results. Accurate determination of these fundamental quantities would be a very significant development in this area of research.

For the formation of p-n junctions required for 0.18 µm and smaller device technologies, dopant ions will have to be implanted at ultra low energies ($\leq$ 5 keV).[2] At these low energies the projected range R_p of the implant is very small and the dopant and defect profiles are close to the surface. Thus the effect of the free surface on the interstitial supersaturation in the near surface region following an implant is an important although controversial topic since the influence of the surface on the formation and evolution of defects and hence on TED is not clear. Previous experiments have had contradictory results. Some authors contend that the size and density of defects reduce upon decreasing the distance between the surface and the end-of range (EOR) damage.[7] However the experimental methodology used is questionable since all the anneals were done at temperatures exceeding 1000°C, when the EOR loops are known to be in a dissolution regime. Other authors have shown that the presence of the free surface has no detectable effect on the nucleation and growth of the EOR defects,[8,9] but the closest distance between the surface and the EOR loops is about 300Å, which might not be small enough to see a significant effect.

But Agarwal et al.,[10] using low-energy Si^+ implants (1-5 keV) of constant dose ($1e14/cm^2$) into MBE grown boron doping superlattices (B-DSL)

and then annealing at temperatures ranging from 810 to 1050°C, showed that the boron TED decreased linearly with Si^+ ion implantation energy and concluded that this reduction is due to the increased annihilation of the excess interstitials at the surface. Thus the surface is seen as an efficient sink for the removal of point defects and this helps in obtaining shallower junctions. However changes in the implant energy lead to changes in the damage profile. Higher energy implants spread the damage over a larger volume and reduce the peak value of damage. Thus changes in the generation of extended defects and the effects of bulk recombination must be taken into account.

Contrary to the above results, a recent study by Moller et al.[11] on the dissolution of {311} defects as a function of depth showed that the surface does not appear to be a controlling sink for interstitials released from the {311} defects. In this study, a 40 keV, $1e14/cm^2$ Si^+ implant into a Czochralski grown wafer was annealed at 750°C at various times. It was found that the top of the {311} defects, which are closer to the surface (at ~ 500Å)did not dissolve faster than the bottom of the defects (at ~ 1500Å) despite their proximity to the surface.

The experimental results presented in Chapter 4 will investigate the effect of proximity of the silicon free surface to the end-of-range damage during the annealing cycle on the morphology of the EOR damage as well as TED of a deeper boron marker layer.

Thus, the goal of the experiments presented in this dissertation is to further our understanding of the intrinsic point defect population in silicon and the role of the surface on the evolution of excess point defects.

1.2 Transient Enhanced Diffusion

Ion implantation is the preferred method of introducing dopant atoms into the silicon lattice according to the National Semiconductor Technology Roadmap[2] and will continue to be so into the new millenium. During implantation the substrate is bombarded with incident ions at various energies. The ions lose kinetic energy due to elastic collisions with the silicon nuclei leading to the creation of point defects such as vacancies and interstitials. The damage created by the ion implantation process needs to be repaired by subjecting the silicon substrate to a post-implantation anneal. Depending on the implant conditions (energy, dose, and substrate temperature) the damage caused varies and several types of extended defects may be formed during the post-implantation anneal. These defects have been characterized by Jones and classified into types I, II, III, IV, and V.[12] Anomalous dopant diffusion was observed during annealing of ion implanted silicon, where the dopant profile did not follow the profile predicted by Fick's law, indicating a mechanism other than regular diffusion. This phenomenon, where the dopant diffusivity is several orders of magnitude higher than the intrinsic value is know as Transient Enhanced Diffusion. It has been

suggested that this TED of the dopant is due to the presence of excess interstitials , which according to the +1 model,[13] is equal to the implant dose (for sub-amorphizing implants).

1.3 Point Defects in Silicon

Point defects in silicon can be categorized as:

1. Native point defects that exist in a pure silicon lattice, and

2. Impurity related point defects that are associated with foreign impurities and dopants.

For the purpose of this discussion, we shall limit ourselves to native point defects. The native point defects of interest in silicon are: vacancy, interstitial, and interstitialcy. The vacancy is an empty lattice site whereas the interstitial, also known as the self-interstitial, is a silicon atom present at an interstitial position. An interstitialcy defect consists of two atoms in non-substitutional positions configured about a single substitutional lattice site. Both the interstitial and the interstitialcy are referred to as interstitials or self-interstitials and the distinction between them is usually ignored.

1.3.1 Dopant Diffusion Mechanisms

Diffusion of a dopant in the silicon lattice can be viewed as atomic movement of the dopant atom in the crystal by vacancies or self-interstitials.

Figure 1.1 shows some common atomic diffusion models in a lattice using a simplified two-dimensional crystal structure.

The vacancy model is based on the assumption that the diffusion coefficient on the dopant is dominated by the interaction of the dopant with vacancies. Occasionally a host atom will acquire sufficient energy to leave its lattice site and move to an interstitial site thus creating a vacancy. When a neighboring dopant atom moves to this vacancy site, the mechanism is called diffusion via a vacancy. Studies on the effect of oxidation on stacking fault growth kinetics and Au diffusion in silicon have indicated that vacancies alone do not control diffusion, but that Si self-interstitials also play a vital role. If an interstitial dopant atom moves from one place to another without occuping a lattice site, the mechanism is known as interstitial diffusion. An atom smaller than the host atom often moves interstitially. A variant of the interstitial mechanism is the interstitialcy or "kickout" mechanism. This process involves the kickout of a dopant atom by a Si self-interstial. The dopant atom now diffuses to another lattice siteand kicks out the lattice silicon atom. As it is impossible to distinguish between the interstitial and the iterstitialcy mechanisms, they are both referred to as "interstitial" mechanism.

1.3.2 Point Defects and Dopant Diffusion

The diffusion of dopant atoms in silicon can be described by the Arrhenius expression:

$$D_A = D_0 \exp(-E_A/k_B T) \tag{1}$$

where D_A is the dopant diffusivity, D_0 is the pre-exponential factor and E_A is the activation energy ($\sim$ 4 to 5 eV). Even though it is generally agreed that dopant atoms diffuse through the interactions with self-interstitials and vacancies, the relative contribution from each mechanism is still a matter of discussion. Dopants that occupy substitutional sites in the silicon lattice can move only through the interaction with defects. For a dopant atom A, the diffusivity can be expressed as

$$D_A = D_{AI} + D_{AV} \tag{2}$$

where D_{AI} and D_{AV} are the interstitial and vacancy components for diffusion. If D_A is defined to be the diffusivity under non-equilibrium point defect concentrations and D_A^* is the equilibrium diffusivity, then

$$\frac{D_A}{D_A^*} = \frac{D_{AI}}{D_A^*} + \frac{D_{AV}}{D_A^*} \tag{3}$$

This can be expressed as

$$\frac{D_A}{D_A^*} = \frac{D_{AI}^*}{D_A^*} \frac{D_{AI}}{D_{AI}^*} + \frac{D_{AV}^*}{D_A^*} \frac{D_{AV}}{D_{AV}^*} \tag{4}$$

The terms $\dfrac{D_{AI}^*}{D_A^*}$ and $\dfrac{D_{AV}^*}{D_A^*}$ are the fraction of dopant A's diffusivity due to the interstitial and the vacancy mechanism respectively. By defining

$\dfrac{D_{AI}^*}{D_A^*} = f_{AI}$ and $\dfrac{D_{AV}^*}{D_A^*} = f_{AV}$ equation (4) becomes

$$\frac{D_A}{D_A^*} = f_{AI} \frac{D_{AI}}{D_{AI}^*} + f_{AV} \frac{D_{AV}}{D_{AV}^*} \qquad (5)$$

and also, $f_{AI} + f_{AV} = 1$

Since $\dfrac{D_{AI}}{D_{AI}^*}$ and $\dfrac{D_{AV}}{D_{AV}^*}$ are proportional to the relative concentration of each

species of point defect, equation (5) can be rewritten as

$$\frac{D_A}{D_A^*} = f_{AI} \frac{C_I}{C_I^*} + f_{AV} \frac{C_V}{C_V^*} \qquad (6)$$

where C_I and C_V are the concentrations of interstitials and vacancies under

non-equilibrium conditions, and C_I^* and C_V^* are the quantities under

intrinsic, equilibrium conditions.

It is generally believed that antimony diffusion is dominated by a

vacancy mechanism ($f_{SbV} \sim 1$) whereas boron and phosphorus diffuse

predominantly by an interstitial mechanism ($f_{BI} \sim 0.8$ to 1 and $f_{PI} \sim 1$).[14]

Antimony, boron and phosphorus doping superlattices can therefore be used

as indicators of the relative population of point defects by observing changes

in their diffusivities as a function of depth.

1.3.3 Equilibrium Concentration / Diffusivity of Point Defects:

Despite numerous attempts, no experimental method has definitely

measured the equilibrium concentrations of vacancies and interstitials in

silicon, or even the enthalpies of formation.

In the presence of interstitials and vacancies the self diffusion coefficient D^{SD} is given by:

$$D^{SD} = D_I C_I^* + D_V C_V^* \qquad (7)$$

Knowledge of D^{SD} does not give information on the relative contributions of self-interstitials and vacancies. To date, numerous experiments have tried to determine $D_I C_I^*$ and $D_V C_V^*$. The $D_I C_I^*$ value given by

$$D_I C_I^* = 914 \exp(-4.84/k_B T) \text{ cm}^2/\text{s} \qquad (8)$$

(where C_I^* is normalized to 5×10^{22} cm^{-3})

is considered to be a reliable and accurate quantity since two different types of experimental measurements involving in-diffusion of impurities (Au, Pt etc.[15,16]) and tracer diffusion[17] give consistent results. On the other hand, very few experiments have attempted to measure the $D_V C_V^*$ product and the published values are unreliable.[3] In addition, though the $D_I C_I^*$ value is established the individual terms D_I and C_I^* are not known. In the literature, there is a large discrepancy between measured D_I values with published values varying by upto six orders of magnitude at 800°C (Figure 1.2). Also, substantial differences have been found between samples grown at different research facilities,[18] thus opening up the need for an experimental procedure that eliminates material-dependent properties.

1.4 Extended Defects in Silicon

As mentioned earlier, a major disadvantage of ion implantation is the damage introduced by the energetic ions and the need for post-implantation annealing to activate the dopant. Different types of extended defects form after annealing, depending on both the implant and the annealing conditions. If the residual implantation damage is not in the form of submicroscopic clusters, it can be imaged in the TEM. A classification scheme has been developed for the secondary defects which arise or develop during annealing of implanted silicon.[12,19] This classification scheme successfully groups all secondary defects into five types based upon the origin of the damage as detailed schematically in Figure 1.3. The categories are closely related to the morphology and position of the amorphous layer (if any) resulting from implantation.

1.4.1 Type I: Sub-amorphization Defects

When the implant damage is not sufficient to turn the silicon surface into a continuous amorphous layer, sub-amorphization defects form during the subsequent annealing. These defects arise from a supersaturation of point defects due to the non-conservative nature of the implantation process. They form around the projected range of the implanted ions, where the supersaturation level is the highest[20,21]. These defects have two common forms: rod-like {311} defects and dislocation loops.

1.4.2 Type II: End-of Range Defects

When the silicon surface has been amorphized during implantation, end-of-range defects form just below the amorphous crystalline interface upon annealing. End-of-range defects may consist of both dislocation loops and {311} defects if the annealing temperature is low. The formation and evolution of the defects have been studied in great detail by various researchers[22],[23]. Due to the relevance of both dislocation loops and {311} defects to this research, they will be discussed in greater detail in the next two sections

1.4.2.1 End-of range dislocation loops

Extrinsic dislocation loops (also known as type II loops or EOR loops) are metastable defects consisting of interstitial silicon atoms. These defects can arise from amorphizing implants i.e. the threshold damage density for silicon is overcome by selecting the proper implant species, dose, energy and temperature.[12] The crystalline region adjacent to the amorphous/crystalline interface is presumed to be saturated with excess interstitials recoiled from the amorphous region. During a recrystallizing anneal the loops form near the end-of-range (i.e., just below the amorphous/crystalline interface) because the overall strain reduction within the material is enough to overcome the increase in area upon loop formation.

At high annealing temperatures (>900°C), the type II loops are thermally unstable and dissolve releasing interstitials into the bulk. Claverie et al.[24] have shown that these loops act as reservoirs, maintaining a high supersaturation of free interstitials during their dissolution which leads to an increase in boron diffusivity, probably due to the formation of mobile boron-interstitial pairs. However, dislocation loops can also act as sinks, gettering interstitials at lower temperatures. Listerbarger et al.[25] used the EOR loops as detectors for quantifying interstitial fluxes and this data can complement information gained from measuring dopant diffusion. This gettering process is due to the strain between a free interstitial and one that is bound by the dislocation loop. In this experiment, damage created by an amorphizing Ge^+ implant was annealed at low temperatures to form point defect clusters or at high temperatures to form EOR loops. A subsequent B+ implant was performed followed by an anneal and the flux of interstitials trapped by the loops was measured. It was found that the loops are atleast 20% more efficient than the clusters in trapping interstitials and that it was possible to introduce a controlled layer of loops which can be used as very sensitive point defect detectors.

Experiments using P and B[26,27] implant profiles located within an amorphous layer generated by Si post-amorphization showed no detectable diffusion enhancement of the dopant thus indicating that the EOR dislocation loops act as a barrier preventing the backflow of excess point defects

generated beyond the a/c interface from diffusing into the regrown crystalline region. Also, studies using CVD grown B-marker layers below the loop layer show no enhanced diffusion of the marker due to a subsequent surface implant and anneal.[28] This indicates that the loops are very effective in blocking interstitial injection and the interaction kinetics appear to be diffusion limited.

Jones et al.[29] studied the interaction between {311} defects and type II loops in Si+ implanted silicon. The study showed that the growth of the type II loops is greater than can be explained by the {311} defect dissolution, indicating that there may be an additional source of interstitials besides the {311} defects for amorphizing implants.

1.4.2.2 {311} Rod-like defects

At the present time, it is believed that point defects left over after recombination of vacancies and interstitials will be primarily in the form of interstitial clusters, both visible under transmission electron microscopy and sub-microscopic (SMIC's). High resolution transmission electron microscopy and amplitude contrast studies reveal that point defects coalesce into rod-like defects running along the [110] directions and lying on the {311} planes as a monolayer of hexagonal silicon.[30] This structure represents a low energy means of accommodating excess interstitials in silicon without dangling bonds. {311} defects are known to occur under conditions of oxidation and radiation. Experiments showed rod-like defects in electron,[31,32] neutron,[33]

proton,[34] phosphorus,[35,36] boron[37] and silicon irradiated silicon,[29,38] as well as electron irradiated germanium.[39]

The {311} defects are unstable and will dissolve very fast at annealing temperatures >700°C. Experiments have shown that at 815°C, these defects will dissolve within 5 minutes (Figure 1.4).[38] This dissolution is believed to be a source of interstitials for TED. During annealing, the {311} defects undergo Ostwald ripening leading to an increase in size as well as evaporation, causing emission of interstitials. The interstitials trapped in {311} defects decay exponentially with annealing time with a characteristic time constant that is smaller for higher temperature. The interstitials released can cause diffusion of dopant spikes at a greater depth. A study of this enhanced diffusion can provide insight into the interstitial supersaturation.

1.4.3 Type III: Regrowth Related Defects

Type III defects are associated with imperfect solid phase epitaxial regrowth of any amorphous layer produced during implantation. The major forms of type III defects are "hairpin" dislocations, microtwins and segregation related defects.[40,41]

1.4.4 Type IV: Clamshell Defects

If the implant energy is sufficiently high it is possible to produce a buried amorphous layer. The regrowth of this buried amorphous layer results

in a layer of defects labeled type IV defects which have a zipper or clamshell appearance.[42] These defects, which form at the junction of the two advancing a/c interfaces, have been extensively studied.[43,42,44]

1.4.5 Type V: Precipitation Related Defects

Because ion implantation is a non-equilibrium process, it is possible to exceed the solid solubility of a species in a given target material. Upon solid phase epitaxy, dopant concentrations in excess of the retrograde maximum solid solubility can be substitutionally incorporated. Upon further annealing, precipitation occurs and defects arise from either the precipitation/precipitate dissolution process or upon the release of trapped point defects. The type V defects include precipitates and dislocation loops that are generally centered around the projected range.[45]

1.5 Scope and Approach of This Study

This dissertation is divided into two main sets of experimental results. In the first experiment a combination of delta doped marker layers and type II dislocation loops are used for simultaneous point defect diffusion and defect flux studies. By combining the results of the two studies, estimates of C_I^* as a function of temperature can be made which in turn should yield information on the enthalpy of formation for a Si self-interstitial. Also, insights into the effect of the surface can be realized by the quantitative comparison of the loss

of interstitials from the {311} defects versus capture by the type II dislocation loops.

The second experiment focuses entirely on the effect of surface proximity on end-of range defect formation and dissolution. The damaged region is brought closer to the surface by a series of chemo-mechanical polishes and the annealed samples are then analyzed using transmission electron microscopy (TEM) and secondary ion mass spectroscopy (SIMS).

The contibution of the experimental results to the overall understanding of point and extended defect behavior is discussed along with comparisons to previous studies, and avenues of future study are suggested.

Vacancy Mechanism   Interstitial Mechanism   Interstitialcy Mechanism

$$A + V \Leftrightarrow AV$$ $$A + I \Leftrightarrow A_I$$ $$A + I \Leftrightarrow AI$$

● Dopant atom
● Silicon atom
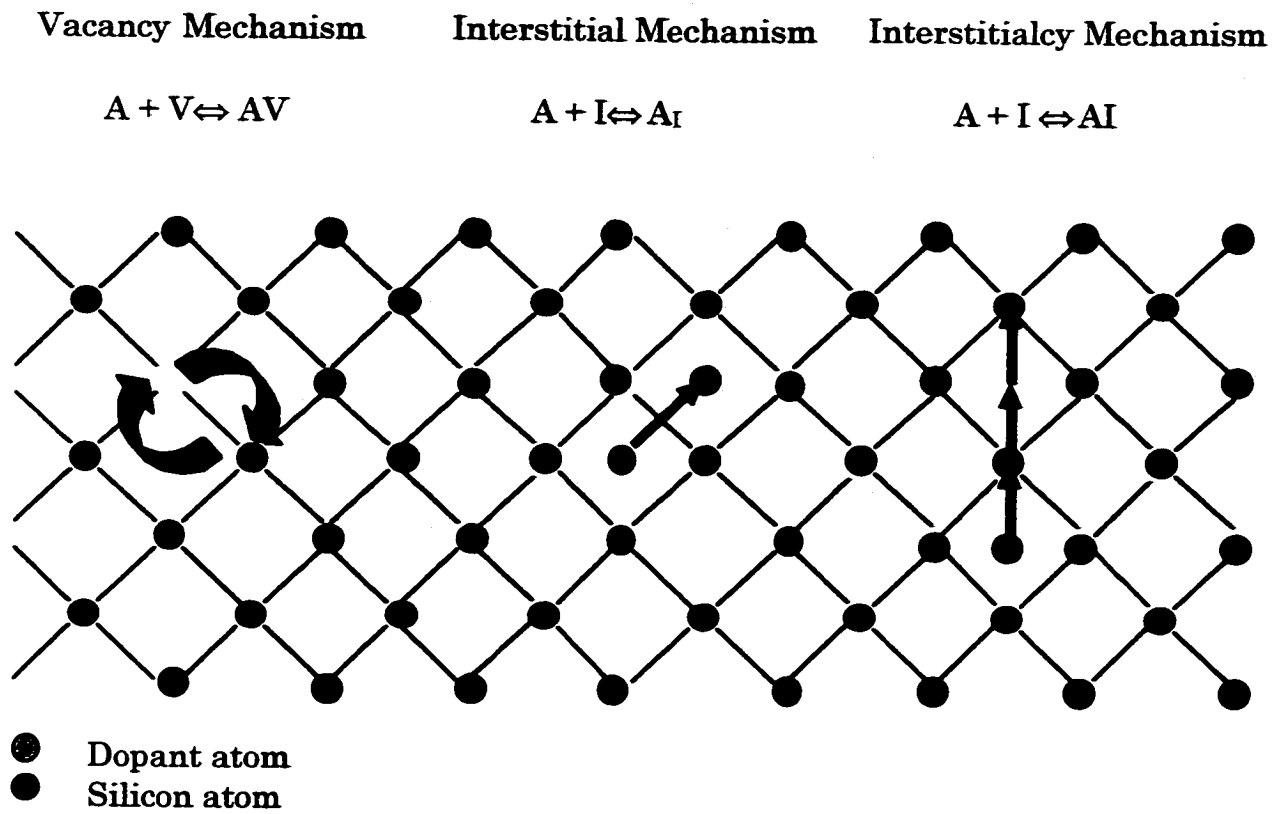
Figure 1.1 Models of atomic diffusion mechanisms for a two-dimensional lattice.

$$D_I \text{ vs. } 1/T$$
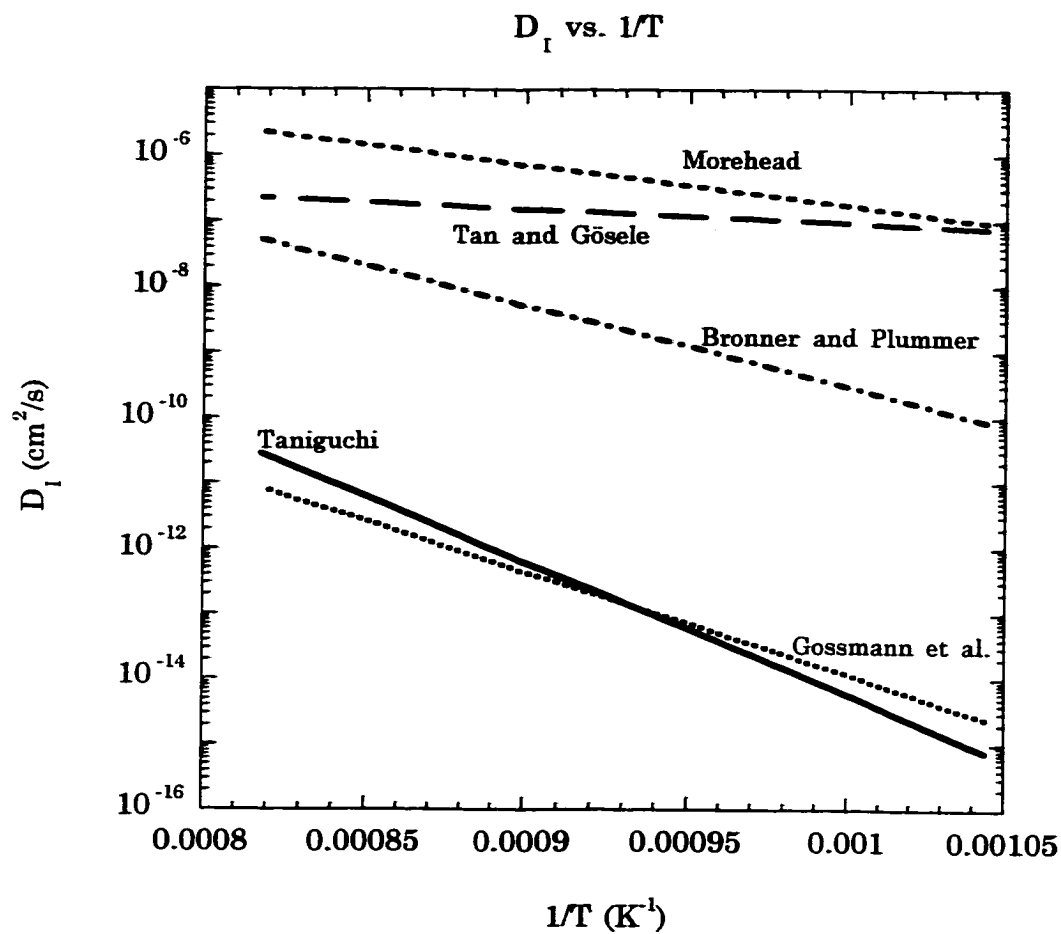
Figure 1.2 Calculated diffusivities D_I for silicon self interstitials as a function of inverse absolute temperature.[86,16,62,81,87]
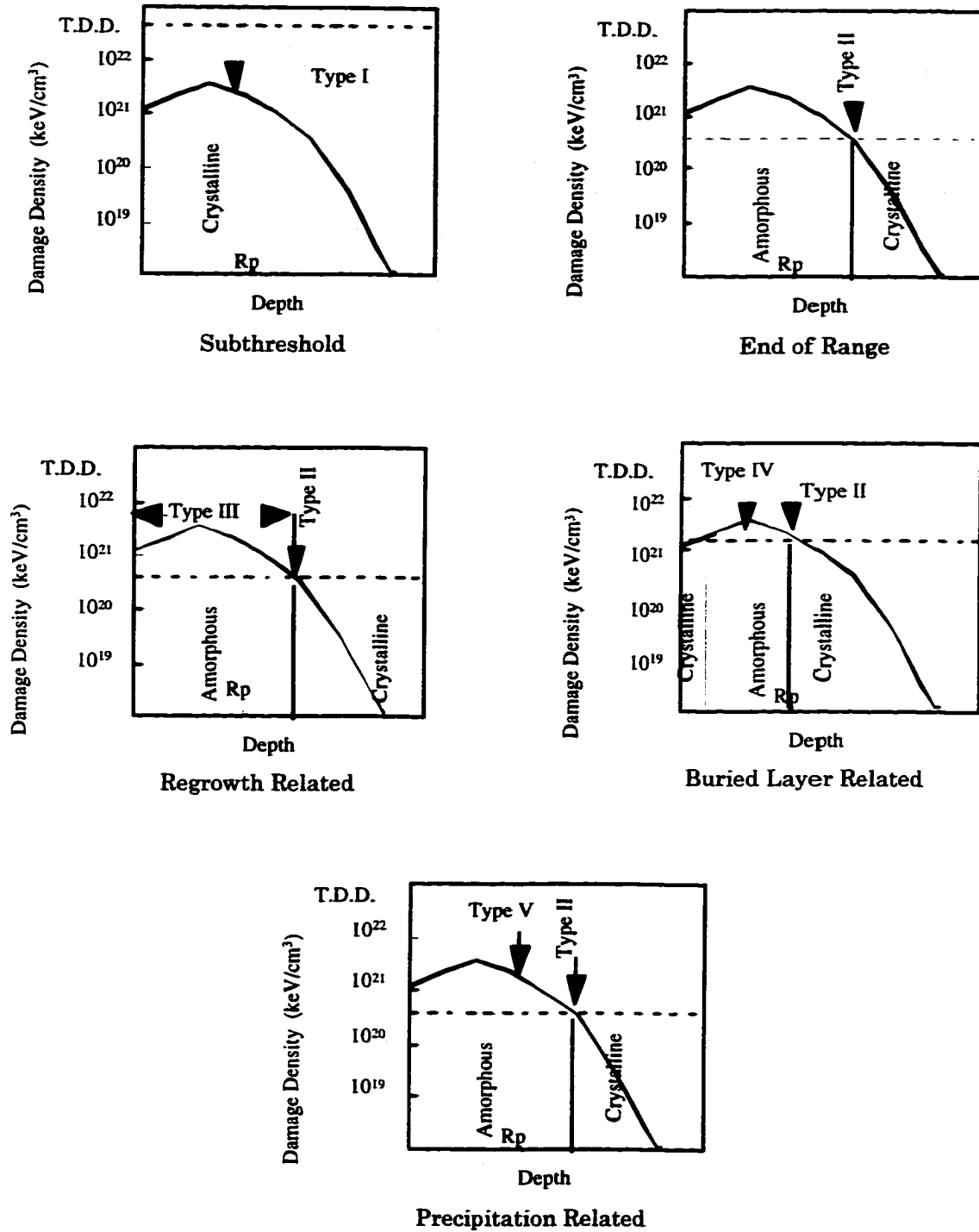
Figure 1.3 Damage classification criteria after ion implantation and annealing.
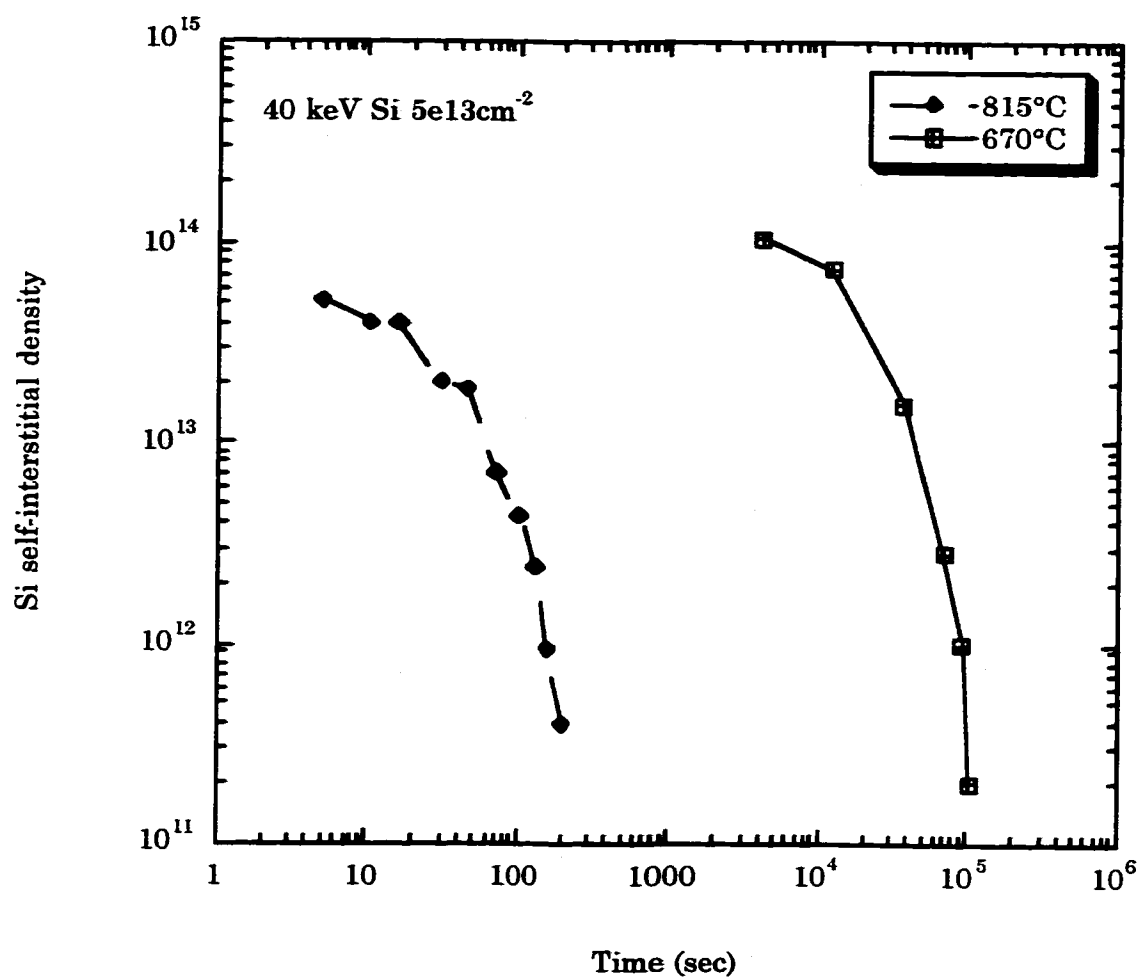
Figure 1.4 Total interstitial areal density in {311} defects as a function of annealing time. Data is for FZ Si samples which were implanted with 40 keV 5e13 cm^{-2} Si and annealed in forming gas.[46]

CHAPTER 2
SAMPLE PREPARATION AND CHARACTERIZATION TECHNIQUES

This chapter will provide an overview of the sample preparation and characterization techniques that have been used in the course of the experiments that have been discussed in the subsequent chapters.

2.1 Doping Superlattices: Growth and Qualification

As stated in the previous chapter, dopant marker layers are an excellent tool for studying the diffusion of point defects in silicon and thus extracting information about their properties. There are several methods available to make dopant marker layers in Si. A single dopant implant with a subsequent anneal to eliminate the disturbance in point defect population will lead to a single marker layer. However, the implant profile will be broad and typically asymmetric due to channeling. Also, the dopant profile will be close to the surface. A CVD technique can be used to epitaxially deposit Si on the surface thus varying the depth of the marker layer but one must still deal with sensitivity limitations imposed by a broad profile.

Another method is to grow dopant marker layers by an epitaxial CVD process. This avoids the point defect disturbance and asymmetric profiles that implantation causes. Marker layers grown by CVD techniques have

22

been used to investigate the properties of point defects in Si. However, CVD can result in contamination from the precursor sources, especially carbon contamination, which is undesirable because of its effects on point defect behavior. Also, due to the inability to shut off the dopant sources quickly, sharp, thin profiles cannot be grown and the resulting profiles are usually box shaped. CVD also requires a relatively high deposition temperature causing diffusion of the grown-in dopant and smearing of the box-shaped profile.

A method that eliminates all of these problems is low temperature molecular beam epitaxy (LT-MBE). By utilizing a low growth temperature (<500°C) extremely thin ∂-doping profiles can be achieved and diffusion of the dopant is minimized. Use of elemental sources limits impurities while the low flux rates lead to excellent control over dopant concentration in the spikes.

The material that will be used in the study involving the determination of the equilibrium concentration of Si interstitials was grown by Dr. Per Kringhøj of the University of Aarhaus, Denmark. A Si buffer layer of 300 nm was first grown on a (100) Si substrate followed by a B-spike 10 nm wide and having a peak concentration of ~ 1e18 cm^{-3}. Two subsequent B-spikes, also 10 nm wide with peak concentrations of 1e18 cm^{-3}, were grown 230 nm apart. This was followed by ~230 nm of undoped Si. The growth was carried out in a VG80 system at a growth temperature of 550°C. Previous studies[47] have shown that the unwanted contaminants from the sample heating elements,

filaments etc., as deduced by deep level transient spectroscopy (DLTS), was below 1e14/cm³.

In addition, CVD grown samples with a single B spike were obtained from Intel Corp. for use in the experiment on the effect of the surface on defect morphology. These samples were grown at 850°C on a (100) Si substrate in a commercial single wafer epi system. B_2H_6 was used as the boron souce and $SiCl_2H_2$ was the silicon source. The B spike is approximately 50nm wide and has a peak concentration of ~ 2e18 cm³.

It is necessary to qualify the as-deposited sample by determining whether it has an equilibrium concentration of vacancies and interstitials. This was done by annealing two sample pieces at 750°C for short (30 to 60 minutes) and long (4 to 6 hrs) times in a nitrogen ambient and then checking the dopant profiles with SIMS. The as-deposited and annealed profiles (Figure 2.1) were analyzed using FLOOPS and the B diffusivities were extracted. It was determined that the as grown B diffusivity enhancements for all the B spikes were less than 10X for the short time anneal and decreased with time to ~ 3X (compared to an accepted value for the B diffusivity) thus indicating a "good" wafer.

2.2 Transmission Electron Microscopy

It is possible to detect the physical damage resulting from ion implantation by a number of methods of which Rutherford backscattering

(RBS) and transmission electron microscopy (TEM) have been used most extensively. Although RBS yields depth information as well as lattice location (interstitial/substitutional) information, correlation of plan-view and cross-sectional TEM samples yields three dimensional information which is mandatory if a thorough understanding of the various forms of damage is to be attained. In addition, structural characterization of the different forms of extended damage (e.g. dislocations, {311} defects etc.) is only possible by TEM. This information is obtained from sample regions that have been thinned so that they transmit electrons. The defect structure can be analyzed by both cross-sectional and plan-view TEM. Cross-sectional TEM (XTEM) can be used mainly to determine depth of defect layers (amorphous layers, dislocation loops and {311} defects) while plan-view TEM (PTEM) is mainly used to study defect evolution during annealing and extract quantitative information on point defects (interstitials) contained in the defects.

2.2.1 Plan-view TEM Sample Preparation

The standard method for preparing a plan-view Si TEM sample involves cutting a 3 mm diameter disc from a wafer, usually with an ultrasonic disc cutter using a SiC cutting slurry. The disc is lapped to ~100µm thickness using 15µm and 5µm Al_2O_3 powder on a glass plate. The implanted side is then protected by coating it with wax and the disc is then mounted on a Teflon pedestal so that the backside (unimplanted side) of the

disc is exposed. This is then smothered with wax and then a small hole is scribed in the center so that the Si is exposed here. The disc is then drip-etched or jet-etched with an acid solution (25% HF: 75% HNO3) till a small hole appears in the sample. The wax is then washed off in Heptane.

2.2.2 Cross-section TEM Sample Preparation

Sample pieces about 1 cm x 1 cm were mounted on a dummy Si wafer using crystal bond and pressed down so as to be flat. The sample was cut into 12 mil strips using a dicing (Tempress 602). The top surfaces (i.e. the implanted side) of two such strips were coated with M-bond 600 adhesive and brought in close contact with each other. Dummy strips were added to each outside surface in order to increase the width and stability of each sample. The samples were then heated for 60 min at 110°C in an oven to cure and harden the adhesive. The bonded strips were affixed onto a polishing jig (South Bay Technology) and thinned from both sides to a thickness of about 50 μm. Slotted copper rings 3 mm in diameter were then mounted onto the thinned samples to provide mechanical strength. Finally, the sample was milled in a dual gun Gatan ion mill set at a 15 angle of incidence using Ar+ ions, a 5 kV gun voltage and a 0.5 mA gun current until a small hole was opened. The regions around the hole were sufficiently thin to be electron transparent and could be analyzed in the TEM.

2.2.3 Imaging of Extended Defects: Loops

For most implants at doses above 2e14 cm^{-2} subthreshold (type I) or end-of-range (type II) dislocation loops will form. Diffraction contrast theory predicts that a defect is visible if $\mathbf{g} \cdot \mathbf{b} \times \mathbf{u} \neq 0$ where $\mathbf{g}$ is the reciprocal lattice vector corresponding to the diffracting plane, $\mathbf{b}$ is the strain vector (or Burgers vector for a dislocation) of the defect and $\mathbf{u}$ is the line direction (for a dislocation). For both the plan-view and cross-sectional samples a 2-beam condition is typically used with s>0, where "s" is the deviation from the exact Bragg condition. Since the Burgers vectors for most of the dislocations are of either a/2<110> or a/3<111> type, the g_{040} reflection can be used for plan-view samples in order to image both sets of dislocations with Burgers vectors parallel to the {001} surface. This is important in characterization of the Burgers vectors and habit planes of network dislocations as well as half-loop dislocations. For example, dislocation loop networks form at the projected range region for 30 keV B^{+} implants with doses above 2e15 cm^{-2} followed by a 900°C, 30 min. anneal whereas half loops are common to As^{+} implants above 5e15 cm^{-2}. The g_{220} reflection is used for both PTEM and XTEM samples because the defect contrast intensity is greatest for this reflection. In most cases, the weak beam dark field (WBDF) conditions are used to increase the resolution of the dislocations. This technique involves using a large deviation parameter $|s| \geq 0.02\text{Å}^{-2}$ and results in increased resolution since only the

region of highest strain, i.e. that closest to the dislocation core, diffracts the beam sufficiently to yield contrast in the image.

2.2.4 Imaging of Extended Defects: {311}'s

One of the most important defects in implanted Si is the {311} defect since it has been shown to be a source of interstitials for transient enhanced diffusion (TED. Since these defects can form at doses as low as $5e12/cm^2$ the imaging and quantification of the defects is critical to understanding post implantation dopant diffusion[48]. {311} defects are elongated in the [110] directions and consist of interstitials precipitating on {311} habit planes. The Burgers vector is thought to be about a/24 [116]. When imaging defects such as {311}'s and dislocation loops in silicon, most researchers use the g_{220} reflection, of the [001] zone axis, in weak-beam, dark field (WBDF) TEM. However some families of those defects will be invisible since {311} defects are out of contrast for **g** parallel to their length, and others very faint, if the g_{220} is the only reflection used for imaging[49]. Thus, in order to maximize the number of defects visible for counting purposes, PTEM images at several different **g** values (220, 400 etc.) for several diffraction conditions (g.2g, g.3g, etc.) need to be taken. This method can then account for all the defects present.

2.3 Determination of Trapped Interstitial Population

It is possible to detect the physical damage resulting from ion implantation by a number of methods of which Rutherford backscattering (RBS) and transmission electron microscopy (TEM) have been used most extensively. Although RBS yields depth information as well as lattice location (interstitial/substitutional) information, correlation of plan-view and cross-sectional TEM samples yields three dimensional information which is mandatory if a thorough understanding of the various forms of damage is to be attained. In addition, structural characterization of the different forms of extended damage (e.g. dislocations, {311} defects etc.) is only possible by TEM. This information is obtained from sample regions that have been thinned so that they transmit electrons. The defect structure can be analyzed by both cross-sectional and plan-view TEM. Cross-sectional TEM (XTEM) can be used mainly to determine depth of defect layers (dislocation loops and {311} defects) while plan-view TEM (PTEM) is mainly used to study defect evolution during annealing and extract quantitative information on point defects (interstitials) contained in the defects.

2.3.1 Trapped Interstitial Concentration: Loops

Typically the implant damage for sub-500 keV implants is confined to a depth less than a half a micron. A transmission electron microscope operating at 200 keV can image through this depth , thus all of the

dislocation loops can be imaged in plan view. Thus by determining the defect size and density it is possible to quantify the trapped interstitial content in the defects. Several methods have been used to quantify total number of trapped interstitials in the dislocation loops. The most commonly used methods are tracing,[28] tracing combined with image processing, and the use of Gaussian distributions to estimate size.[50]

Stereology is based on geometric probability, which has been in use for several decades. According to stereology, the probability that any given point is within a dislocation loop is the same as the area fraction covered by the loops. Therefore, a grid is used, and the fraction of grid nodes within the loops is the same as the fractional area covered by the loops. Since the loops are all extrinsic the trapped interstitial content in the loops can now be determined.

Several grid/image magnification combinations were studied and the procedure outlined below minimized the time/error combination. Weak beam, dark field transmission electron microscopy is used to produce a negative at a magnification of 50,000 X. An 8x10 inch print is made at a magnification of approximately 4X, resulting in a total magnification of approximately 200,000X. A 0.5cm spaced grid (1333 nodes) is placed over the photograph. Then every node that lies inside a loop is marked. The number of marked points is divided by the total number of points (1333 in this case). This fraction is multiplied by the planar atomic density of the {111} plane ($\sim 1.6E15/cm^2$) to yield the number of trapped interstitials.

Following many tests the error for a single investigator counting the same image was found to be less than $\pm$ 3E12/cm^2. In addition if two people count the same image the error again is less than $\pm$ 4E12/cm^2. Thus stereology offers an improvement in accuracy over the previous methods, especially in reducing the error from person to person.

2.3.2 Trapped Interstitial Concentration: {311} Defects

When imaging defects such as {311}'s and dislocation loops in silicon, most researchers use the g_{220} reflection, of the [001] zone axis, in weak-beam, dark field (WBDF) TEM. However, some families of these defects will be invisible since {311} defects are out of contrast for **g** parallel to their length, and others very faint, if the g_{220} is the only reflection used for imaging. This could lead to lower defect counts and thus inaccurate calculations of trapped interstitial concentrations. In order to maximize the number of defects visible for counting purposes, TEM images at several different **g** values (220, 400, etc.) for several diffraction conditions (g.2g, g.3g, etc.) need to be taken. The images are then traced on transparencies and overlapped to account for all defects present. This method of defect counting, while comprehensive, is extremely time-consuming and yields diminishing returns, particularly for a large experimental matrix. This method of determining the trapped interstitial density in {311} defects has been described elsewhere in more detail.[49]

2.4 Ellipsometry

As has been stated in section 1.4, the end-of-range defects form just below the amorphous/crystalline interface upon annealing. Thus determination of the amorphous layer thickness gives the location of the EOR damage layer. There exist different techniques to determine the amorphous layer thickness, both destructive and non-destructive. The common destructive technique used widely is cross-sectional transmission electron microscopy (XTEM). In addition to being destructive, the disadvantages of an XTEM analysis are that the process, especially sample preparation is costly, tedious and time-consuming. Also, a transmission electron microscope is an expensive piece of equipment. In comparison, spectroscopic ellipsometry (SE) is a non-destructive analytical technique that requires very little sample preparation (usually, a surface cleaning step is all that's required). Also, the actual analysis is simple, largely automated and fast. Previous experiments[51,52] in ellipsometry have shown that SE can provide information on

- the depth profile of multilayer structures

- quantitative information on the thickness and composition of each layer

- the structure (whether amorphous or crystalline) as well as the degree of crystallinity

- microroughness of the surface, if present

Also, this technique can be extended to in situ conditions to monitor film deposition or ion implantation processes.

In ellipsometry, a collimated polarized light beam is directed at the material under study, and the polarization states (ellipsometric ψ and Δ, where $\tan\psi$ is known as the amplitude factor and $\exp(j\Delta)$ is the phase factor) of light reflected of the surface and the interfaces are determined using a second polarizer possibly as functions of the light beam wavelength, angle of incidence and/or polarization state. Also, ψ and Δ are related by the expression

$$\rho = \frac{r_p}{r_s} = (\tan\Psi)e^{j\Delta} \tag{2.1}$$

$$\text{and } r_p = \frac{\eta_1 \cos\theta_i - \eta_0 \cos\theta_r}{\eta_1 \cos\theta_i + \eta_0 \cos\theta_r} \tag{2.2a}$$

$$r_p = \frac{\eta_0 \cos\theta_i - \eta_1 \cos\theta_r}{\eta_0 \cos\theta_i + \eta_1 \cos\theta_r} \tag{2.2b}$$

where r_p and r_s are the complex Fresnel reflection coefficients for the p and s polarizations respectively, where p refers to the light vector component parallel to the plane of incidence and s refers to the component perpendicular to the plane of incidence (Figure 2.3). For any angle of incidence between 0° and 90°, p-polarized light and s-polarized will be reflected differently so that $r_p \neq r_s$.

Once the optical constants are measured, a model is constructed in order to accurately predict the unknown parameters e.g. the amorphous layer thickness. The unknown physical parameters are then varied till the calculated data closely matches the measured optical data. Having found a set of physical parameters, this set is then evaluated in order to determine that it is unique and physically reasonable. A flowchart of the procedure used for an ellipsometric experiment is given in Figure 2.4.

All measurements were made on a J. A. Woollam multi-wavelength spectroscopic ellipsometer at a fixed angle (usually 75°). The ellipsometer uses a rotating analyzer/detector combination to measure beam polarization states. The data measured is the ratio $\rho=r_p/r_s$ for wavelengths varying from 250 to 1100 nm. First, a calibration wafer with a known oxide thickness is analyzed and used to calibrate the system. The surfaces of the calibration wafer and the samples for analysis are cleaned so as to prevent errors arising from surface artifacts. The sample size should be large enough (atleast 1cm x 1cm) so that the beam hits the sample away from the edge thus eliminating edge effects. The spot size of the incident beam is of the order of 3mm in diameter. For the samples analyzed here, only amorphous Si and Si oxide are the expected layers, so these two are entered into the computer along with an initial guess for their respective thicknesses. After the calibration run, the sample to be analyzed is placed on the stage and the data acquisition step is

carried out. The numerical analysis of the data is based on a mathematical model based on the Levenberg-Marquardt algorithm. Successive iterations are carried out by varying the thicknesses of the amorphous silicon and silicon oxide layers till the mean-squared error (MSE) cannot be improved upon i.e. a best fit between the measured ψ_i^{exp} and Δ_i^{exp} and the calculated ψ_i^{mod} and Δ_i^{mod} is found. The MSE is given by the mathematical equation

$$MSE = \frac{1}{2N-M}\sum_{i=1}^{N}\left[\left(\frac{\psi_i^{mod}-\psi_i^{exp}}{\sigma_{\psi,i}^{exp}}\right)^2 + \left(\frac{\Delta_i^{mod}-\Delta_i^{exp}}{\sigma_{\Delta,i}^{exp}}\right)^2\right] = \frac{1}{2N-M}\chi^2 \quad (2.3)$$

where N is the number of (ψ,Δ) pairs, M is the number of variable parameters in the model, and σ are the standard deviations on the experimental data points. Once this is done the layer thickness corresponding to the minimum MSE value is displayed and recorded.

2.5 Chemo-mechanical Polishing

For the studies on surface recombination effects controlled thinning of the amorphous silicon layer is required after ion implantation. So spectroscopic ellipsometry can be used simultaneously with chemo-mechanical polishing to get amorphous layers of required thicknesses without changing the damage beyond the end-of-range. A piece of silicon wafer 1 cm x 1 cm in size is mounted on a South Bay Technology Model 150 lapping jig using crystal bond. The sample is mounted as planar as possible so as to ensure

uniform lapping. Lapping is done on a fine rayon pad using Syton®, a 0.01µm colloidal silica suspension, as the polishing agent. The amounted of silicon removed during the polishing has been calibrated in the past by Herner et al.[53] and also by Raman et al.[54] The thickness of the amorphous layer is regularly checked using the ellipsometry after washing the sample surface and drying it with a compressed nitrogen spray. Since the sample is mounted on the polishing jig during the ellipsometry measurements it is necessary to adjust the stage height prior to taking the measurements. The lapping process is then repeated till the required amorphous layer thickness is achieved.

2.6 SIMS Profiling and Boron Diffusivity Extraction

The most common technique to resolve atomic doping concentration profiles is secondary ion mass spectroscopy (SIMS). A rastering primary beam of oxygen or cesium sputters a crater (typically 200 x 200 µm) of which the secondary ions are analyzed by mass spectrometry. After the SIMS analysis, the crater depth is measured using a Dektak and the average sputtering rate is determined, which is then used to reconstruct the concentration vs. depth profile. The SIMS resolution is <50Å and the relative accuracy in concentration and depth measurement are <10%.

Sputtering SIMS is used to characterize the dopant profiles before and after processing. A typical SIMS run uses a 3.5 keV O_2^+ beam angled at 35°

to the sample surface. The beam rasters over a sample area that is about 200 x 200 μm and the B signal is detected from a central area about 60 μm in diameter. Under these conditions the sputter rate is about 5-10 Å/s. The boron peaks are then split into individual files. Since the boron peaks are sufficiently deep (>2000Å), it is assumed that the dose of boron in the spikes are conserved and therefore can be normalised to the dose of the as deposited spike.

The diffusivity enhancement at each time and temperature combination is then extracted for each boron peak using FLOOPS (Florida Object Oriented Process Simulator)[55]. This is done by diffusing the initial profile at the temperature of the anneal for times that result in a best fit of the final measured profile. The ratio of the time required by the simulator to achieve the best fit to the actual time of the anneal is then equal to the diffusivity enhancement.

2.7 Simulation of Implant Profiles Using UT-MARLOWE 5.0

UT-MARLOWE is a software platform for the simulation of ion implantation into crystalline and amorphous materials. The modeling of ion implantation using UT-MARLOWE results in the prediction of impurity profiles as a function of implant parameters and also the damage profiles that can be used as inputs for transient enhanced diffusion simulations.

During the course of this dissertation UT-MARLOWE has been used mainly to simulate amorphous layer formation for comparison with experimentally determined layer thicknesses and to determine interstitial and net excess interstitial (NEI) profiles beyond the amorphous/crystalline interface. These defect profiles are then related to the trapped interstitial dose in the end-of-range defects. At the conclusion of the simulation UT-MARLOWE generates certain output files that contain information on the damage produced. The *filename.rbs* file contains the normalized damage profile in units of 'percent amorphization' vs. depth from which an amorphous layer thickness can be extracted. The *filename.ist* and *filename.vac* output files provide concentration profiles of the silicon interstitials and vacancies formed during the implantation. The integral of the *filename.ist* and *filename.vac* files below the a/c interface gives the excess interstitial and excess vacancy dose and the difference between these two gives the NEI value. Since the NEI value is a difference of two large numbers, in order to get sufficient accuracy, the simulation needs to be run with a large number of ions in the input, of the order of 10^6.
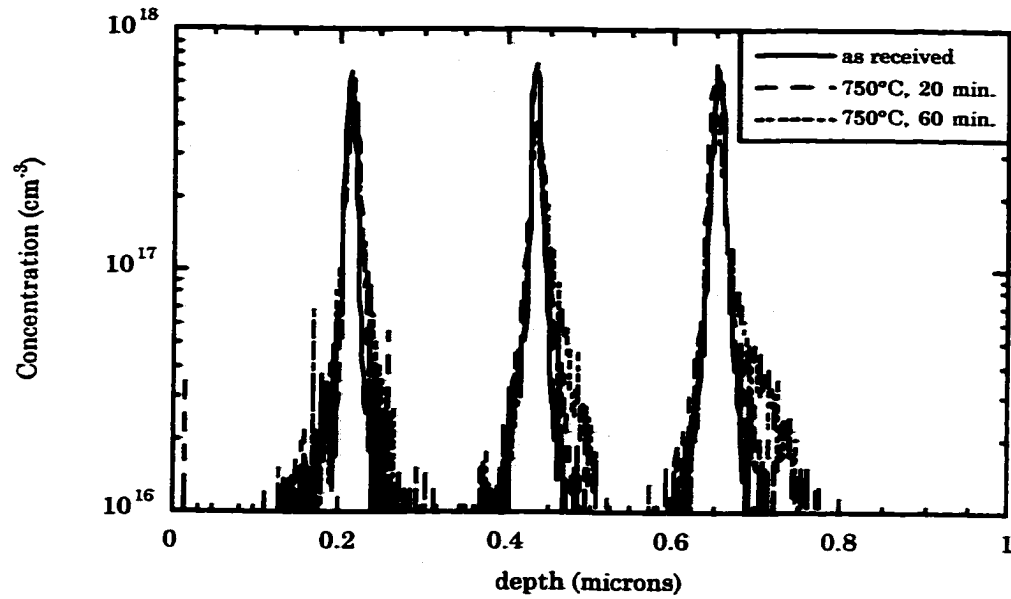
Figure 2.1.a SIMS profiles of MBE-grown B-DSL samples used for qualification.
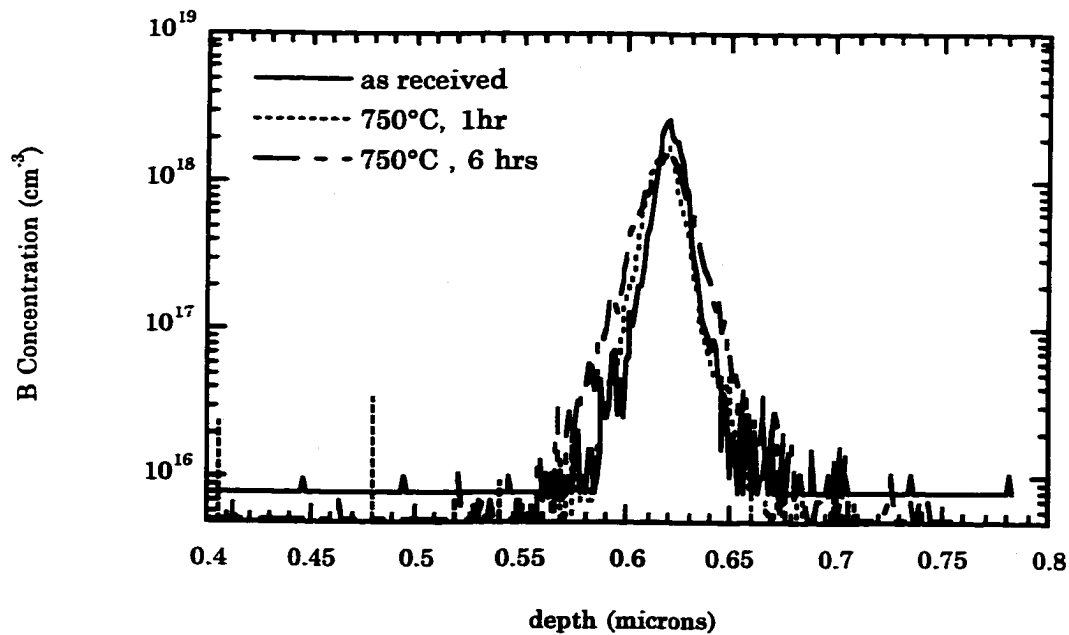
Figure 2.1.b SIMS profiles of CVD-grown B-DSL samples used for qualification.
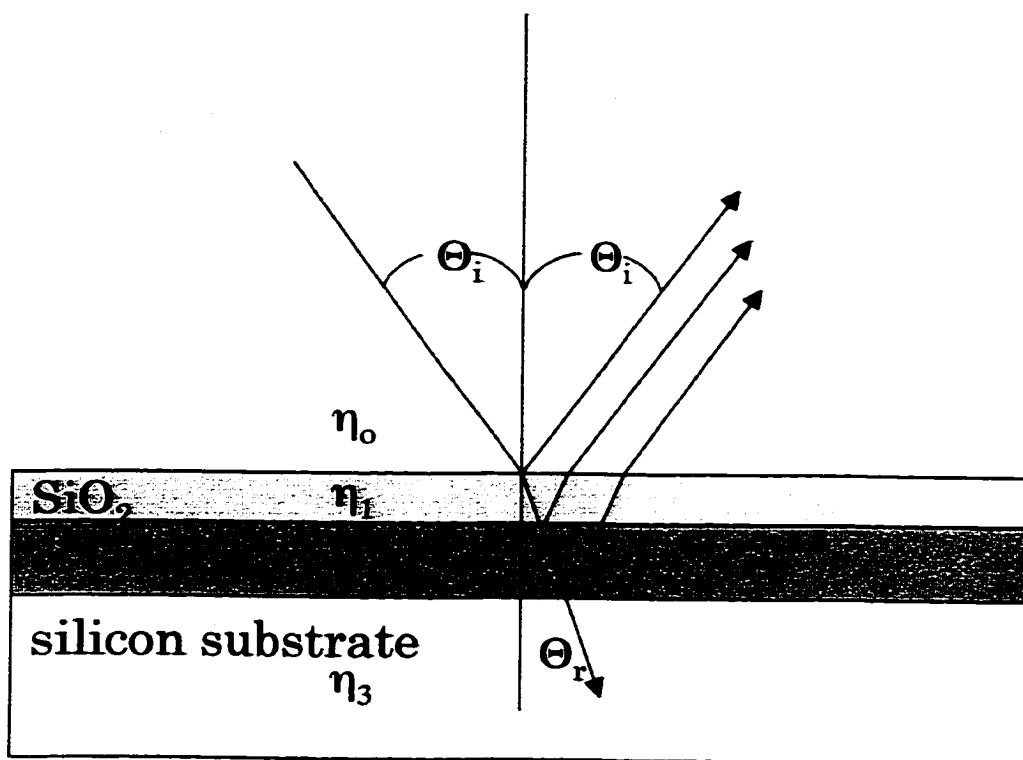
Figure 2.2 Schematic diagram of a planar structure assumed for spectroscopic ellipsometry (SE): η_o is the complex index of refraction for the ambient medium, η_1, η_2, η_3 are the complex indices of refraction for the structure materials as shown, Θ_i is the value of the angle of incidence and angle of reflection and Θ_r is the final angle of refraction.
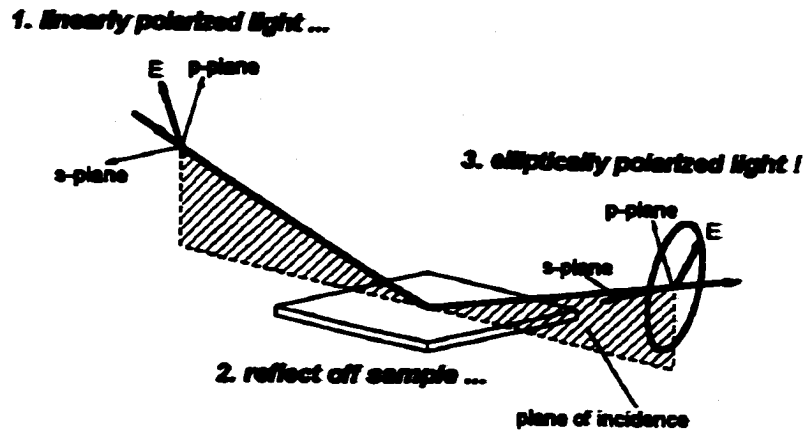
Figure 2.3 Measurement geometry for ellipsometric measurements.[56]
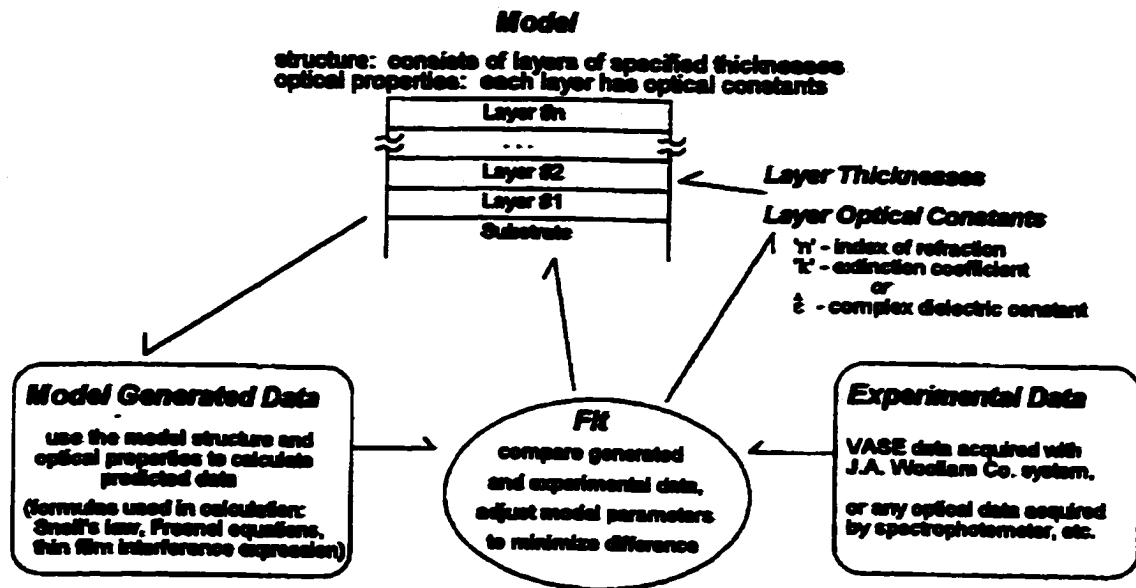
Figure 2.4 Flowchart of the procedure for an ellipsometric experiment.[56]

CHAPTER 3
DETERMINATION OF THE EQUILIBRIUM CONCENTRATION OF SILICON SELF-INTERSTITIALS

Ion implantation is the dominant form of dopant introduction into crystalline silicon. An unavoidable side effect of the implantation process is the crystalline damage created. This damage consists of both point defects (vacancies and interstitials) and extended damage (dislocations and rods). One of the least understood by-products of this damage is Transient Enhanced Diffusion (TED).[57] This occurs because the dopants diffuse through interaction with the point defects. The increase in the point defects from implantation creates a rapid burst of motion that quickly disappears as the implant damage is annealed. The extended defects act as sources and sinks for the point defects, and can modulate the entire TED process.[48,58]

In order to develop accurate physically based process simulators, it is necessary to have a good knowledge of the fundamental point defect behavior.[59] This behavior in silicon is largely unparameterized, because direct methods of measuring the point defects are not possible. Consequently, most of the defect parameters (diffusivities, formation energies, recombination rates, etc.) are obtained by "reverse engineering" diffusion behavior[3] or through *ab initio* calculations[4] and atomistic simulations based

42

on empirical interatomic potentials[6,5]. These calculations provide energies of migration, formation, and binding for various defect structures. However, verification of these parameters is difficult.

This chapter discusses an experimental procedure that provides information on equilibrium concentration on Si interstitials at various temperatures and thus the enthalpy of formation.

3.1 Experimental Approach

The accurate modeling of nonequilibrium diffusion phenomena like TED, OED etc. requires the knowledge of point defect diffusivities and equilibrium concentrations. However, despite numerous attempts, no experimental method has definitely measured the equilibrium concentrations of vacancies and interstitials in silicon, or even the enthalpies of formation. In the presence of interstitials and vacancies the self-diffusion coefficient D^{SD} is given by:

$$D^{SD} = D_I C_I^* + D_V C_V^* \tag{3.1}$$

Knowledge of D^{SD} does not give information on the relative contributions of self-interstitials and vacancies. To date, numerous experiments have tried to determine $D_I C_I^*$ and $D_V C_V^*$. The $D_I C_I^*$ value (also known as the diffusion capacity) is given by

$$D_I C_I^* = 914 \exp(-4.84/k_B T) \ cm^2/s \tag{3.2}$$

where where C_I^* is normalized to 5×10^{22} cm^{-3}. This value is considered reliable since different types of experimental measurements involving in-diffusion of impurities (Au, Pt [15,16]) and tracer diffusion[17] give consistent results. On the other hand, very few experiments have attempted to measure the $D_V C_V^*$ product and the published values are unreliable.[3] So, in order to determine the Si-interstitial parameters it is sufficient to determine either C_I^* or D_I. But this measurement is not trivial as they can only be determined indirectly by interaction of self-interstitials with dopant atoms or extended defects or by self-diffusion experiments using radioactive isotopes like ^{31}Si. However, using the short-lived ^{31}Si radiotracer limits the self-diffusion studies to a rather narrow temperature range near the melting point.[60]

Dopant or impurity diffusion experiments provide a sensitive means of monitoring small deviations and perturbances in point defect concentrations through changes in the impurity diffusion behavior. These kinds of experiments can be divided into roughly two different groups:

- diffusion or gettering experiments using fast metal diffusers

- experiments with dopant marker layers, either implanted or grown-in

The results of these two types of experiments show a wide discrepancy in the derived interstitial diffusivity; D_I is found to be much higher in the metal studies, especially at relatively low annealing temperatures.

In metal diffusion experiments, fast interstitial diffusers such as Au, [61,62], Pt[63, 64] or Zn[65] are diffused into the silicon. By assuming interactions

with the Si self-interstitials such as the kick-out mechanism or the Frank-Turnbull (or dissociative) mechanism, the interstitial diffusivity is calculated by analyzing and fitting the metal diffusion profiles.

Kick-out: $$M_s + I \Leftrightarrow M_I \qquad (3.3)$$

Frank-Turnbull $$M_s \Leftrightarrow M_I + V \qquad (3.4)$$
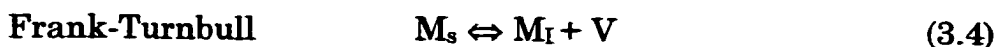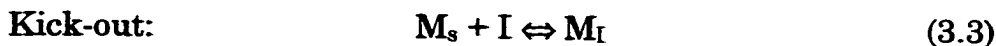
Where M_s and M_I represent the substitutional and interstitial metal and V represents a vacancy. The numerical analysis and the mathematical treatment of foreign-atom diffusion is discussed in great detail by Bracht et al.[65]

In doping layer experiments dopant marker layers are grown in by MBE or CVD or implanted and annealed to remove damage and then their response to Si-interstitial injection (by surface oxidation, ion implantation) is examined. Use of multiple steep narrow profiles obtained by MBE or CVD can detect even a small amount of enhanced diffusion while implanted profies are more spread out and less sensitive. In theory, the silicon self-interstitial diffusivity can be extracted from the depth and time dependence of the diffusion enhancement.[66]

A schematic diagram of a new experimental method is shown in Figure 3.1. One set of samples contain B-doped superlattice marker layers and are grown by low-temperature molecular beam epitaxy (LT-MBE). The second of samples are made by implanting an undoped LT-MBE grown silicon wafer

with Si⁺ or Ge⁺, selecting the implant energy and dose so that an amorphous layer is formed. The wafer is then annealed at 900°C for 30 min to regrow the amorphous layer and form a type II dislocation loop layer. The energy and dose are also selected so that this loop layer forms at the same depth as the first B marker layer from the first sample set. Since both silicon wafers are grown in the same MBE system under similar growth conditions, the defect concentrations (oxygen, carbon and other metallic impurities) and therefore the concentration of traps can be assumed to be similar. The two sample sets then receive identical Si⁺ implants at a lower energy and dose and are then simultaneously annealed to form {311} defects at the projected range. Longer time anneals are then carried out in order to dissolve these defects, thus releasing an interstitial flux. This interstitial flux causes enhanced diffusion of the B marker layers in the first set of samples and is trapped by the dislocation loops in the second set of samples causing loop growth. The set of samples containing the delta-doped B layers are analyzed by SIMS to determine the extent of B diffusion. The enhancement in B diffusion ($<D_B>/D_B^*$) relative to an unimplanted control sample is used to determine the time averaged enhancement in the interstitial concentration ($<C_I>/C_I^*$). The second set of samples, containing the end-of-range <110> dislocation loops, are analyzed by PTEM and NIH Image[67] to determine how the concentration of interstitials bound by the loops varies before and after the ²⁹Si⁺ implantation and annealing treatments. The number of atoms bound by

both the <110> loops and the {311} defects are independently monitored. Under the annealing conditions used in this experiment the EOR loops are in the coarsening regime,[68] therefore, any increase in the number of bound interstitials can be attributed to the capture of interstitials released by the dissolution of the {311} defects. This increase is the interstitial flux, which is related to the C_I value.

By comparing the results of the two parallel experiments, C_I^* can be estimated for different temperatures and times. From this the enthalpy of formation of a Si interstitial can be determined. Since the dissolution of the {311} defects and the number of atoms trapped by the dislocation loops can be computed and compared, these studies can also give quantitative information about the surface recombination and diffusion of defects in the crystal.

3.2.1 Numerical Extraction of C_I^*

Consider a schematic representation (Figure 3.2) of the experimental setup discussed in the previous section with the concentration of the interstitials at a given point in time. The first important point to note here is that the loop layer in the pre–amorphized sample and the shallowest boron spike in the DSL sample are at the same depth, x_0. Above that height, the two samples are exactly identical and the {311}'s are at the same depth below the surface. As shown in Figure 3.2, the flux of interstitials from the {311}'s into the bulk is the same in both samples. This will be further examined at a later point. For the analysis of this experiment three assumptions are made:

1. After a long time (specifically, for the measurement times in our experiment), the total dose of interstitials injected across the plane of depth $= x_0$ is the same in both samples;

2. In the pre–amorphized sample, most of these interstitials are captured by the loops; and

3. In the DSL sample, all of these interstitials remain free and can contribute to the boron diffusivity as long as they remain in the neighborhood of the boron spikes.

In particular, no knowledge of the interstitial diffusivity, the instantaneous flux of interstitials into the bulk as a function of time or the profile of interstitials above depth $= x_0$ is assumed. Also it is not necessarily assumed that at each point in time the flux of interstitials into the bulk is the same in both samples. An examination of the plausibility of our three assumptions given above will be presented later. The strength of the following analysis is that it only utilizes dose information, which can be directly measured, and does not assume knowledge of the details of the flux at a given instant in time.

Consider first the DSL sample. After time t, the total dose that has crossed the x_0–plane has to all be distributed in the remainder of the bulk somehow. Hence:

$$\Delta Q(t) = \int_{x_0}^{x'} C_I(x,t)dx \tag{3.5}$$

Note again at this point that this expression is true regardless of the details of the time behavior of the interstitial flux. In fact, equation 3.5 is true

regardless of the accuracy of any of the above assumptions. In the DSL sample, all of the interstitials that crossed the x_0–plane from time 0 to time t must be distributed somehow in the depth of the sample between x_0 and x' where x' is the depth at which $C_I = C_I^*$. By definition, the interstitial supersaturation, "s" is a time–averaged value for the free interstitial supersaturation:

$$s(x) = \frac{1}{t}\int_0^t \frac{C_I(x,\tau)}{C_I^*}d\tau \qquad (3.6)$$

Note that in equation 3.6 C_I represents the concentration of free interstitials. If we assume that all the interstitials injected across the x_0–plane remain free (assumption 3 noted above), then C_I is the same in both equations 3.5 and 3.6.

For the same time period, the interstitial dose, ΔQ, captured by the dislocation loops in the pre–amorphized samples can be counted. According to assumptions 1 and 2, we can equate this to the total dose of excess interstitials present in the corresponding DSL samples at the end of that time period from the location of the first boron peak downwards. Hence;

$$\int_{x_0}^{x'} s(x)dx = \int_{x_0}^{x'} \frac{1}{t}\int_0^t \frac{C_I(x,\tau)}{C_I^*}d\tau dx = \frac{1}{tC_I^*}\int_0^t d\tau \int_{x_0}^{x'} C_I(x,\tau)dx$$

$$= \frac{1}{tC_I^*}\int_0^t \Delta Q(\tau)d\tau \qquad (3.7)$$

so that;

$$C_I^* = \frac{\int_0^t \Delta Q(\tau)\,d\tau}{t \int_{x_0}^{x'} s(x)\,dx} \qquad (3.8)$$

3.2 Experimental Conditions

Before carrying out the experiment in the LT-MBE grown material, which is difficult to come by, a series of experiments were carried out in readily available CZ grown silicon wafers. One aim of these preliminary studies were to optimize the type II dislocation loop layer distribution and determine the implant conditions need to form the loop layer at the same depth as the first B marker layer, ~2400Å. Also, in order to reduce the inherent statistical error involved in using loops as point defect detectors, it is essential that the loops be well formed, distinct and well distributed.

In order to cause maximum loop growth after the Si^+ implant and anneal, but not so much that the loops start networking, it is necessary to maximize the flux of Si self-interstitials released by the implant. Thus another experiment was carried out to maximize the number of interstitials contained in the <311> defects after a low temperature short time anneal, without forming type I loops.

3.2.1 Optimization of Type II Dislocation Loop Distribution and Depth

Previous studies by Jones et al.[69] and Laanab et al.[70] have discussed the variation in the end of range defect densities and the depth of the a/c interface with the different ion implantation parameters. They showed that the number of interstitials bound by the EOR dislocation loops is a strong function of the implant energy, dose and the implant temperature (i.e. the substrate temperature during the implant). In order to get an estimate of the implant energy and dose required to from the EOR layer at the required depth, simulations were carried out using UT-MARLOWE, which generates damage profiles along with the dopant profile. Using UT-MARLOWE to simulate a 165 keV, 1e15/cm^2 As$^+$ implant resulted in an amorphous layer depth of ~2050Å (Figure 3.3). Since the atomic mass of As (74.9) is very close to that of Ge (72.6), an As$^+$ implant with an energy of 165 keV will result in a damage profile similar to a Ge$^+$ implant with an energy of 170 keV. So, the Marlowe simulation is believed to be sufficiently accurate and the value of 2050Å was used as the initial guess. Since the EOR loops form below the a/c interface, they would form at a depth of ~2200 to 2400Å.

Once the implant energy was fixed at 170 keV, the effect of the other parameters, i.e. dose, and implant temperature were studied. CZ grown n-type phosphorus doped (100) silicon wafers were implanted under the following conditions. Inorder to prevent the formation of a buried amorphous

layer a 75 keV, 1e15/cm² Ge⁺ implant was done prior to the 170 keV Ge⁺

implant. The beam currents were kept constant.

Table 3.1 Implant conditions for studying the effect of implant temperature
and dose on the EOR loop layer depth and distribution.

Wafer ID	Implant Temp (°C)	Dose (/cm²)
1	40	1e15
2	40	2e15
3	5	1e15
4	5	2e15

The wafers were annealed at 900°C for 30 minutes and then analyzed

by PTEM and XTEM. As can be seen from the TEM micrographs in Figure 3.4

and Figure 3.5, the ideal loop distribution and depth (2300Å) occurs for the

sample implanted at 40°C to a dose of 1e15 cm⁻². If the implant temperature

is reduced to 5°C, the number of loops present and therefore the number of

interstitials trapped by the loops decreases and the loops occur at a depth of

2000Å. If the implant dose is changed the width of the loop layer formed upon

annealing increases from ~400Å for the 1e15 cm⁻² implant to ~1000Å for the

2e15 cm⁻² implant.

The EOR dislocation loops are known to be sinks for

interstitials[71,72,73,25]. However studies by Jones et al.[74] show that

amorphizing implants performed at very low temperatures will lead to dislocation loops that are not very effective sinks and do not hamper the flow of interstitials across the a/c interface. This was explained by a TEM study which showed that the loop density distribution increased as the implant temperature increased. Since the sample implanted at 40°C has a higher loop density, it would be a more effective barrier against interstitial flow and lead to a more efficient interstitial sink. Also, the full width at half maximum concentration (FWHM) of the boron spikes in the DSL material are ~100Å we want a loop layer width that is as close to that as possible, hence 1e15 cm^{-2} is the ideal dose for the amorphizing implant.

3.2.2 Optimization of Si$^+$ Implant (Interstitial Flux)

As has been stated in an earlier section on the experimental approach, a Si$^+$ implant into the samples with the EOR loops and the samples with B-DSL's is carried out and then annealed in order to create an interstitial flux into the bulk. In the samples with the EOR loops this interstitial flux is captured by the dislocation loops causing them to grow. In order to reduce the error in the quantification of this growth the flux of interstitials to the loop layer needs to be maximized resulting in a statistically significant increase in the trapped interstitial counts. Therefore maximum interstitial flux can be achieved by maximizing the number of interstitials contained in the <311> defects, without forming type I loops, since the type loops are extremely stable at the temperatures and times studied during this work.[75]

In order to determine the maximum Si implant dose that can be used, implants were done in CZ grown Si wafers at 40 keV with doses varying from 5e13 to 2e14 cm^{-2}. The wafers were annealed at 750°C for 30 min. in flowing N$_2$ and then analyzed by PTEM. It can be seen from Figure 3.6 that an increase in dose from 1e14 cm^{-2} to 2e14 cm^{-2} leads to the formation of type I loops. Thus, this experiment shows that 1e14 cm^{-2} is the maximum allowable dose for the 40 keV Si$^+$ implant.

3.3 Experimental Results

Once the optimal experimental conditions were determined using the CZ grown wafers, the MBE grown boron-doped superlattice samples and the EOR loop layer samples (also MBE grown Si) were implanted with Si$^+$ ions at an energy of 40keV to a dose of 1e14 cm^{-2}. Pieces from each sample are annealed simultaneously in a furnace or RTA under a flowing N$_2$ ambient for different times at 685°C, 750°C and 815°C. The B-DSL samples are then analyzed by secondary ion mass spectroscopy (SIMS) to profile the boron spikes and thus determine the diffusivity enhancement (and thus the interstitial supersaturation). The implanted and annealed EOR loop samples were analyzed by plan view TEM using a g$_{220}$ WBDF condition to image the dislocation loops and the {311} defects.

3.3.1: Determination of the Interstitial Flux Captured by Loops

As can be seen from the PTEM micrographs in Figure 3.7, with an increase in annealing time at a given temperature, there is a decrease in the number of interstitials trapped by the {311} defects and a corresponding coarsening of the dislocation loops indicating an increase in their trapped interstitial content. This increase is quantified using stereology as described in section 2.3. Figure 3.8 shows the variation in the number of interstitials in the loops versus time for the three different annealing temperatures. The number of interstitials at time t=0 is the number of interstitials in the loop sample after the Ge^+ implants and the 900°C, 30 min anneal. This interstitial count remains constant for the control sample during the subsequent lower temperature anneals and is taken as the initial condition. The number of interstitials trapped in this zero reference sample is then subtracted from the number of interstitials trapped in loops at a subsequent time step to give the values of ΔQ, i.e. the increase in interstitials trapped by the loops, used in equation 3.8.

3.3.2: Determination of interstitial supersaturation vs. depth

The B-DSL samples are analyzed by secondary ion mass spectroscopy (SIMS) to profile the boron spikes. This analysis was done on a Cameca IMS-3f system. The concentration vs. depth data from SIMS is then broken up into three files corresponding to the three boron peaks. The total dose contained

within a boron peak is scaled so that it is equal to the boron dose in the as-implanted DSL sample. The three files are then imported into FLOOPS. The simulation to determine the boron diffusivity enhancement then consists of diffusing the profile of the as-deposited spike for a certain time till it matches the implanted and annealed profile. The ratio of the diffusion time in the simulation to the actual anneal time is then equal to the time averaged diffusivity enhancement $<D_B>/D_B^*$. Since for boron

$$\frac{<C_I>}{C_I^*} = \frac{D_B/D_B^*}{f_{IB}} \text{ where } f_{IB} = 0.8[1] \tag{3.9}$$

the interstitial supersaturations can be calculated and are plotted vs. depth (Figure 3.9). The graphs are then fitted with a straight line and the area under the curve from the depth of the first peak to the depth where C_I/C_I^* drops off to a value of 1 is computed. This computed value is equal to the integral

$$\int_{x_0}^{x'} s(x)dx \text{ which appears in equation 3.8.}$$

Some researchers consider the {311} defects to maintain a constant supersaturation in their vicinity during dissolution.[38] If this is the case, then the graph of C_I/C_I^* vs. depth can be considered to be similar to the indiffusion of dopants from a surface source of constant concentration into a silicon wafer and the resulting profile will be of the form

$$C(x,t) = C_s \text{erfc}(\frac{x}{\sqrt{4Dt}})$$ (3.10)

where C(x,t) is the dopant concentration as a function of depth (x) and time (t),

Cs is the constant surface dopant concentration, and D is the dopant

diffusivity. Therefore for the case of constant interstitial supersaturation at

the "surface" (actually at a depth equal to the first spike) we can write

$$\frac{C_I}{C_I^*}(x,t) = (\frac{C_I}{C_I^*})_{x=x_0} \text{erfc}(\frac{x}{\sqrt{4Dt}})$$ (3.11)

where x_0 is the depth of the first B-spike.

Table 3.2 compares the values of the integral $\int_{x_0}^{x'} s(x)dx$ assuming a straight

line fit or an erfc fit to C_I/C_I^* vs. depth.

Table 3.2 Comparison of the values of the integral $\int_{x_0}^{x'} s(x)dx$ assuming a

straight line fit or an erfc fit to C_I/C_I^* vs. depth.

	Straight line fit	erfc fit	% difference
685°C, 4hr	0.63	0.632	0.3
685°C, 10hr	0.30	0.347	13
750°C, 20min	0.27	0.46	24
750°C, 60min	0.0933	0.117	20.3
815°C, 30sec	0.0373	0.044	15
815°C, 60sec	0.027	0.0332	18

Now that the values that need to be inserted in equation 3.8 have been determined, we can solve for C_I^* to obtain the following result at the various temperatures

T (°C)	C_I^* (cm^{-3})
685	5.6×10^{12}
750	1.0×10^{14}
815	2.8×10^{14}

This yields a best fit of:

$$C_I^* = 2 \times 10^{27} e^{-2.7eV/kT} \text{ cm}^{-3} \tag{3.12}$$

3.3.3 Comparison of Diffusivities

As stated earlier, in the presence of interstitials and vacancies the self-diffusion coefficient D^{SD} is given by

$$D^{SD} = D_I C_I^* + D_V C_V^* \tag{3.13}$$

Knowledge of D^{SD} does not give information on the relative contributions of self-interstitials and vacancies. To date, numerous experiments have tried to determine $D_I C_I^*$ and $D_V C_V^*$. The $D_I C_I^*$ value is given by

$$D_I C_I^* = 914 \exp(-4.84/kT) \text{ cm}^2/\text{s} \tag{3.14}$$

where C_I^* is normalized to 5×10^{22} cm^{-3}.

This value is considered to be a reliable and accurate quantity since different types of experimental measurements involving in-diffusion of impurities (Au, Pt [15,16]) and tracer diffusion[17] give consistent results.

In order to compare the value of C_I^* in equation 3.12 to the published values of D_I in the literature, the $D_I C_I^*$ value in equation 3.14 is used. Figure 3.10 shows this comparison.

3.4 Analysis and Discussion

In Figure 3.10, the temperature dependence of D_I given by Morehead[76] is based on re-analysis of Au in-diffusion in Si with the assumption that at temperatures above 800°C the kick-out mechanism, given by

$$Au_i \longrightarrow Au_s + I_{Si}$$

dominates[77,78]. Based on a crude estimate of $C_I^*(T_m)$ where T_m is the melting point of silicon, Tan & Gösele[16] determined D_I vs. T. The experimental procedure was heavily dependent on interstitial- and vacancy-type swirl defects which are notoriously difficult to intepret. Therefore the data should be viewed with skepticism.

The parameter values of Bracht et al.[65,79] are extracted by analyzing Zn diffusion in Si, applying a special method to perform isothermal anneals as short as a few seconds. The diffusion profiles are described by simultaneous diffusion via the kickout and dissociative mechanism. The extraction ignores interaction between the interstital and vacancy mechanisms. This results in a vacancy diffusivity much lower than that of self interstitials which is contrary to molecular dynamics based defect calculations which predict tha vacancies diffuse faster than interstitials. The Zn concentration profiles have

also been re-analyzed by Chakravarthi et al.[80] and conclude that the experiments are insensitive to C_V* and reasonably sensitive to C_I* variations. The results from Bronner and Plummer are extracted from enhanced diffusion of phosphorus and extrinsic gettering of gold. The data is based on the assumption that the mechanism of gettering is only limited by the self-diffusion of self-interstitials. Taniguchi et al.[81] used the growth of stacking faults during oxidation as a monitor of silicon interstital kinetics. The data was analyzed assuming diffusion limited growth of stacking faults. This assumption is not valid because several authors have showed that the stacking fault growth is reaction rate limited.[82,83]

Gossmann et al. investigated the broadening of MBE grown boron spikes during dry oxidation and extracted D_I values which are about 5 orders of magnitude lower than the extractions by Morehead and Bracht et al. which involve fast metal diffusers. Assuming that the concentration of interstitials at the surface was constant during oxidation, the interstitial concentration at a particular time t is proportional to a complementary error function. The low D_I value extracted by Gossmann et al. was explained by trapping of self-interstitials at impurities, especially substitutional carbon[58,84]. Oostrum et al.,[85] in a study of indiffusion of silicon interstitials during oxidation as a function of growth process, found a decay in interstitial concentration in MBE grown films but practically no decay in low temperature CVD grown films.

They attributed this difference to a higher number of traps in the MBE grown films.

The value for C_I^* in equation 3.12 is about 5 orders of magnitude higher than the theoretical calculations of Morehead and Bracht et al. When this value is inserted in the equation for the self–diffusion coefficient, $D_I C_I^*$ (equation. 3.14), it yields a diffusivity that is five orders of magnitude lower than these calculations and is close to the value reported by Gossmann et al. which is thought to be the effective diffusivity in the presence of a large concentration of interstitial traps.

We now examine the validity of our initial assumptions presented in section 3.2.1 in conjuction with this discrepancy in the D_I values in order to obtain a self-consistent picture. It may be argued that the assumed representation of the interstitial scaled concentration profile in Figure 3.2 is wrong and that the correct profile for the interstitials in the samples with dislocation loops is as shown in Figure 3.11. This would occur if the loops were assumed to pin the enhancement in the interstitial concentration to a value of the order of unity. Under such circumstances, the flux into the bulk would be different in the two samples and assumption 1, which states that the total dose of interstitials injected across the plane of depth $= x_0$ is the same in both samples, cannot hold for all time. If this situation were true, one would expect the {311}'s in the loop samples to dissolve more rapidly than those in the boron-DSL samples.

To test this possibility, the dissolution rate of the {311} defects in the two set of samples was determined (Figure 3.12). It was found that there was no measureable difference. This leads to the conclusion that the flux of interstitials away from the {311} defects is the same in both sets of samples and therefore the loops do not affect the flow of interstitials into the bulk.

Another possibility is that the surface controls the dissolution of the {311} defects and hence strong differences in the interstitial concentration at the loop layer and the first boron spike (which is at the same depth as the loop layer) do not affect the dissolution of the {311} defects but the flux of interstitials into the bulk can still be dramatically different in the two sets of samples. The {311} dissolution curves from Figure 3.12 along with the graph of increase in trapped interstitials vs. time from Figure 3.8 can be used to test for this possibility. For example, at 750°C, from 20 minutes to 60 minutes, the interstitial dose in the {311} defects decreases by $1.6e13$ cm^{-2} while the interstitial dose in the loops increases by $1.35e13$ cm^{-2}. This indicates that most of the interstitials emitted by the {311}'s are going into the bulk and not toward the surface. This also validates assumption 2 which states that in the pre–amorphized sample, most of the interstitials emitted by dissolution of the {311} defects are captured by the loops. Since 84% of the interstitials released from the {311}'s are showing up in the loops it implies that the loops are efficient as interstitial sinks. This may seem contradictory: how can the loops be efficient sinks yet not pin the interstitial concentration at some low

value sufficiently different from that in the DSL samples to affect dissolution of {311}'s and hence the interstitial flux? There are two possible answers to this apparent contradiction. One would be that the kinetics of the loop growth creates a flux balance between the rate of flow of interstitials to the loops and the rate of annihilation of interstitials at the loops without significantly perturbing the concentration at the loops. The second is that at the time periods we have used for measurement, most of the interstitials initially in the {311}'s have already been released, albeit over different periods of time, so that the total dose of interstitials injected into the bulk is the same although it took different amounts of time to inject that dose. Whatever the case may be, the measurements performed ensure that assumptions 1 and 2 hold.

Assumption 3, which states that all of the interstitials in the B-DSL sample remain free and can contribute to the boron diffusivity as long as they remain in the vicinity of the boron spikes, may hold the key to the discrepancy between the C_I^* value calculated here and the other theoretical results. The interstitial dose captured by the dislocation loops in the pre–amorphized samples represents all of the interstitials flowing from the {311} defects into the bulk of the wafer. However, the interstitial supersaturation which gives rise to the boron diffusivity enhancement is only due to the free interstitials. As the interstitials diffuse into the bulk of the wafer (deeper than the x_0–plane), some of them will be trapped. The ratio of free–to–trapped interstitials is the ratio of the effective diffusivity to the free diffusivity[18] (the

diffusivity of the free interstitial in the absence of trapping). Hence, in the DSL samples, only a fraction of the interstitials is accounted for. The denominator in equation 3.8 should be multiplied by the ratio of trapped-to-free interstitials. This would reduce the calculated value of C_I^* close to the theoretical values.

Evidence of the presence of traps in silicon is presented in Figure 3.12 by comparing the dissolution kinetics of {311} defects in silicon wafers grown by three different methods, namely MBE, Czochralski (CZ) and Float Zone. It can be seen from the graph that the maximum number of interstitials trapped in {311} defects is greatest for the FZ material and least for the MBE grown material. This seems to indicate that the MBE grown material has the largest number of interstitial traps. This could arise from differences in the contamination levels in the different crystal growth systems. Another probable explanation is that the low growth temperature prevents annealing out of defect clusters that might occur at higher temperatures (<700°).[18] It is also interesting to note that the presence of type II dislocation loops in the MBE grown sample does not affect the {311} dissolution, indicating that the impurity traps are more effective than the loops.

Experimentally, the effect of trapping may be compensated for by creating a type II dislocation loop layer at the same depth as the third boron spike as opposed to the first. However, in order to create a loop layer at a depth of about 0.65 μm an implant energy of ~650 keV (for Ge$^+$ ions) would be

required. Also, this implant would lead to the formation of a buried amorphous layer, so in order to create a continuous amorphous layer from the surface down, additional shallow implants (possibly two implants) would be necessary. An additional difficulty with the use of such high energy implants to form loop layers is that upon annealing the loops tend to coalese into a network due to the high concentration of interstitials beyond the amorphous/crystalline interface. As a result quantitative analysis of the interstitials trapped by the loops and any increase in this number due to dissolution of {311} defects is extremely difficult (if not impossible).

Thus a value of $2 \times 10^{27} e^{-2.7eV/kT}$ cm^{-3} obtained for C_I^* appears to be an effective value, including both free and trapped interstitials. Also, it has been shown that the interstitials that flow into the bulk can be quantitatively distinguished from the ones that flow towards the surface. This effect of the surface on defect formation and dissolution will be studied in greater detail in the next chapter.
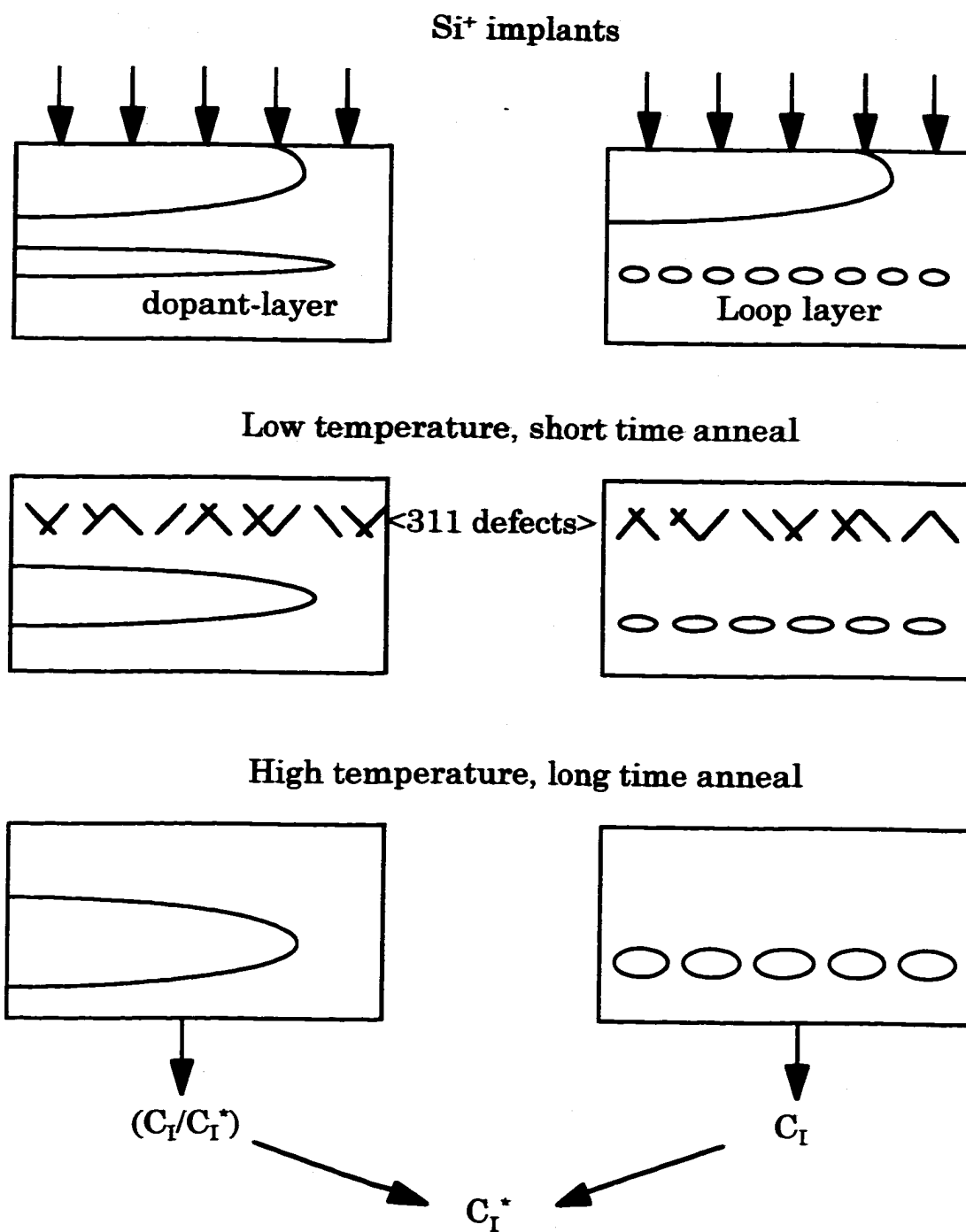
Figure 3.1 Schematic diagram of the experimental procedure used to determine the C_I^* value.
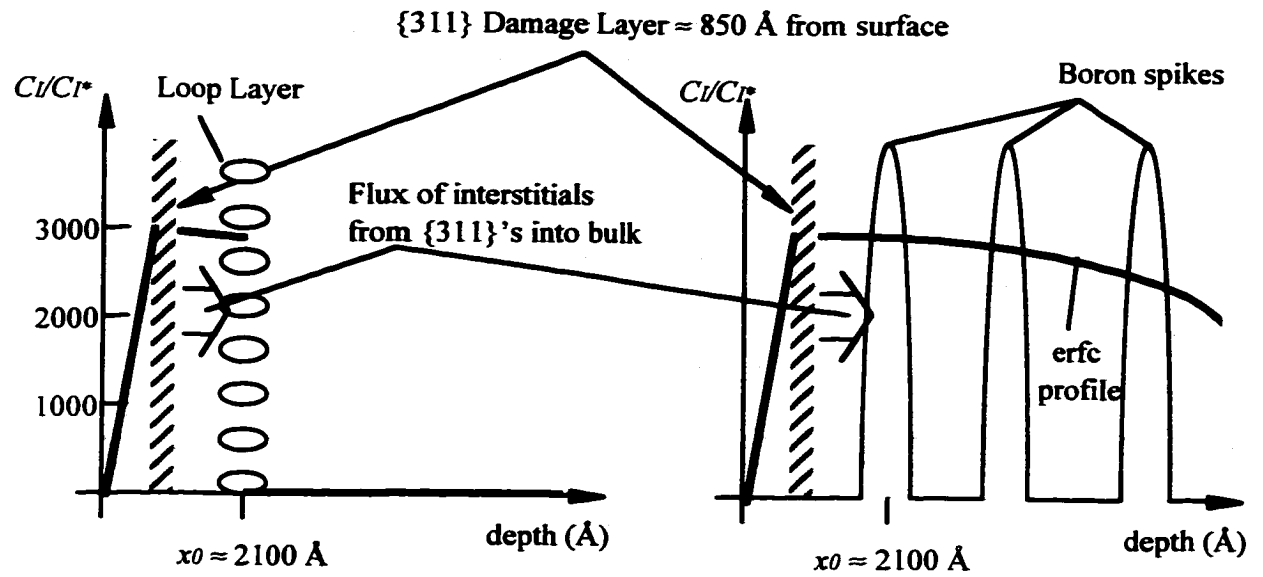
Figure 3.2 Schematic representation of the interstitial scaled concentration profile in the two types of samples used in this experiment.
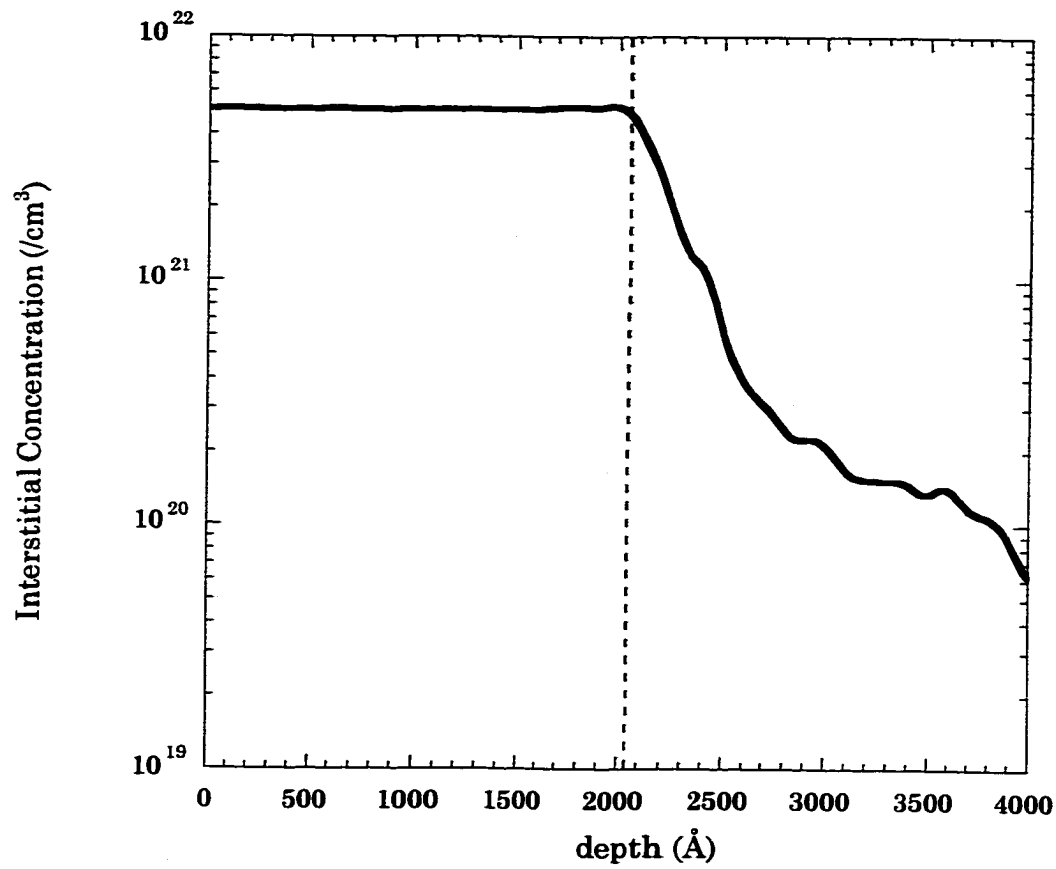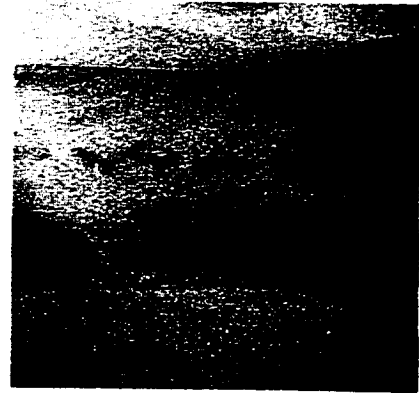
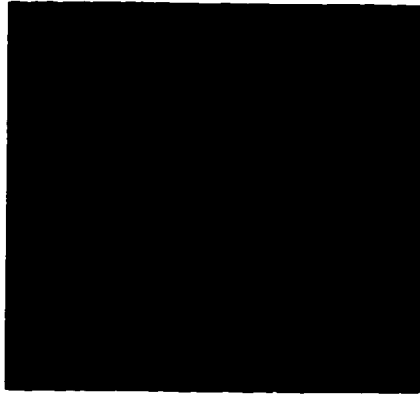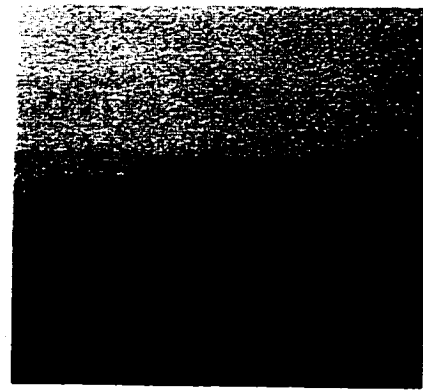**Figure 3.3 Amorphous layer depth determination using Marlowe simulations for 165 keV, 1e15/cm² As⁺.**

$T_{sub}=40°C$
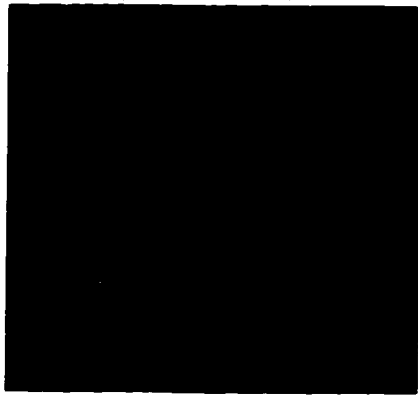
$T_{sub}=5°C$

Figure 3.4 TEM micrographs showing variation in loop distribution and loop layer depth with changing implant temperature for a constant dose of 1e15 cm^{-2} (annealed for 30 min at 900°C in flowing N$_2$).

$T_{sub}=5°C$, dose=2e15 cm^{-2}

Figure 3.5 XTEM micrograph showing formation of a wide EOR defect region for a sample implanted to a dose of 2e15 cm^{-2} (annealed for 30 min at 900°C in flowing N$_2$).

Dose = 1e14 cm^{-2}
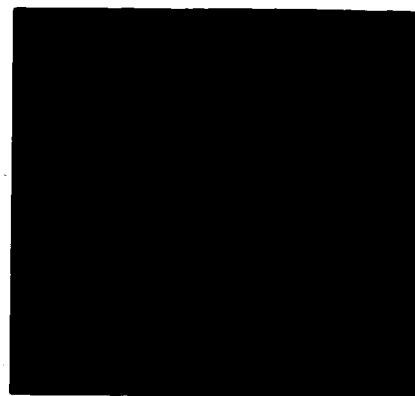
Dose = 2e14 cm^{-2}

Figure 3.6 Effect of Si$^+$ dose (40 keV implant) on the microstructure after a 750°C, 30 min. anneal in flowing N$_2$.

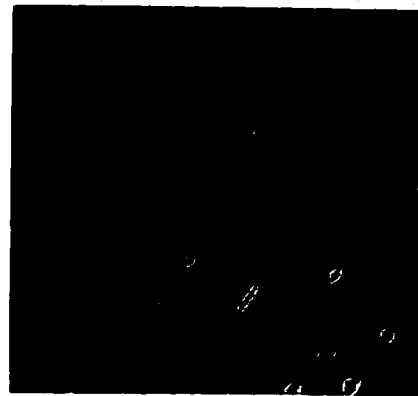a) Zero reference sample, 900°C, 30 min

4hr

16 hr

b): 685°C

Figure 3.7 PTEM micrographs of the various samples following anneals at different temperatures and various times.
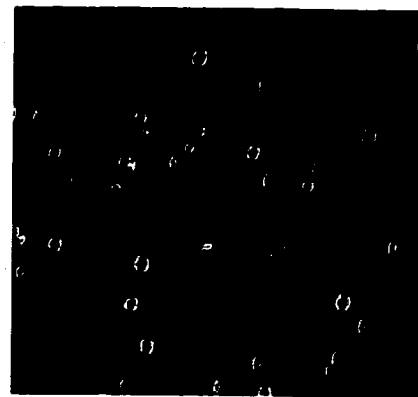
20 min   1hr

c): 750°C
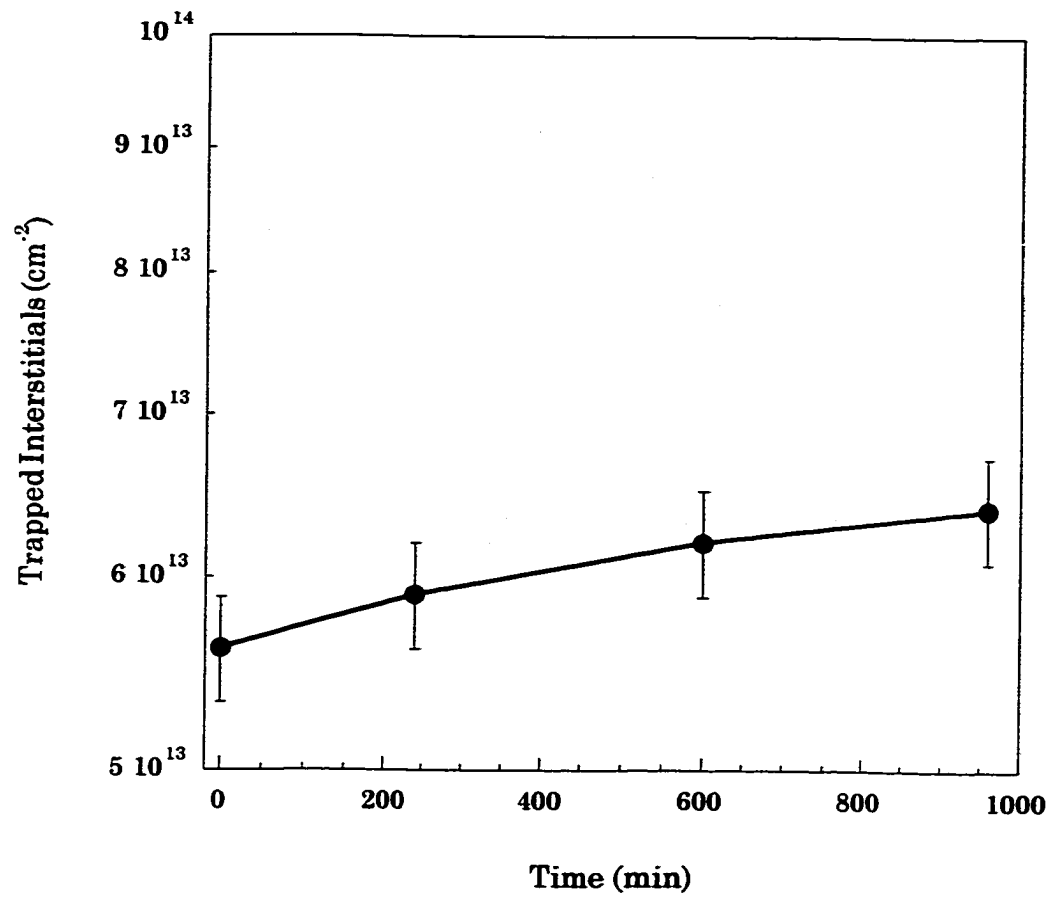

30s   60s

d): 815°C (in an RTA)

Figure 3.7 (contd.) PTEM micrographs of the various samples following anneals at different temperatures and various times.

a) 685°C

Figure 3.8 Increase in trapped interstitials vs. time for different temperature anneals.
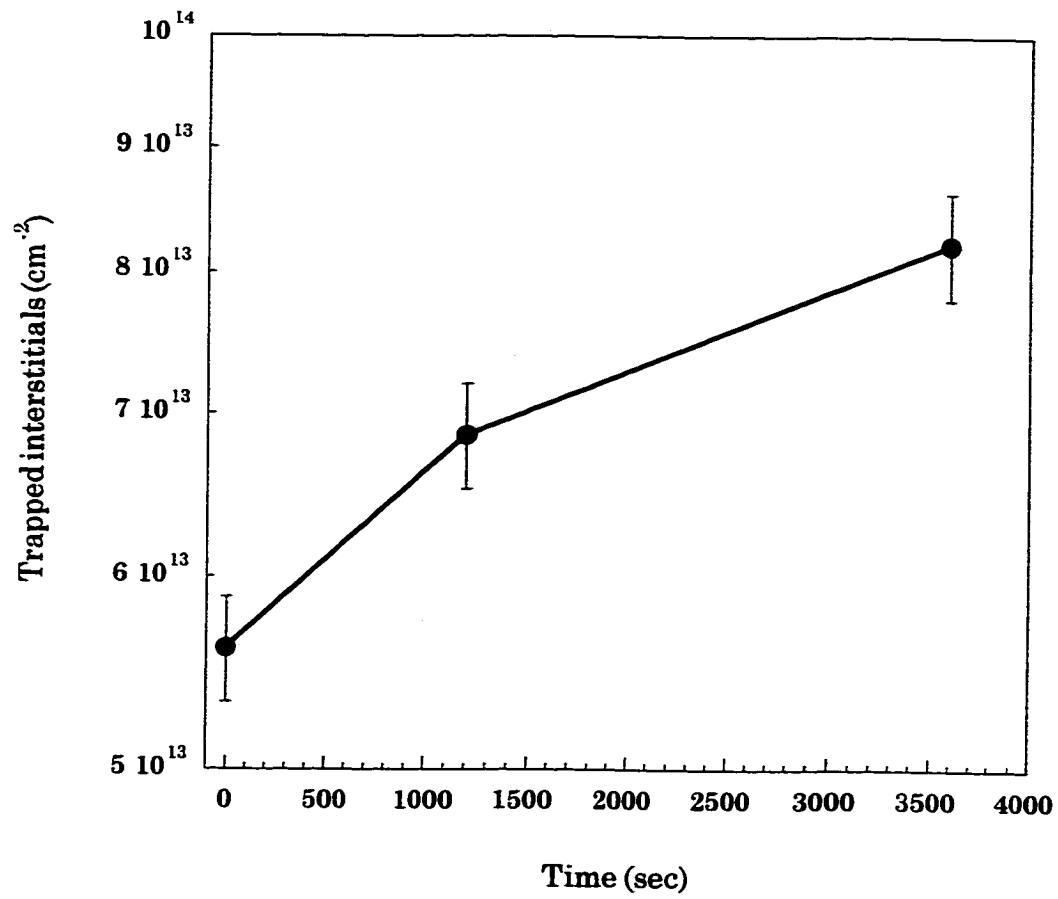
b) 750°C

Figure 3.8 (contd.) Increase in trapped interstitials vs. time for different temperature anneals.

c) 815°C (RTA)

Figure 3.8 (contd.) Increase in trapped interstitials vs. time for different temperature anneals.
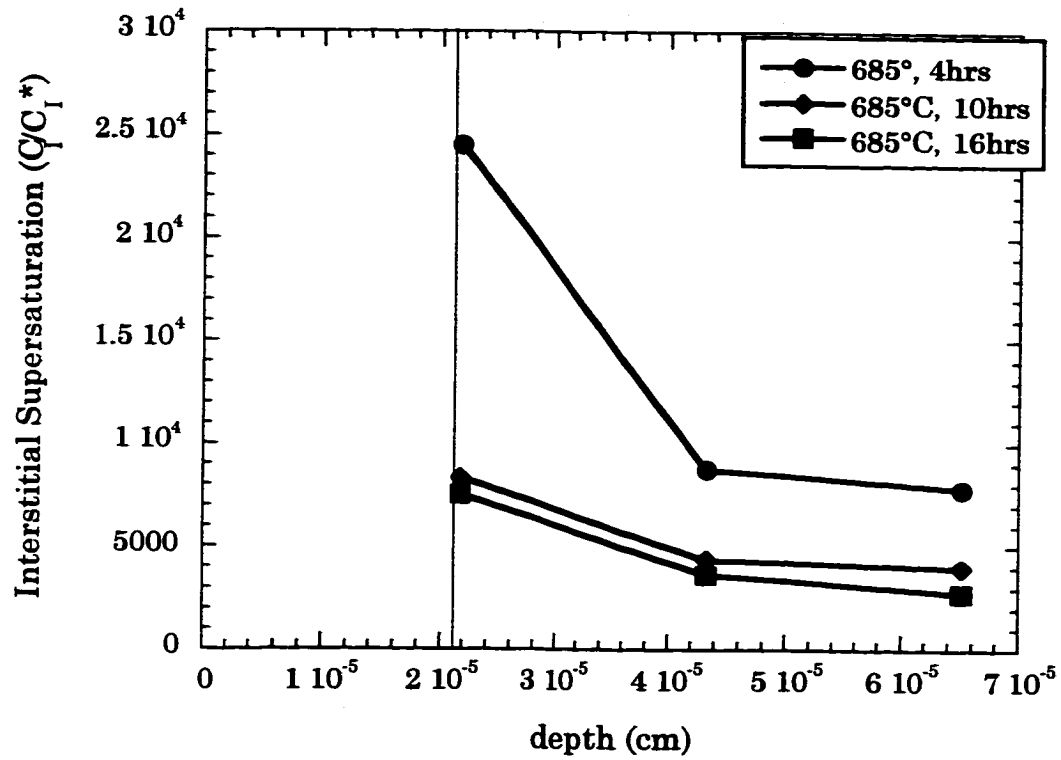
a) 685°C

Figure 3.9 Interstitial supersaturation vs. depth extracted from FLOOPS analysis of the SIMS profiles for the implanted boron DSL sample annealed at different temperatures.
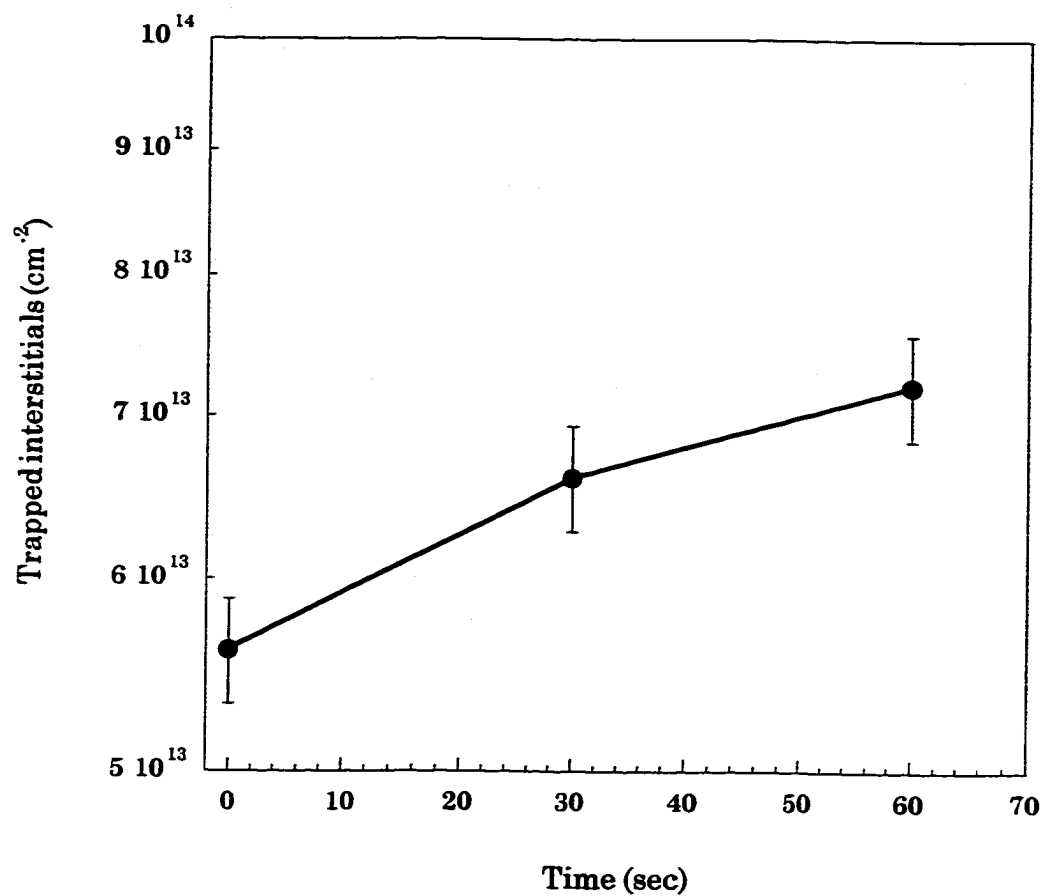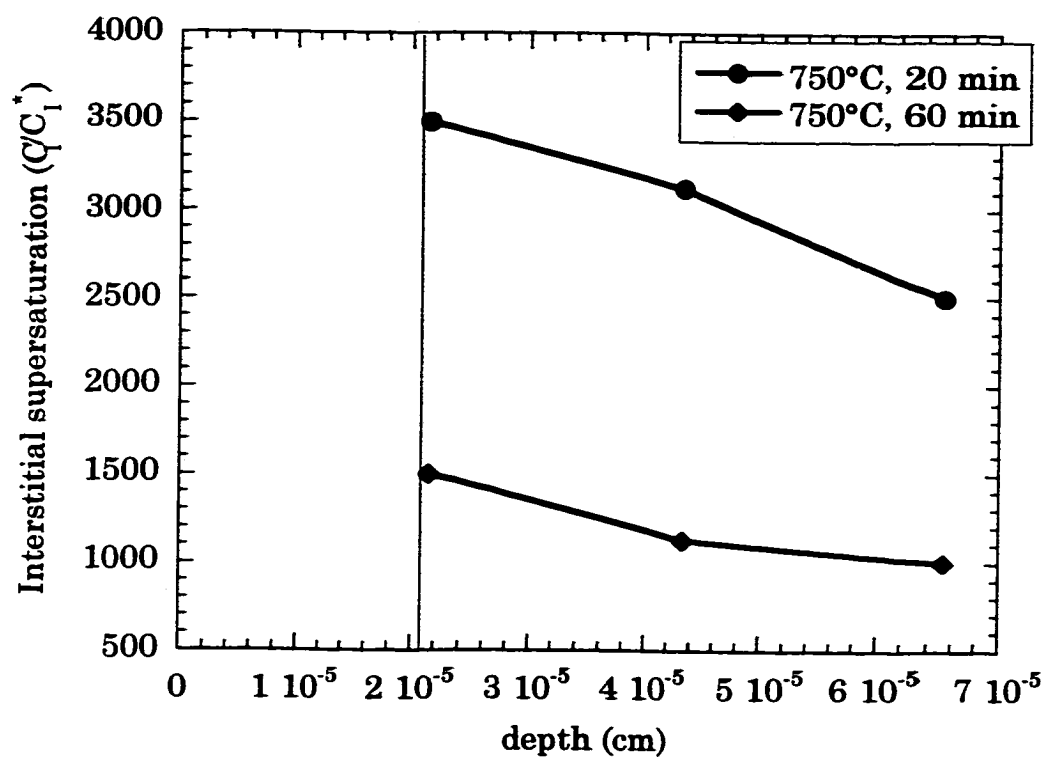
b) 750°C

Figure 3.9 (contd.) Interstitial supersaturation vs. depth extracted from FLOOPS analysis of the SIMS profiles for the implanted boron DSL sample annealed at different temperatures.
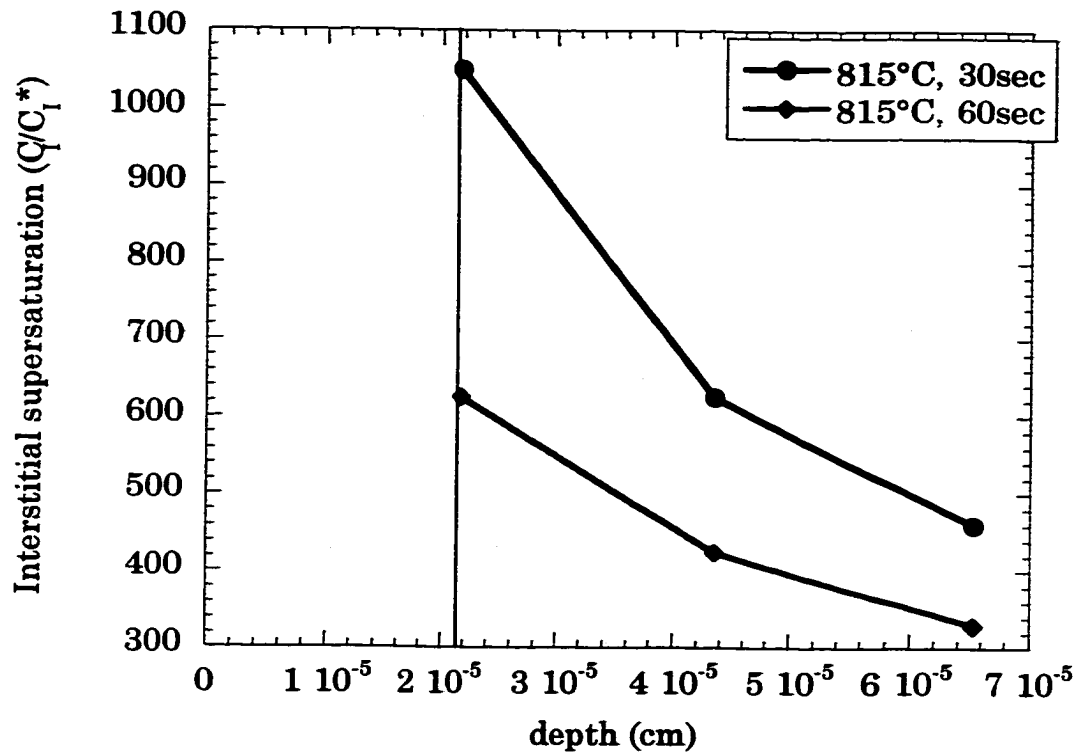
c) 815°C

Figure 3.9 (contd.) Interstitial supersaturation vs. depth extracted from FLOOPS analysis of the SIMS profiles for the implanted boron DSL sample annealed at different temperatures.
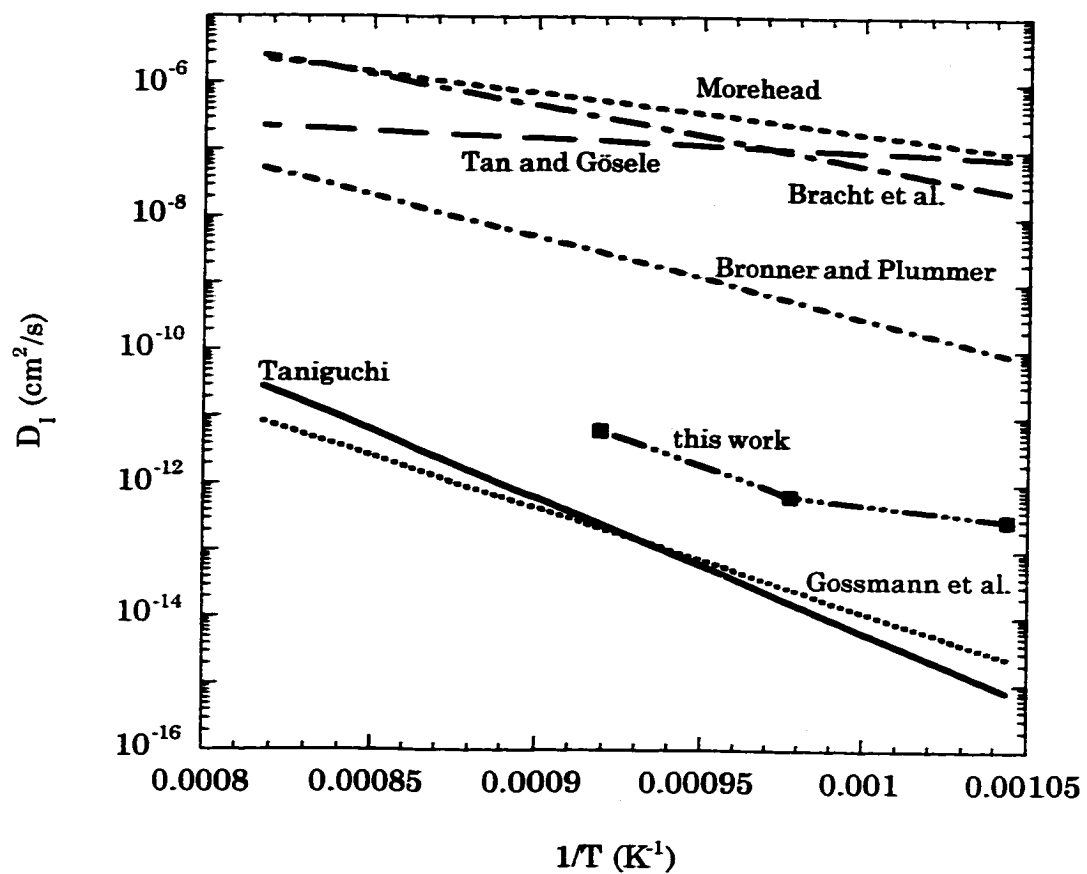
Figure 3.10 Comparison of calculated diffusivities D_I for silicon self-interstitials as a function of inverse absolute temperature.[86,16,62,81,87,65]
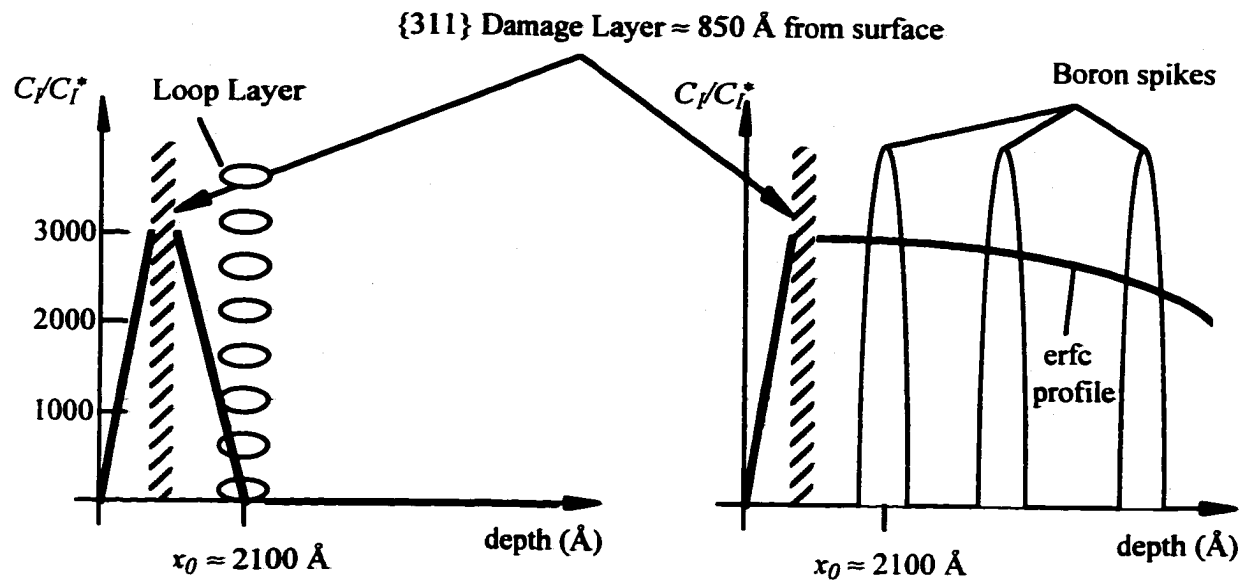
Figure 3.11 A schematic representation on the interstitial scaled concentration profile assuming pinning to a value of order unity at the loop layer.
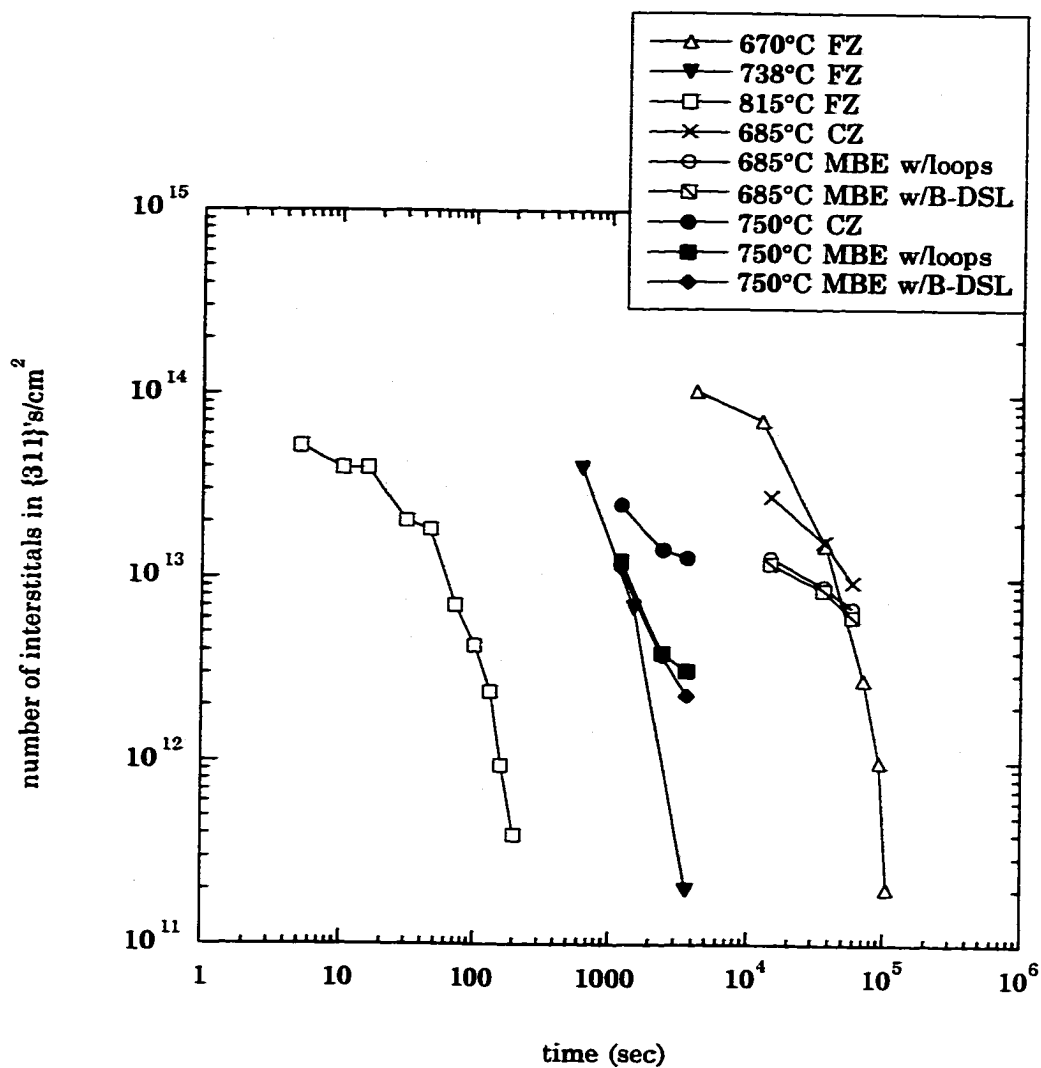
Figure 3.12 Comparison of {311} defect dissolution in the two sample sets, one with boron spikes and one with dislocation loops. Shown for comparison is data from Eaglesham et al. for {311} defect dissolution in FZ silicon.

CHAPTER 4
EFFECT OF SURFACE ON END-OF-RANGE DEFECT MORPHOLOGY AND BORON TED

For the formation of p-n junctions required for 0.18 μm and smaller technologies, the effects of implant damage on dopant diffusion become increasingly important. As device dimensions shrink dopant ions will have to be implanted at ultra-low energies (≤ 5 keV). Unfortunately, our understanding of the interaction between implant damage and dopant diffusion is limited. At low energies, the projected range R_p of the implant as well as the entire implant and damage profiles are very close to the surface. Thus the effect of the surface on the interstitial supersaturation in the near surface region following the implant and subsequent anneal becomes very important. Surface effects on the formation and evolution of extended defects and also on transient enhanced diffusion (TED) is a controversial topic and previous results have had contradictory results.

Meekison[7] using controlled etching reduced a 3900Å amorphous layer to 2000Å and 800Å and then annealed the samples in nitrogen at 1100°C. TEM showed that the number of interstitial atoms per unit area trapped in the EOR dislocation loops reduced with a decrease in amorphous layer thickness. Also, the loss of interstitials from dislocation loops was faster at

82

smaller thicknesses. Similar results have been reported by other researchers as well[88,89]. They attributed this effect to either the reduced distance over which the interstitals have to diffuse to the surface, or glide of the loops to the surface due to an image force. More so, in all cases, the morphology of the type II defects was reported to be in the form of loops.

In a similar study, Omri et al.[8] amorphized a (100) Si wafer with Ge⁺ and then etched away increasing thickness of the amorphous layer. The etched samples were then annealed at 1000 or 1100°C in argon for 10 seconds and then examined by PTEM. They reported that irrespective of the distance of the amorphous/crystalline (a/c) interface to the surface, the mean size and density of the loops and thus the total number of interstitials trapped by the loops were same. They concluded that the a/c interface acts as a diffusion barrier for the Si interstitials during the nucleation stage and that the surface acts mirrorlike (i.e. is not a strong sink) during the coarsening stage. It should be noted that the thinnest amorphous layer studied was ~300Å and that the etching process left behind an extremely rough surface. Also, no change in the morphology of the loops was reported.

It is possible that the minimum distance of 300Å was not small enough to observe a surface effect. Agarwal et al.[10] estimated a surface recombination length of < 100Å from experiments involving TED of B marker layers from a Si⁺ implant and anneal. They showed that as the Si⁺ implant energy was reduced from 20 keV to 1 keV, the boron diffusivity enhancement

decreased and extrapolated to 1 for a 0 keV implant. Hence the formation of shallow junctions would not be limited by poor interstitial recombination at the surface.

However, TEM analysis of 5 keV Si^+ implants, with non-amorphizing (1e14 cm^{-2}) and amorphizing (3e14 cm^{-2}) doses showed the formation of elongated extended defects after a 750°C anneal.[90] These defects were identified as zig-zag {311} defects and were shown to be extremely stable despite the low surface proximity (< 100Å) and dissolved slower than regular {311} defects.

This chapter will focus on the effect of the proximity of the silicon free surface to the end-of-range damage on the morphology of the EOR damage as well as TED of a deeper boron marker layer.

4.1 Experimental Approach

A schematic of the experimental method used is shown in figure 4.1. The samples used in this study consist of CVD grown epilayers on CZ (100) Si substrates. The epilayer has a B-spike grown in at a depth of ~5000Å from the surface. Qualification of the sample quality has been discussed in section 2.1. Sample pieces were implanted with Si^+ ions at an energy of 10 keV and to a dose of 1e15 cm^{-2}. The implants were done at room temperature at two different dose rates (5μA/cm² and 25 nA/cm²) and at liquid nitrogen temperature (77K) at a dose rate of 25 nA/cm². Under these conditions a

surface amorphous layer was formed. Table 4.1 shows the amorphous layer depths as measured by spectroscopic ellipsometry for the different implant conditions.

Table 4.1: Comparision of amorphous layer depths for combinations of different implant conditions (energy = 10 keV and dose = 1e15 cm^{-2} for all samples).

Temperature	Dose rate	α layer depths (Å) before CMP	α layer depths (Å) after CMP
RT	5 μA/cm²	250	175, 50
RT	25 nA/cm²	175	50
LN₂ (77K)	25 nA/cm²	220	175,50

Using a chemo-mechanical polish described in section 2.5 the amorphous layer depths were reduced to values shown in column 4 of Table 4.1. The CMP was carried out in conjunction with spectroscopic ellipsometry so as to prevent overpolishing of the amorphous layers. A piece of each sample (i.e. every combination of implant condition and amorphous layer thickness) was then annealed at 750°C in a flowing N₂ ambient for various times, 15 min, 1 hr and 6 hrs. The samples were then analyzed by SIMS and

PTEM/XTEM to determine the boron profiles and the defect microstructures respectively. The SIMS profiles were imported into FLOOPS and analyzed to determine the B diffusivity enhancement as described in section 2.6.

In order to determine just the effect of the dose rate of the Si^+ implants on the amorphous layer depth and the EOR defect morphology, a set of four samples were implanted with 10 keV Si^+ ions to a dose of 1e15 cm^{-2} at dose rates of 0.06, 0.12, 0.24 and 0.48 mA/cm^2. These implants were done in the same implanter and on CZ (100) Si wafers from the same batch. Amorphous layer depths were determined by spectroscopic ellipsometry and confirmed by XTEM. Pieces of each wafer were then annealed at 750°C in a flowing N_2 ambient for various times (15, 90 and 360 min) and then analyzed by PTEM.

4.2 Experimental Results and Discussion

PTEM using a g_{220} weak beam dark field (WBDF) condition was used to image the EOR defects. The PTEM micrographs are shown in Figures 4.2 through 4.4 for the samples used to study the effect of surface proximity on the defect morphology, i.e. the samples listed in Table 4.1. It can be seen from the PTEM micrographs in Figure 4.2 that when the amorphous layer depth is reduced by CMP, the morphology of the EOR damage exhibits a change; for amorphous layer thicknesses of 250Å the EOR defects are in the form of well formed type II dislocation loops which increase in size with anneal time with very little change in defect density, as well as {311} defects that dissolve

rapidly with time or unfault to form loops. However for samples with an initial amorphous layer of 50Å, the defect morphology shows a large number of {311}'s and a few small dislocation loops. The {311} defects appear similar to the zig-zag defects reported by Agarwal et al.[90] They are wider than regular {311} defects when seen in plan-view and have a corrugated appearance when viewed in high resolution cross-section (Figure 4.10). The {311} defects appear to coarsen from 15 min to 60 min and then dissolve with very few defects remaining after 6 hrs. The samples that start of with an amorphous layer thickness of 175Å show an intermediate behavior. After a 15 min anneal the defect morphology and defect density looks very similar to the 250Å sample but with increase in time both the loops and the {311} defects dissolve though the dissolution is not as dramatic as in the 50Å samples. This evolution of the defect density has been quantified and plotted in Figure 4.11.

When the dose rate of the Si^+ implant is reduced to 25 nA/cm^2, the thickness of the as-implanted amorphous layer decreases from 250 to 175Å. With decreasing dose rate the shallower a/c interface leads to a significant increase in the net excess interstitials in the EOR region[91]. So, as expected, upon annealing, the number of interstitials trapped in the EOR defect layer is higher. This is obvious when Figure 4.3 is compared to Figure 4.2. In fact, the number of interstitials is so high that the loops appear to be networking. It should be noted that the low dose rate samples do not contain any {311} type

defects. It is possible that the presence of an extremely high interstitial supersaturation favors the nucleation of loops as opposed to {311} defects. Another possibility is that the higher a/c interface roughness caused by the lower dose rate implant[92] combined with a higher population of net excess interstitials leads to a greater number of nuclei of critical size for loop formation. It can also be seen from Figure 4.3 that the PTEM micrographs for the 175Å, 15 min sample and the 50Å, 15 min sample are very similar. Thus the presence of a higher interstitial supersaturation and a larger number of loop nuclei acts as a barrier and reduces the effect of the surface during the nucleation process. But the change in surface proximity does seem to affect the loop kinetics after nucleation; the loops in the 50Å sample appear to dissolve with an increase in annealing time while the loops in the 175Å appear to coarsen with very little dissolution, if any. It should be noted from Figure 4.3 that the 50Å samples have loops that intersect the surface that this is probably the reason for the increased dissolution. Unfortunately, this along with networking of the loops and their non-uniform shape makes quantification of the defect density and trapped interstitial dose extremely difficult.

Decreasing the implant temperature from room temperature to 77 K led to an increase in the amorphous layer thickness from 175 to 220Å. It has been proposed that this increase is due to a decrease in the effective threshold damage density[12] and the effect has also been reported by other researchers.[93]

This results in a decrease in the concentration of atoms coming to rest in the EOR region beyond the a/c interface without affecting the final implanted ion profile. The above result can also be simulated using UT-MARLOWE [94] which is a software platform for Monte-Carlo simulation of ion implantation. The results are summarized in Table 4.2 below where column 3 represents the integral of the total interstitial profile below the a/c interface.

Table 4.2: Results of UT-MARLOWE simulations of a 10 keV Si^+ implant to a dose of 1e15 cm^{-2} at a dose rate of 25 nA/cm^2.

Implant Temperature	α-layer depth (Å)	Intersititals beyond α/c interface (cm^{-2})
RT	217	4.4e15
LN_2 (77K)	260	3.7e15

Even though these results show the right trends in values, obviously, the values of the amorphous layer thickness from the simulations vs. the experimental techniques are different. This is because UT-MARLOWE does not correctly account for all the physical mechanisms involved in modeling dose rate effects for Si^+ self-implantation. For example, two simulations of a 1e15/cm^2 10 keV Si^+ implant at dose rates of 25 nA/cm^2 and 5 mA/cm^2

resulted in the same amorphous layer thickness of 239Å. As a result the simulated dose rate effects are different from those observed experimentally.

Since the thicker amorphous layer for the LN_2 implant also implies fewer recoiled atoms beyond the a/c interface, the number of interstitials trapped in EOR defects upon annealing should also be less. This can be seen in the PTEM micrographs in Figure 4.4 compared to those in Figure 4.3. The number of trapped interstitials in EOR defects is lower for the LN_2 implant samples as compared to the samples implanted at room temperature , irrespective of the initial amorphous layer thickness. Even though the defect density for the 220Å sample is higher than the 175Å and 50Å samples after the 15 min anneal, in all cases the defects seem to have dissolved upon annealing for 1 hr (Figure 4.12). It should be noted that the data point for the 1 hr samples represents one defect per negative (9.5 cm x 7 cm) at a magnification of 50,000. Also, the RT and the LN_2 samples were implanted in different implanters and this could have some bearing on the interpretation of the results.

SIMS measurements were taken from each annealed sample to obtain the final boron marker layer profiles. The position of the boron peaks were adjusted by taking into account the thickness of the amorphous layer that was removed by CMP and then translated to coincide with the peak position of an as deposited control sample. After this, the dose of boron in the spike was normalized to equal the dose in the control sample. The profiles were

imported into the process simulator FLOOPS and the time averaged boron diffusivity enhancements ($<D_B>/D_B^*$) were determined. Figures 4.5 through 4.7 show the plots of $<D_B>/D_B^*$ vs. time for the three different implant conditions. Examination of these plots show that generally changing the thickness of the amorphous layer has a minimal effect on the diffusion of the buried boron marker layer. This is in agreement with Huang[72] and Robertson's[95] results showing that above the amorphization threshold, an increase in the implant dose or implant dose rate has no effect on boron diffusivity in a buried marker layer thus suggesting that the boron diffusivity is not affected by the physical processes occuring in the amorphous region and the EOR region where the defects occur i.e only the point defects present below the EOR damage layer contribute to the boron diffusivity and to a first order this is similar in all cases.

A comparison of the amorphous layer depths as determined by XTEM (average of 10 readings) and spectroscopic ellipsometry was carried out on the CZ (100) Si samples implanted with 10 keV Si^+ to a dose of 1e15/cm^2 and at dose rates of 0.06, 0.12, 0.24 and 0.48 mA/cm^2. The results are plotted in fig. 4.8. With increasing implant dose rate there is an increase in the amorphous layer thickness. However, as can be seen from the graph, there is a consistent difference between the values measured by the two different techniques. Since the SE readings were used for all the samples, the sample sets that are

supposed to have the same amorphous layer thicknesses are expected to be consistent. Possible reasons for this discrepancy are;

1. Error in the calibration of the HRTEM i.e. the actual magnification of the image is slightly different from the magnification printed on the TEM negative.

2. Effect of the surface oxide layer on the reading of the amorphous layer depth. In all cases, the oxide layer thickness as measured by SE was ~ 10Å less than that measured by HRTEM.

3. Error in the model used to fit the experimental values of Ψ and Δ to the theoretical ones (see section 2.4).

After an anneal at 750°C for various times (15, 90 and 360 min), these samples were analyzed by PTEM using a g_{220} WBDF condition and the micrographs in fig. 4.9 show the variation in defect morphology. It is quite obvious from the micrographs after the 15 min anneal that as the dose rate of the implant is increased from 0.06 mA/cm^2 to 0.48 mA/cm^2, the density of EOR loops reduces. Any change in the {311} defect density is not immediately apparent from these images and therefore has been quantified along with the loop defect density (Figure 4.13) and the trapped interstitial dose (Figure 4.14). The data in Figure 4.13 indicates that as the dose rate of the implant is increased, there is a tendency to form {311} defects instead of dislocation loops. However the total defect density is unchanged. Consequently, the contribution of the {311} defects to the total trapped interstitial dose increases while the contribution from the dislocation loops decreases. Also, the total trapped interstitial dose in extended defects decreases with an

increase in implant dose rate which is consistent with previous results involving RT and LN$_2$ implants.

In order to study the evolution of the defects with time, the samples implanted at dose rates of 0.06 mA/cm^2 and 0.48 mA/cm^2 and annealed for 90 and 360 min. were also quantified. The variation in defect densities and trapped interstitial dose as a function of time for these two dose rates are plotted in Figure 4.15 and Figure 4.16 respectively. It can be seen from these graphs that for both dose rates the {311} defects show similar dissolution with time. For the higher dose rate, there is an increase in loop density from 15 min. to 90 min. due to unfaulting of {311} defects. Since the initial population of {311} defects is relatively low for the low dose rate sample, there is no corresponding increase in loop density, in fact, it remains constant with time. The effect of the differences in population of {311} defects vs. dislocation loops also leads to differences in the graph of total defect density with time; the higher dose rate sample shows a continuous decrease in total defect density due to a strong influence of the {311} dissolution whereas the low dose rate sample shows decrease in total defect density during the initial time step only.

4.3: Proposed Model: Effect of Amorphous Layer Thickness, Implant Temperature and Dose Rate on Defect Evolution

When the thickness of the amorphous layer is decreased by CMP to 50Å prior to an anneal there is a change in the defect morphology from

dislocation loops to zig-zag {311} defects. These {311} defects show a more rapid dissolution than the dislocation loops in samples with thicker initial amorphous layer thicknesses with very few defects remaining after a 6 hr. anneal. At the annealing temperature of 750°C used in these experiments, Frenkel pair recombination is completed within ~5 secs whereas the α-layer regrowth is over in a few milliseconds. This implies that the point defects in the EOR region "see" the surface before Frenkel pair recombination is complete. Previous work[96] has shown that the faster moving vacancies annihilate at the surface first and at lower temperatures (350°C) while the interstitial clusters break up and migrate to the surface at higher temperatures (500°C). A possibility is that the removal of the vacancies leaves behind a higher interstitial supersaturation for the thinner amorphous layers and this could cause the preferential evolution of {311} defects. However this is contrary to the dose rate study which showed that the higher interstitial supersaturation leads to preferential nucleation and growth of dislocation loops. This leaves us with the possibility that the formation of the {311} defects is due to a surface induced strain or image force[88] which extends down to the EOR damage region when the amorphous layer is reduced to 50Å but dose not affect the EOR region for thicker amorphous layers. This strain or image force could affect the formation of clusters and prevent the formation of critical nuclei required for the growth of dislocation loops.

The number of trapped interstitials in EOR defects decreases with decrease in implant temperature from RT to 77K. After a 1 hr the defects seem to have dissolved for all α-layer thicknesses. This is because the thicker amorphous layer for the LN_2 implant also implies fewer recoiled atoms beyond the a/c interface, the number of interstitials trapped in EOR defects upon annealing should also be less.

The reason for the decrease in trapped interstitial dose in extended defects can be explained as follows; increasing the implant dose rate from 0.06 mA/cm^2 to 0.48 mA/cm^2 leads to an increase in the amorphous layer thickness from 191Å to 230Å. This results in a decrease in the concentration of the net excess interstitials coming to rest beyond the amorphous/crystalline interface for thicker amorphous layers. Since the transition region from amorphous to crystalline silicon (a region of dark strain contrast when viewed under a bright field condition) is approximately the same for the samples irrespective of the dose rate,[95] it follows that the interstitial supersaturation will be highest for the sample with the thinnest amorphous layer thickness. Since the defect density is same for all dose rates but the density of dislocation loops decreases with increase in dose rate, it follows that a higher interstitial supersaturation in the EOR region either

1. creates nuclei of larger critical radius which favors the nucleation of dislocation loops to {311} defects or

2. favors the rapid unfaulting of {311} defects to form dislocation loops.

Figure 4.14 shows that after a 15 min anneal the interstitial dose trapped in defects for the 0.06 mA/cm² sample is about 2.5X more than the trapped interstitial dose in the 0.48 mA/cm² sample. This correlates well with the net excess interstitial dose (NEI) calculated from a UT-MARLOWE 5.0 simulation of a 10 keV, 1e15/cm² Si⁺ implant (Table 4.3). The numbers in the table below show that as the α-layer thickness decreases from 230Å to 191Å, the NEI increases by 1.7X. However, this dose not correlate with the trapped interstitial dose for the above two samples after 6 hrs where the 0.48 mA/cm² sample shows a higher trapped interstitial dose than the 0.06 mA/cm² sample. This might be due to a higher error in the counts since the defects in the 0.48 mA/cm² sample show very irregular shapes.

Table 4.3: Net excess interstitials (NEI) beyond the a/c interface as a function of implant dose rate and amorphous layer thickness for a 10 keV, 1e15/cm² Si⁺ implant as simulated by UT-MARLOWE 5.0

Dose rate (mA/cm²)	α-layer thickness (Å)	Trapped interstitial dose after 15 min (#/cm²)	NEI (#/cm²)
0.06	191	3.05e14	1.7e14
0.48	230	1.2e14	1e14

4.4 Summary

In this chapter, the previous literature outlining the effect of surface proximity on the evolution of end of range defects was reviewed. Most of the previous work has been on samples with amorphous layer thickness greater than 300Å. With an increase in the use of ultra-low energy implants it was felt that a study with thicknesses less than that (i.e. 300Å to ~50Å) was required. Experiments were carried out with samples implanted at different dose rates and at different temperatures keeping the implant energy and dose fixed at 10 keV and 1e15/cm² respectively and based on the results, a model was proposed to explain the effect of amorphous layer thickness and implant dose rate on EOR damage evolution.
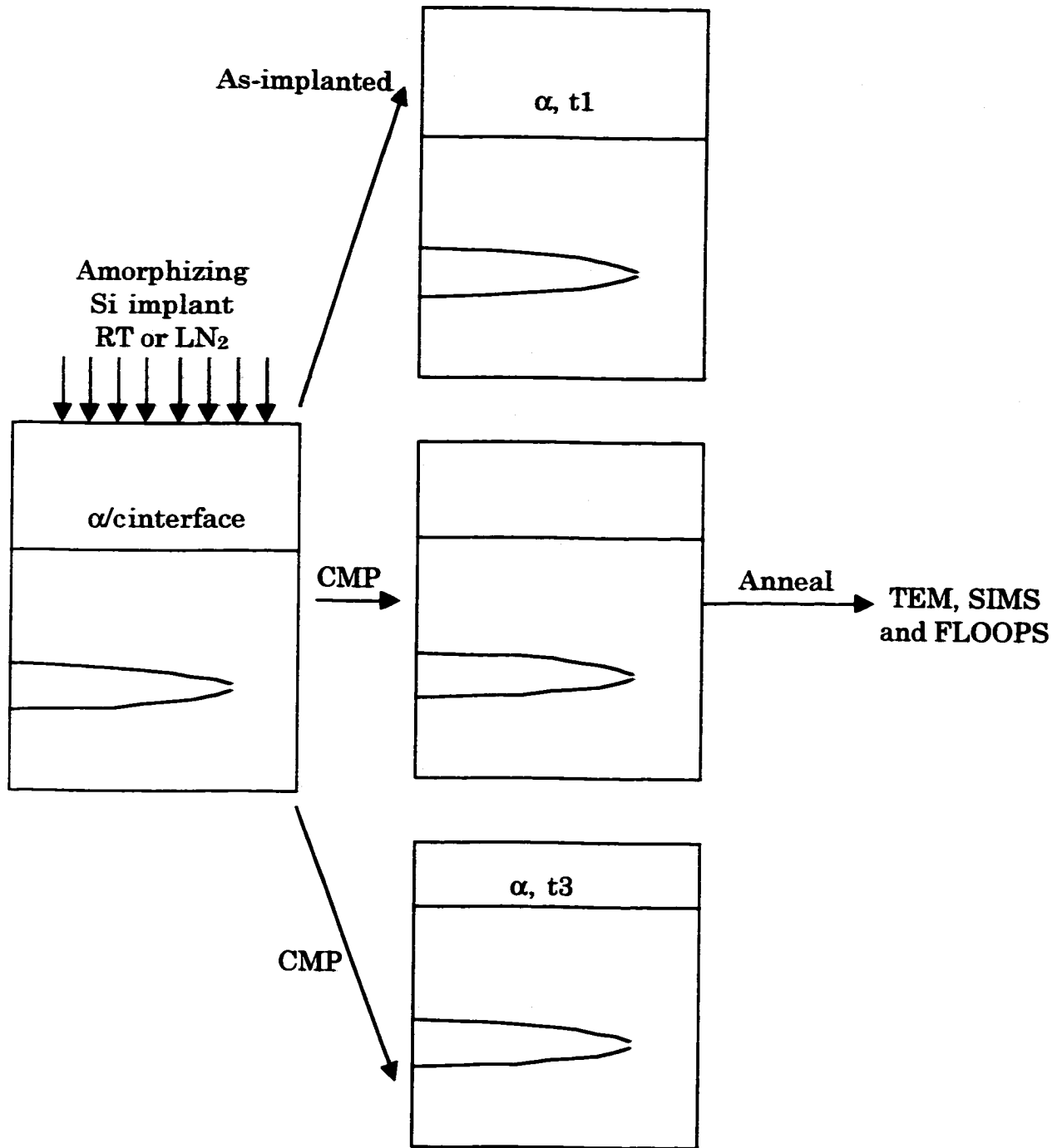
Figure 4.1 Schematic diagram of the experimental procedure used to study the effect of surface proximity on the morphology of extended defects formed beyond the a/c interface.
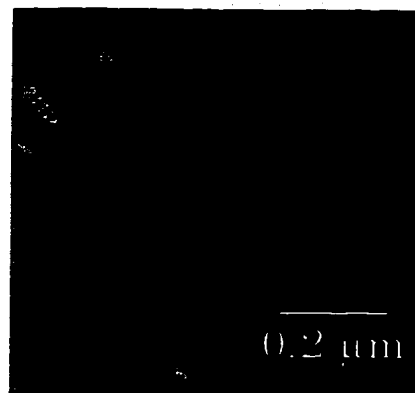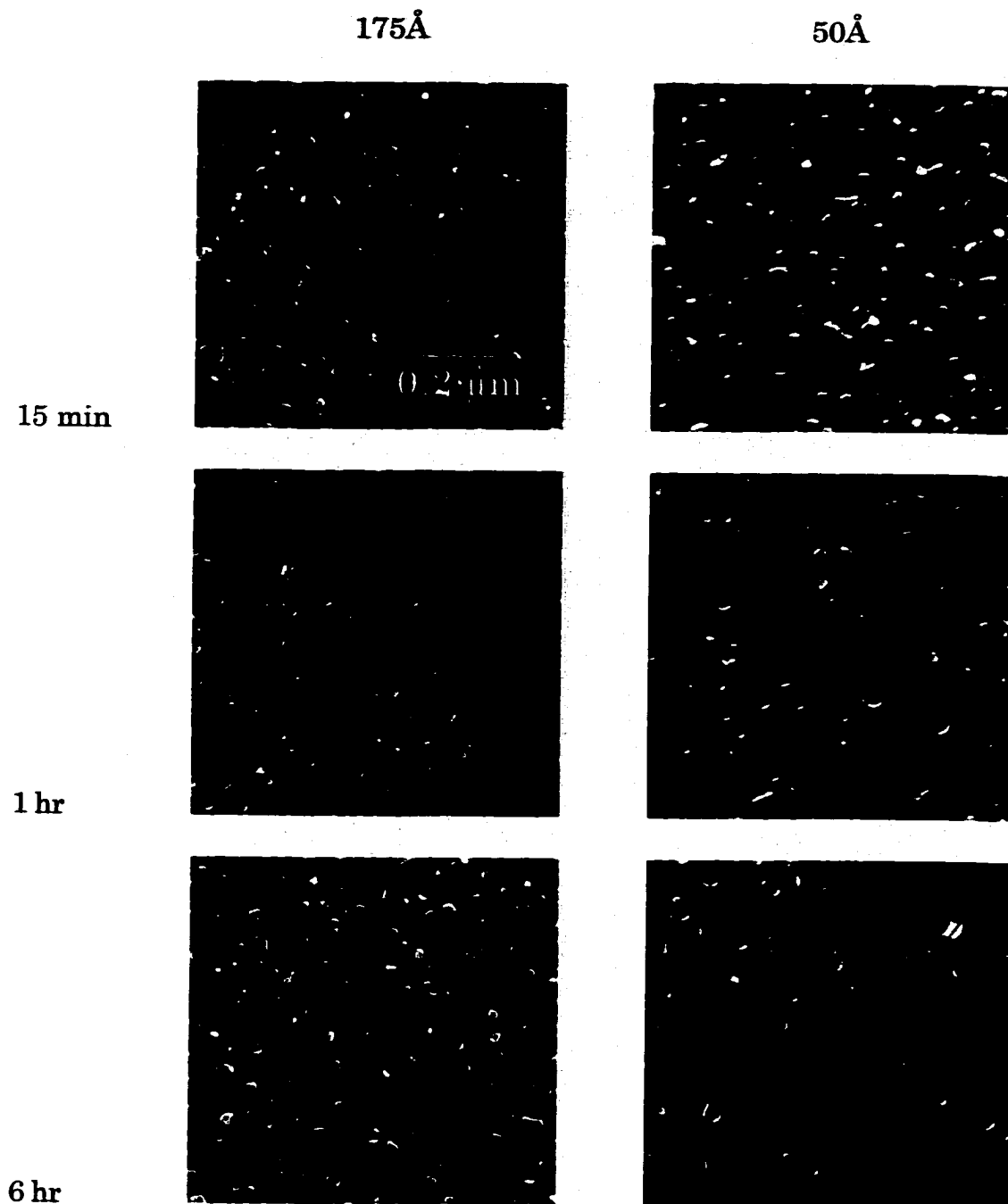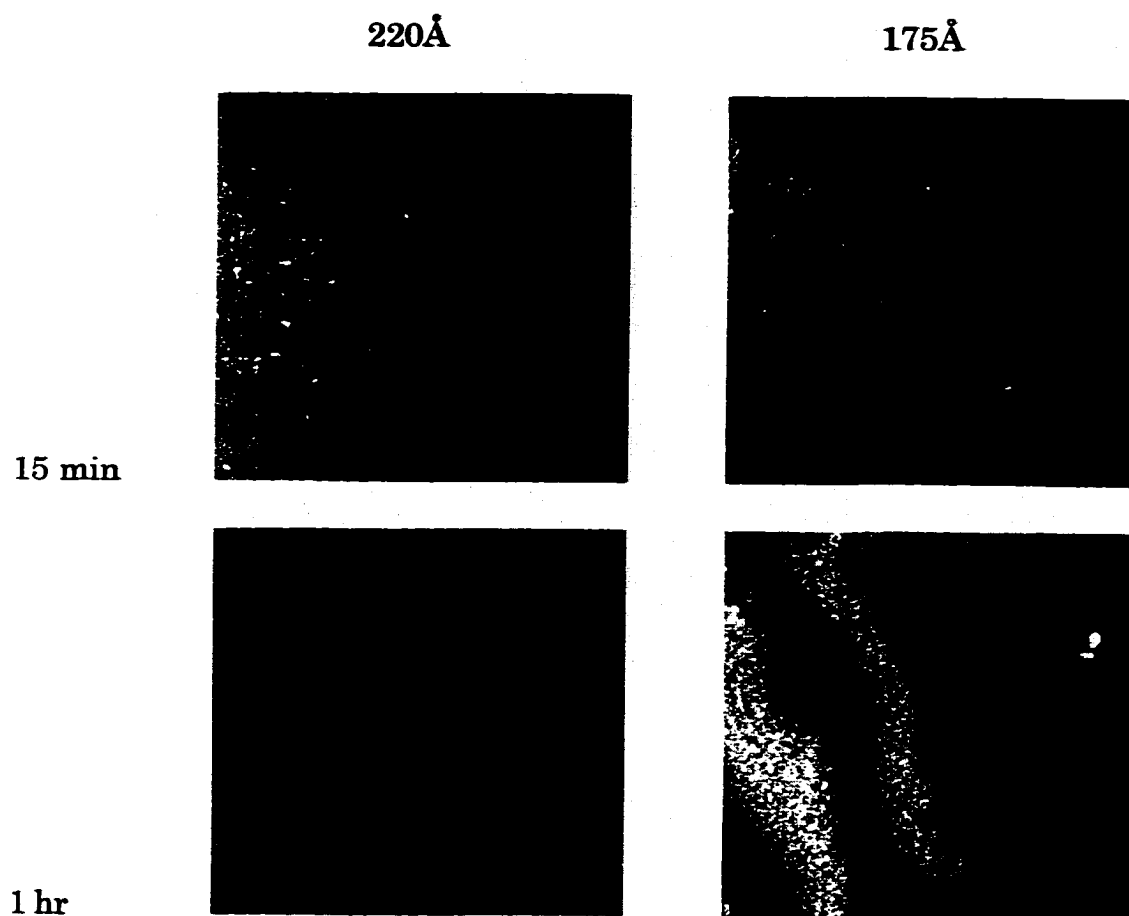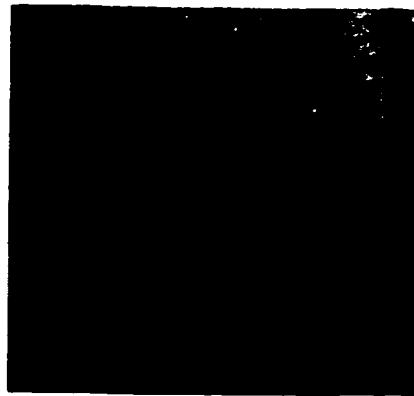
250Å   175Å

15 min

1 hr

6 hr
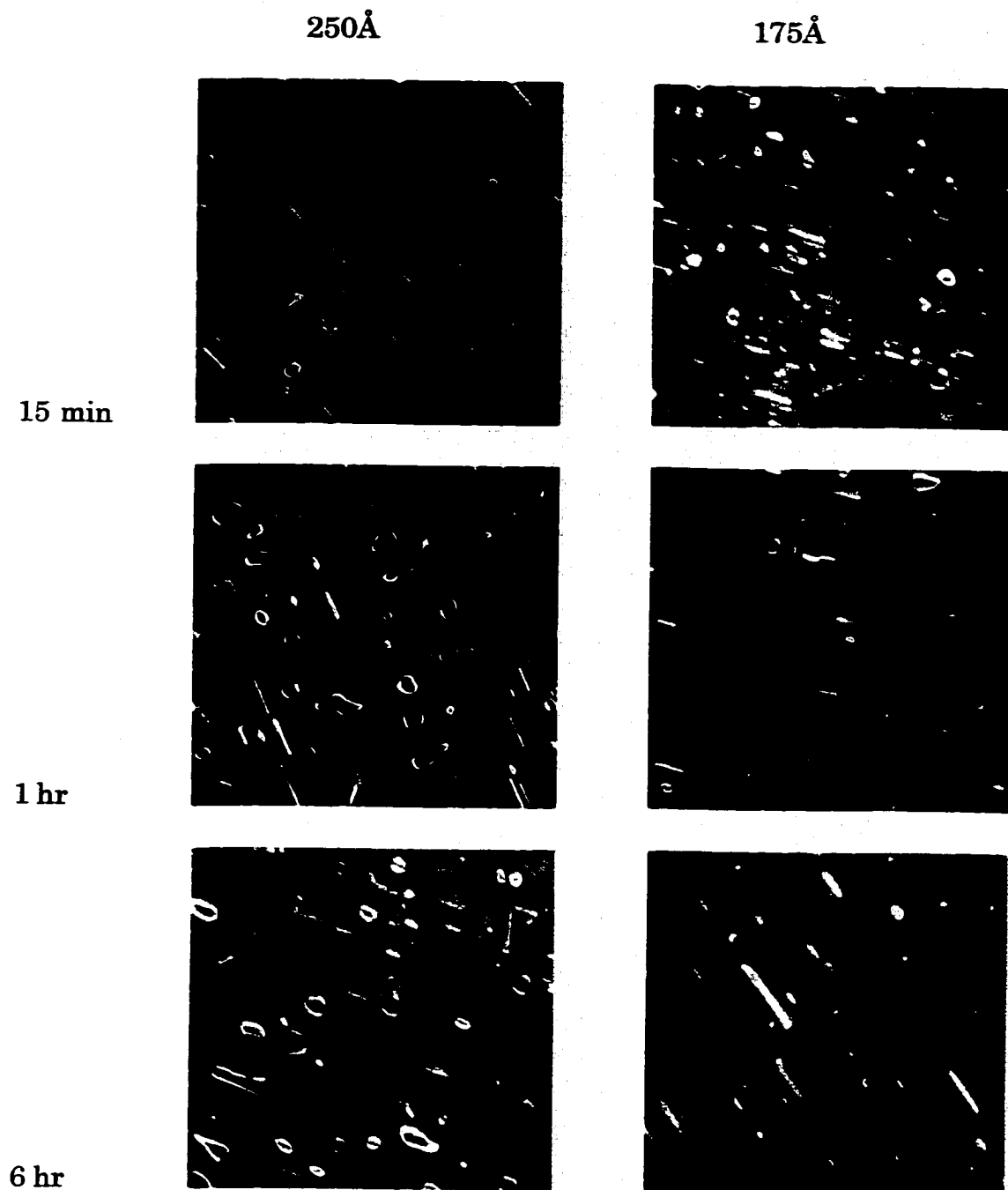
Figure 4.2 PTEM micrographs of the end-of-range damage as a function of annealing time and amorphous layer thickness. Samples were implanted at room temperature with 10 keV Si^+ ions to a dose of 1e15 cm^{-2} and at a beam current of $5\mu A/cm^2$ and then annealed at 750°C in a flowing N_2 ambient.
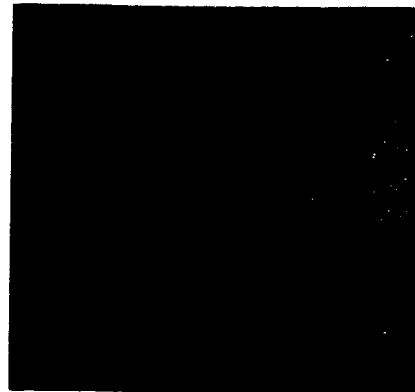
50Å

15 min
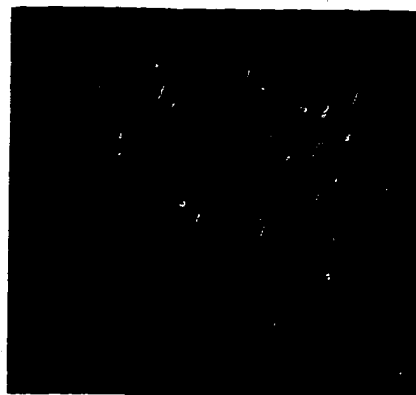
1hr

6hr

Figure 4.2 (contd.) PTEM micrographs of the end-of-range damage as a function of annealing time and amorphous layer thickness. Samples were implanted at room temperature with 10 keV Si$^+$ ions to a dose of 1e15 cm^{-2} and at a beam current of 5μA/cm^2 and then annealed at 750°C in a flowing N$_2$ ambient.

175Å   50Å

15 min

1 hr

6 hr

Figure 4.3 PTEM micrographs of the end-of-range damage as a function of annealing time and amorphous layer thickness. Samples were implanted at room temperature with 10 keV Si^+ ions to a dose of 1e15 cm^{-2} and at a beam current of 25nA/cm^2 and then annealed at 750°C in a flowing N_2 ambient.

220Å   175Å

15 min

1 hr

Figure 4.4 PTEM micrographs of the end-of-range damage as a function of annealing time and amorphous layer thickness. Samples were implanted at liquid nitrogen temperature (77K) with 10 keV Si^+ ions to a dose of 1e15 cm^{-2} and at a beam current of 25nA/cm^2 and then annealed at 750°C in a flowing N_2 ambient.

50Å

15 min

1 hr

Figure 4.4 (contd.) PTEM micrographs of the end-of-range damage as a function of annealing time and amorphous layer thickness. Samples were implanted at liquid nitrogen temperature (77K) with 10 keV Si^+ ions to a dose of 1e15 cm^{-2} and at a beam current of 25nA/cm^2 and then annealed at 750°C in a flowing N_2 ambient.
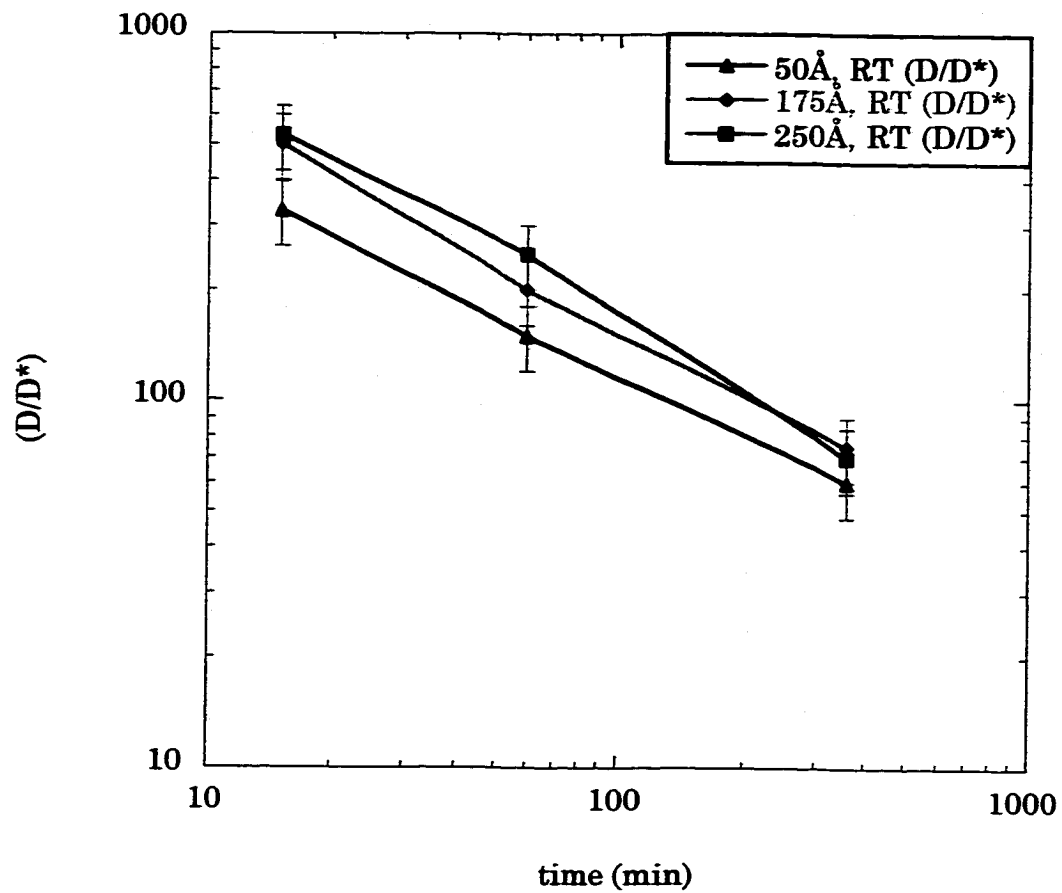
D/D* vs. time (RT Implant, higher dose rate)
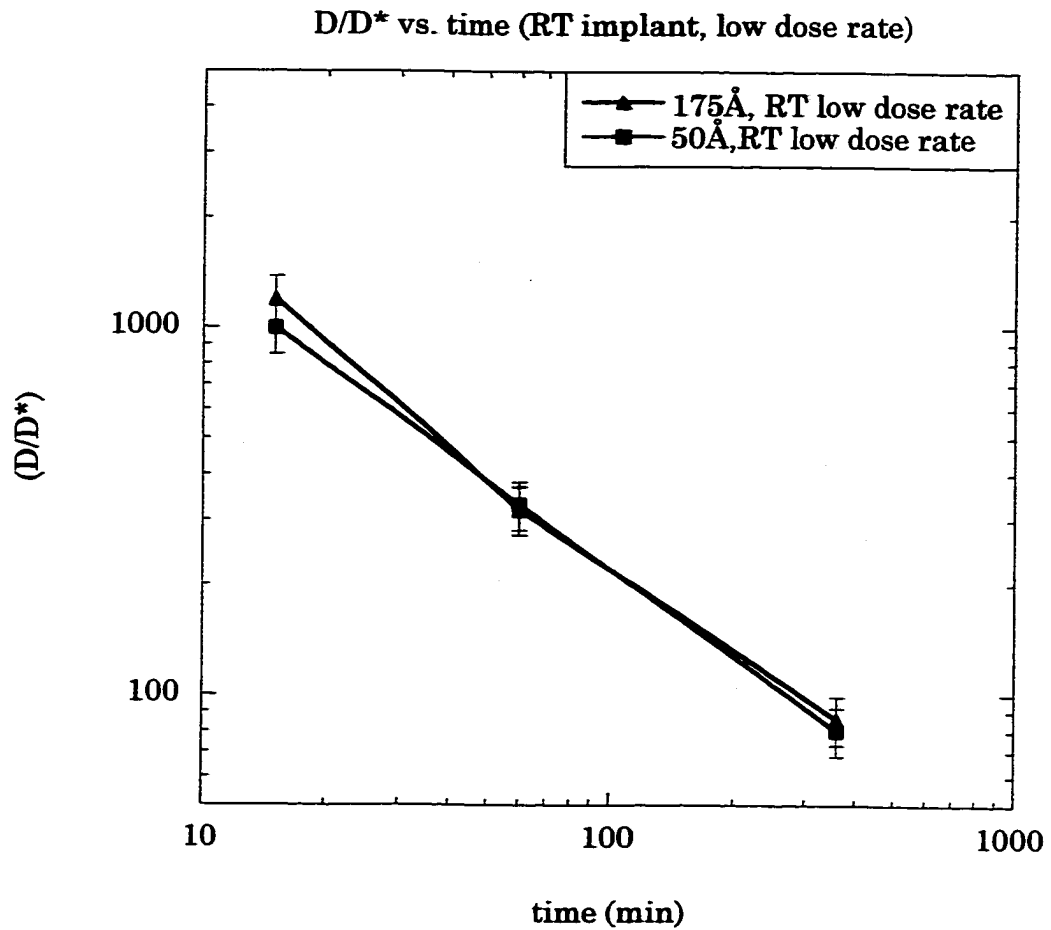
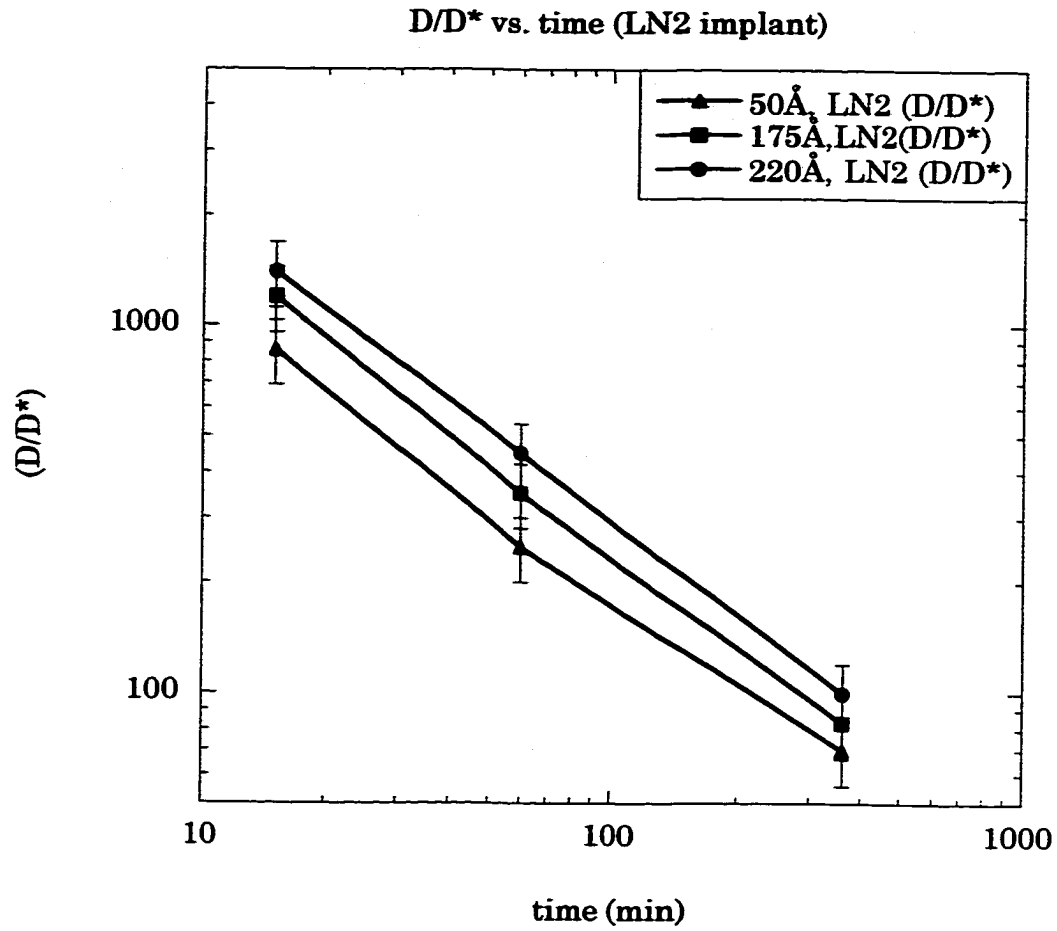Figure 4.5 Comparison of boron diffusivity enhancements for samples implanted at room temperature with 10 keV Si$^+$ ions to a dose of 1e15 cm^{-2} and at a beam current of 5μA/cm^2 and then annealed at 750°C in a flowing N$_2$ ambient.

D/D* vs. time (RT implant, low dose rate)

Figure 4.6 Comparison of boron diffusivity enhancements for samples implanted at room temperature with 10 keV Si^+ ions to a dose of 1e15 cm^{-2} and at a beam current of 25nA/cm^2 and then annealed at 750°C in a flowing N_2 ambient.

D/D* vs. time (LN2 implant)

Figure 4.7 Comparison of boron diffusivity enhancements for samples implanted at liquid nitrogen temperature (77K) with 10 keV Si$^+$ ions to a dose of 1e15 cm^{-2} and at a beam current of 25nA/cm^2 and then annealed at 750°C in a flowing N$_2$ ambient.
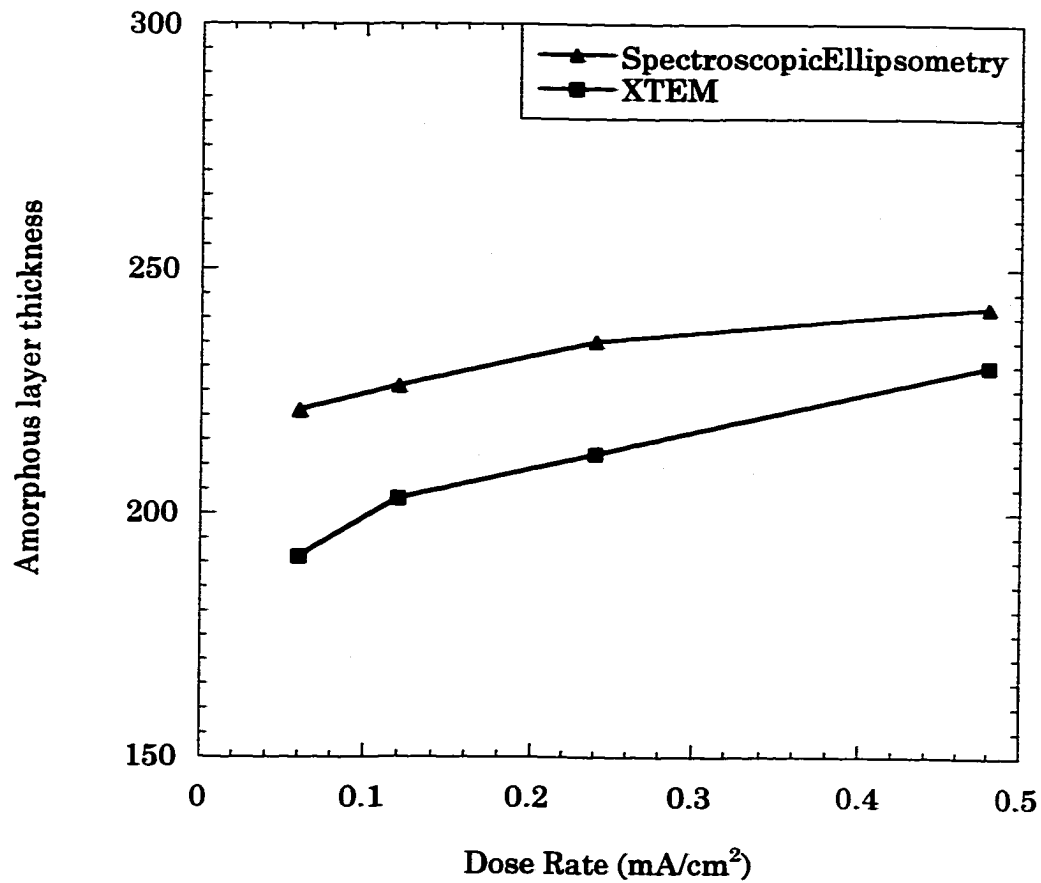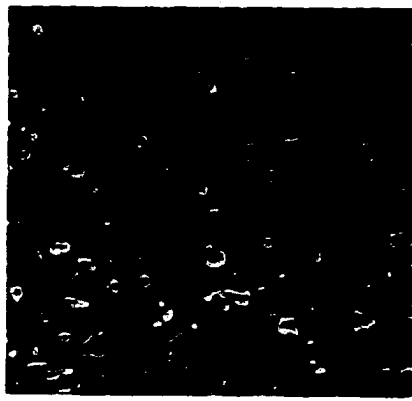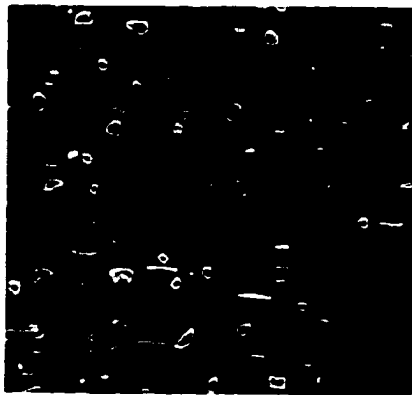
Figure 4.8 Comparison of amorphous layer thicknesses as measured by XTEM and spectroscopic ellipsometry. Results are plotted as a function of dose rate for 10 keV Si^+ implant to a dose of 1e15 cm^{-2} done at room temperature.
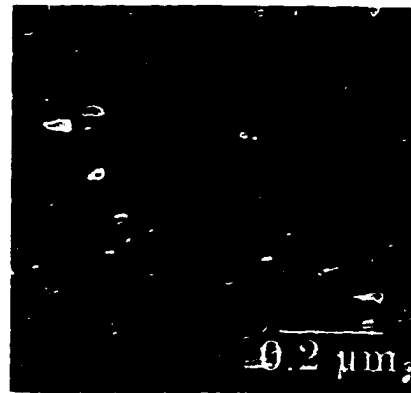
0.06 mA/cm²   0.12 mA/cm²

0.24 mA/cm²   0.48 mA/cm²

a) 15 min.

Figure 4.9 PTEM micrographs of the end-of-range damage as a function of dose rate. Samples were implanted at room temperature with 10 keV Si^+ ions to a dose of 1e15 cm^{-2} and then annealed at 750°C in a flowing N_2 ambient for various times.

0.06 mA/cm²

0.12 mA/cm²

0.24 mA/cm²

0.48 mA/cm²

b) 90 min.

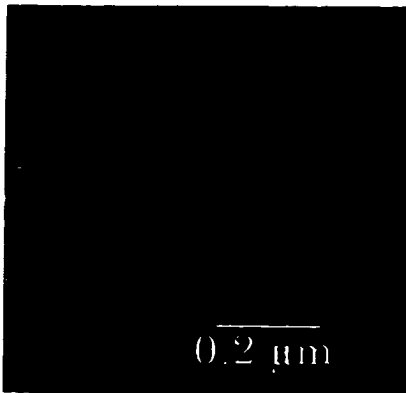Figure 4.9 (contd.) PTEM micrographs of the end-of-range damage as a function of dose rate. Samples were implanted at room temperature with 10 keV Si⁺ ions to a dose of 1e15 cm⁻² and then annealed at 750°C in a flowing N₂ ambient for various times.
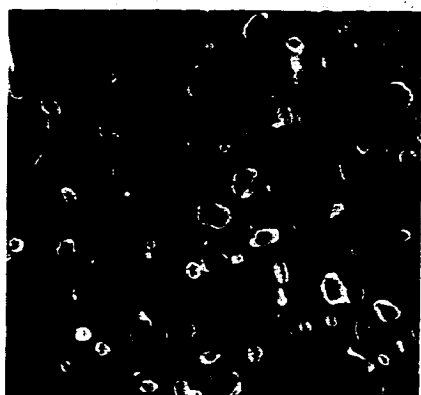
0.06 mA/cm²

0.12 mA/cm²

0.24 mA/cm²
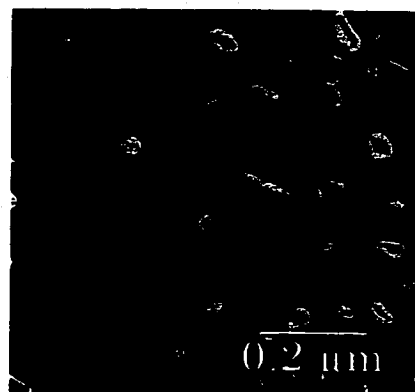
0.48 mA/cm²

c) 360 min.

Figure 4.9 (contd.) PTEM micrographs of the end-of-range damage as a function of dose rate. Samples were implanted at room temperature with 10 keV Si⁺ ions to a dose of 1e15 cm⁻² and then annealed at 750°C in a flowing N₂ ambient for various times.
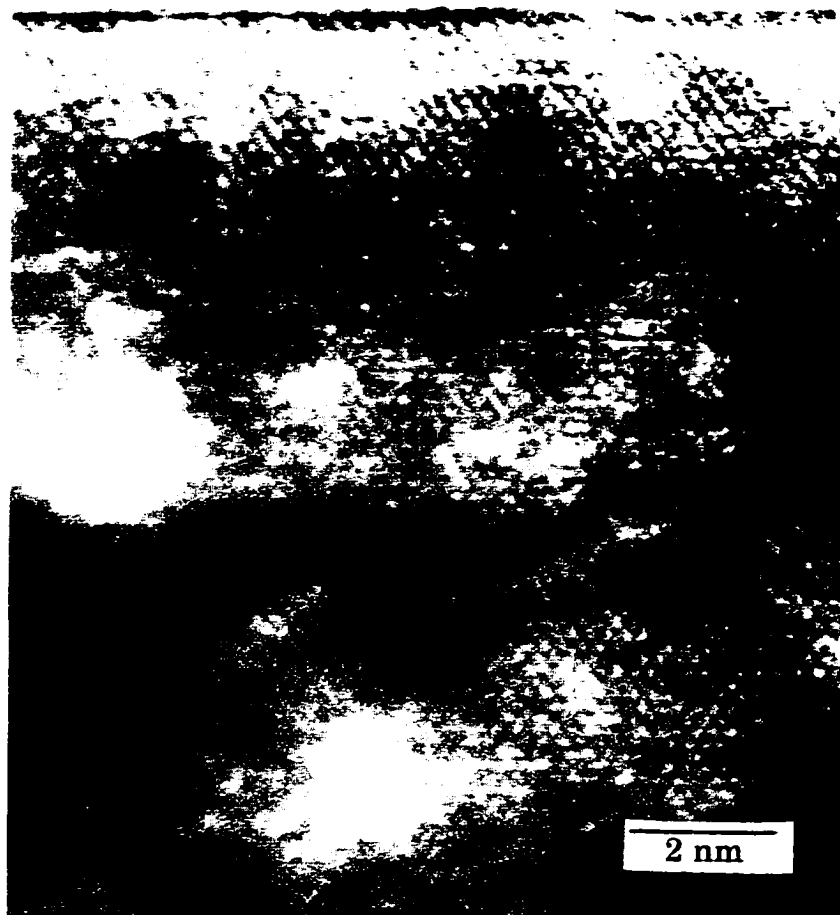
Figure 4.10 XTEM micrograph showing zig-zag {311} defects in (100) Si implanted with 10 keV Si^+ ions to a dose of 1e15 cm^{-2} at room temperature and a dose rate of 5 $\mu A/cm^2$. The amorphous layer thickness was reduced to 50Å by CMP prior to a 750°C, 15 min anneal in flowing N_2.

(a) EOR loops

Figure 4.11 Comparison of defect densities as a function of time and initial amorphous layer depth for samples implanted at room temperature with 10 keV Si^+ ions to a dose of 1e15 cm^{-2} and at a beam current of 5μA/cm² and then annealed at 750°C in a flowing N_2 ambient.

(b) {311} defects

Figure 4.11 (contd.) Comparison of defect densities as a function of time and initial amorphous layer depth for samples implanted at room temperature with 10 keV Si+ ions to a dose of 1e15 cm-2 and at a beam current of 5μA/cm2 and then annealed at 750°C in a flowing N2 ambient.
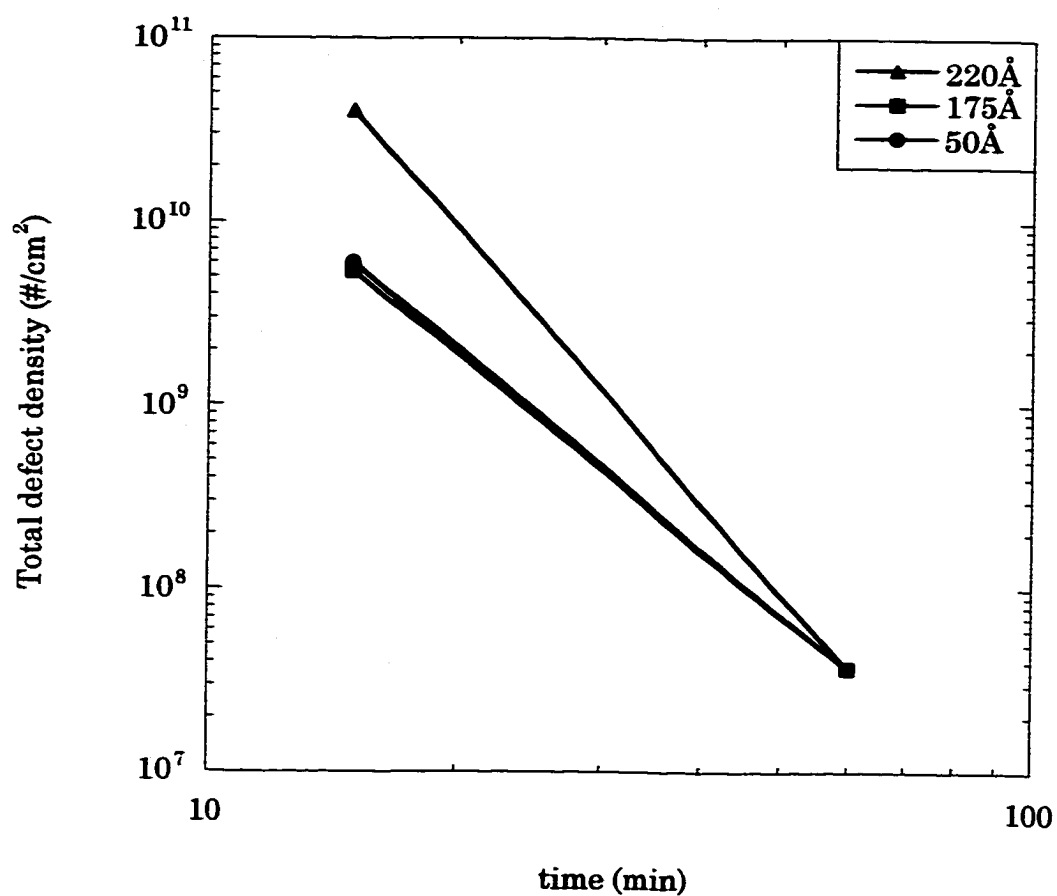
Figure 4.12 Comparison of total defect densities as a function of time and initial amorphous layer depth for samples implanted at LN_2 temperature (77K) with 10 keV Si^+ ions to a dose of 1e15 cm^{-2} and at a beam current of 25nA/cm^2 and then annealed at 750°C in a flowing N_2 ambient.
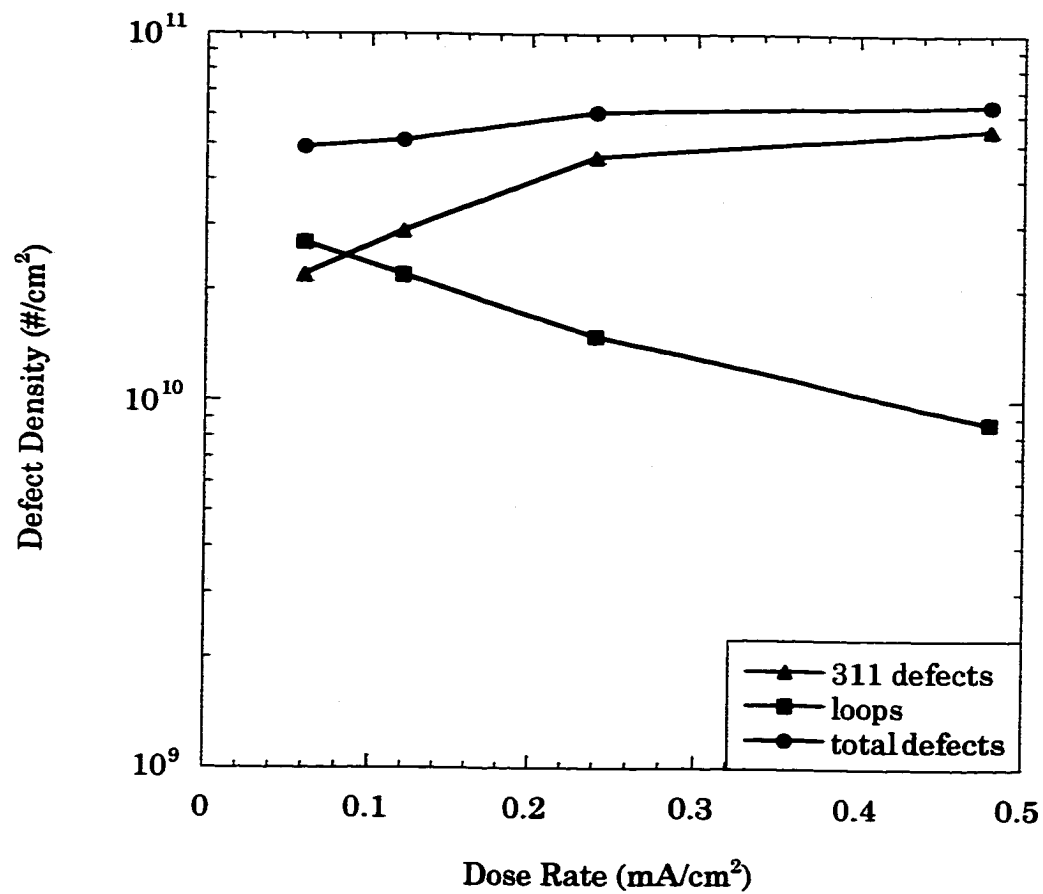
Figure 4.13 Comparison of defect densities as a function of implant dose rate for samples implanted at room temperature with 10 keV Si$^+$ ions to a dose of 1e15 cm^{-2} and then annealed at 750°C in a flowing N$_2$ ambient.
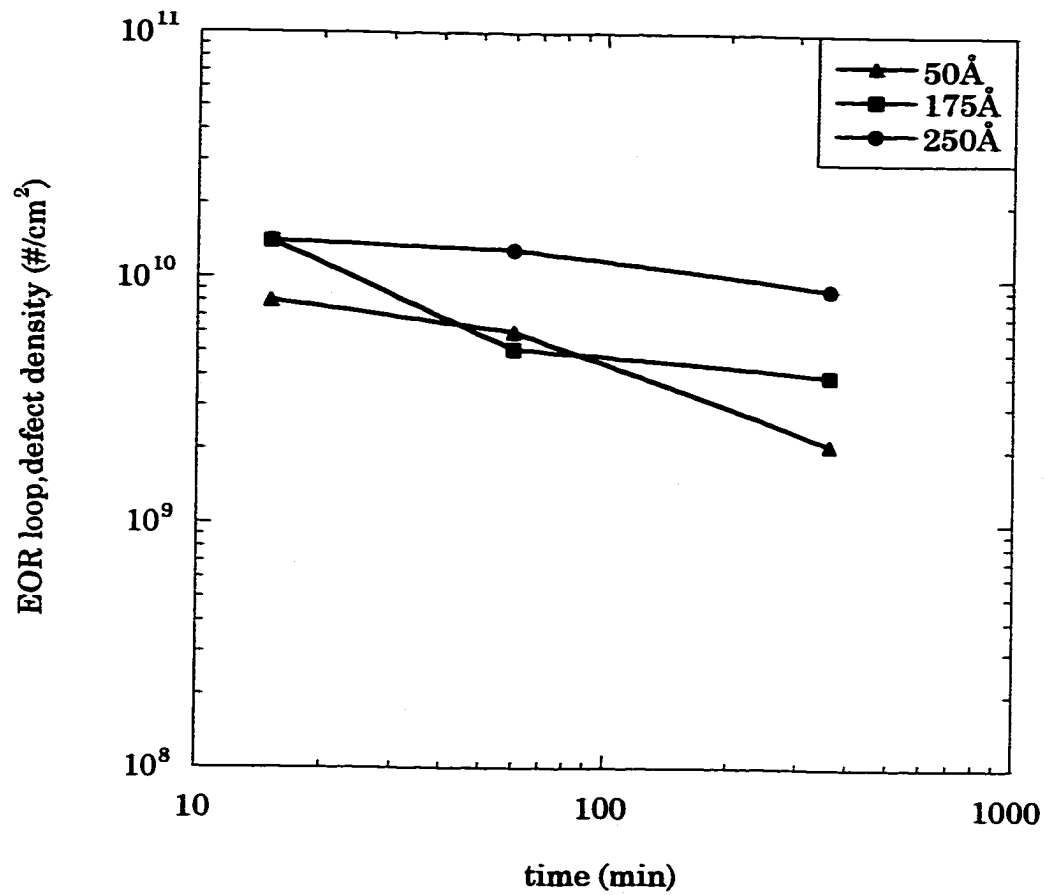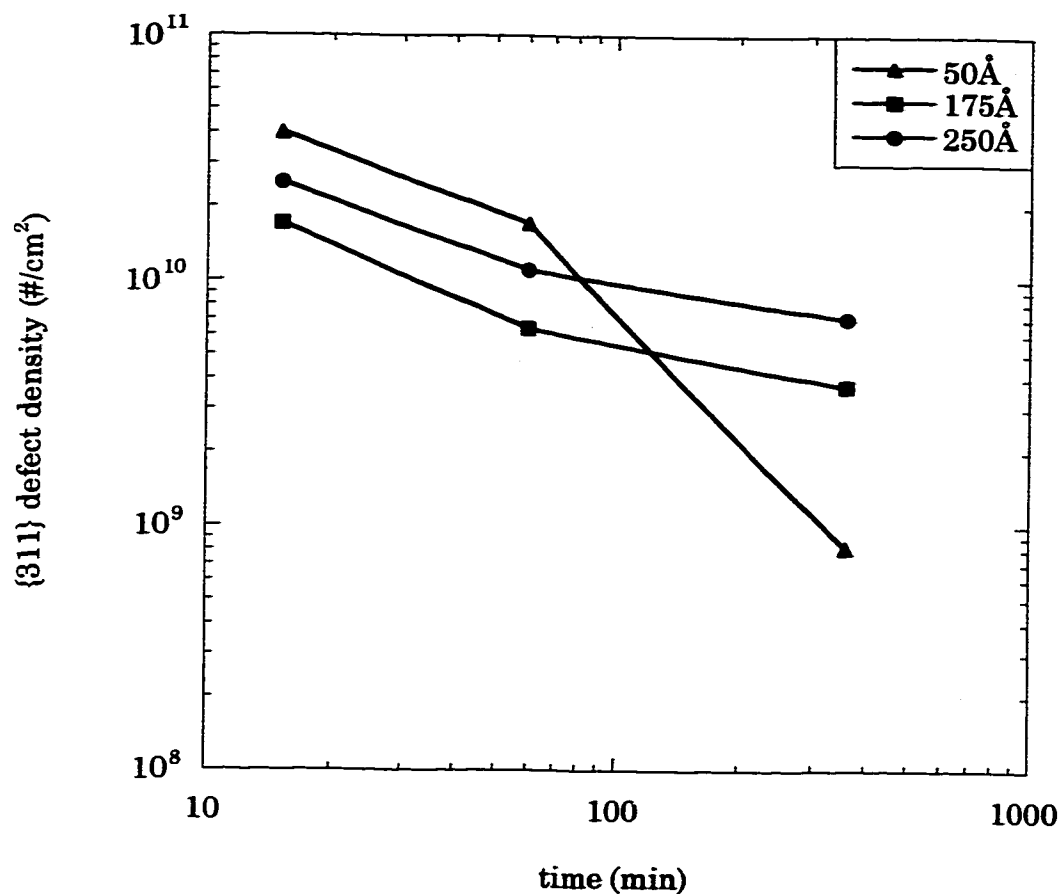
Figure 4.14 Comparison of trapped interstitial dose as a function of implant dose rate for samples implanted at room temperature with 10 keV Si$^+$ ions to a dose of 1e15 cm^{-2} and then annealed at 750°C in a flowing N$_2$ ambient.

(a) {311} defects and loops

Figure 4.15 Comparison of defect densities as a function of time and dose rate fro samples implanted at room temperature with 10 keV Si^+ ions to a dose of $1e15/cm^2$ and annealed at 750°C in a flowing N_2 ambient. b) total defects

(b) total defects

Figure 4.15 (contd.) Comparison of defect densities as a function of time and dose rate fro samples implanted at room temperature with 10 keV Si^+ ions to a dose of 1e15/cm^2 and annealed at 750°C in a flowing N_2 ambient.
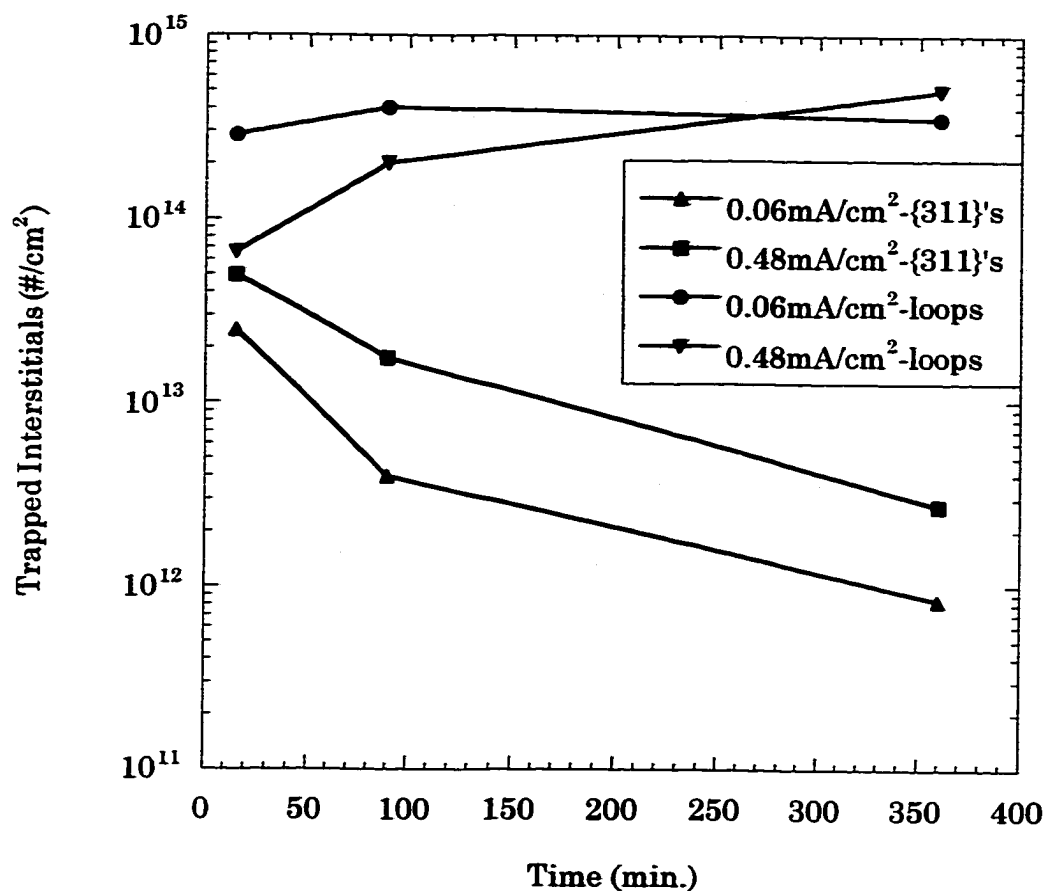
(a) in {311} defects and loops

Figure 4.16 Comparison of trapped interstitial dose as a function of time and dose rate for samples implanted at room temperature with 10 keV Si$^+$ ions to a dose of 1e15/cm^2 and then annealed in a flowing N$_2$ ambient.
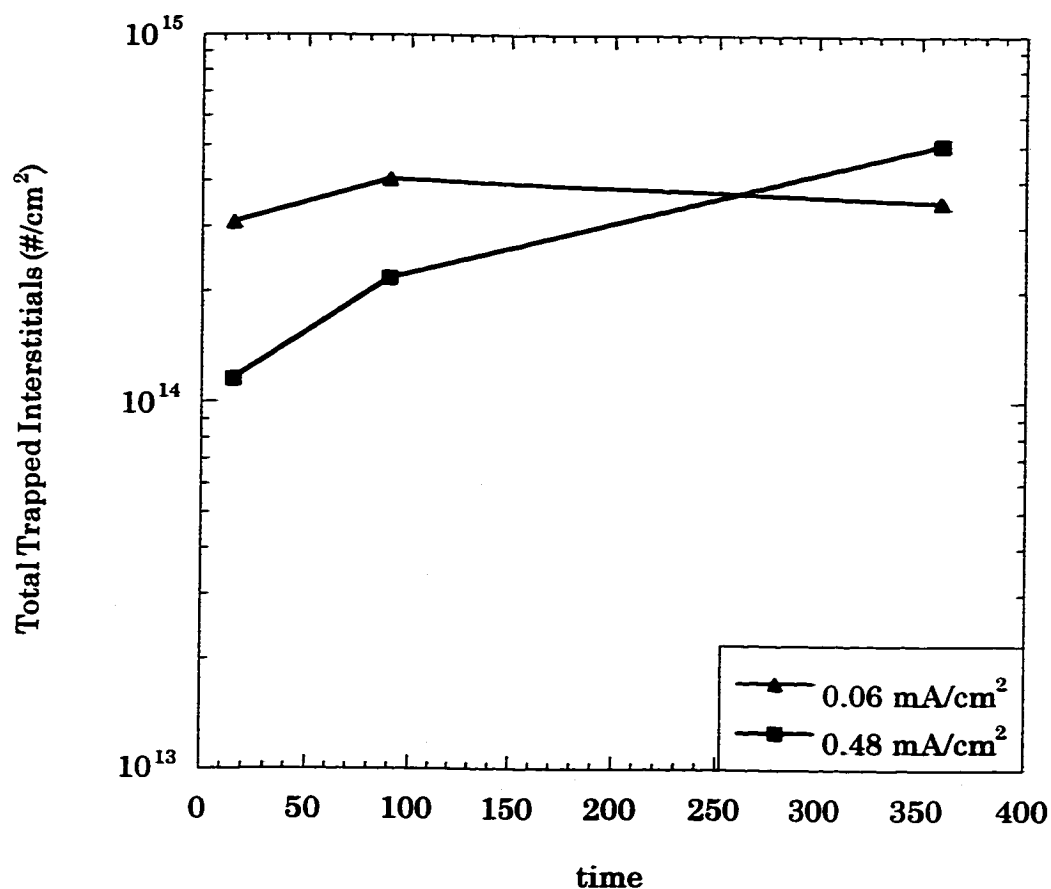
(b) total trapped interstitial dose
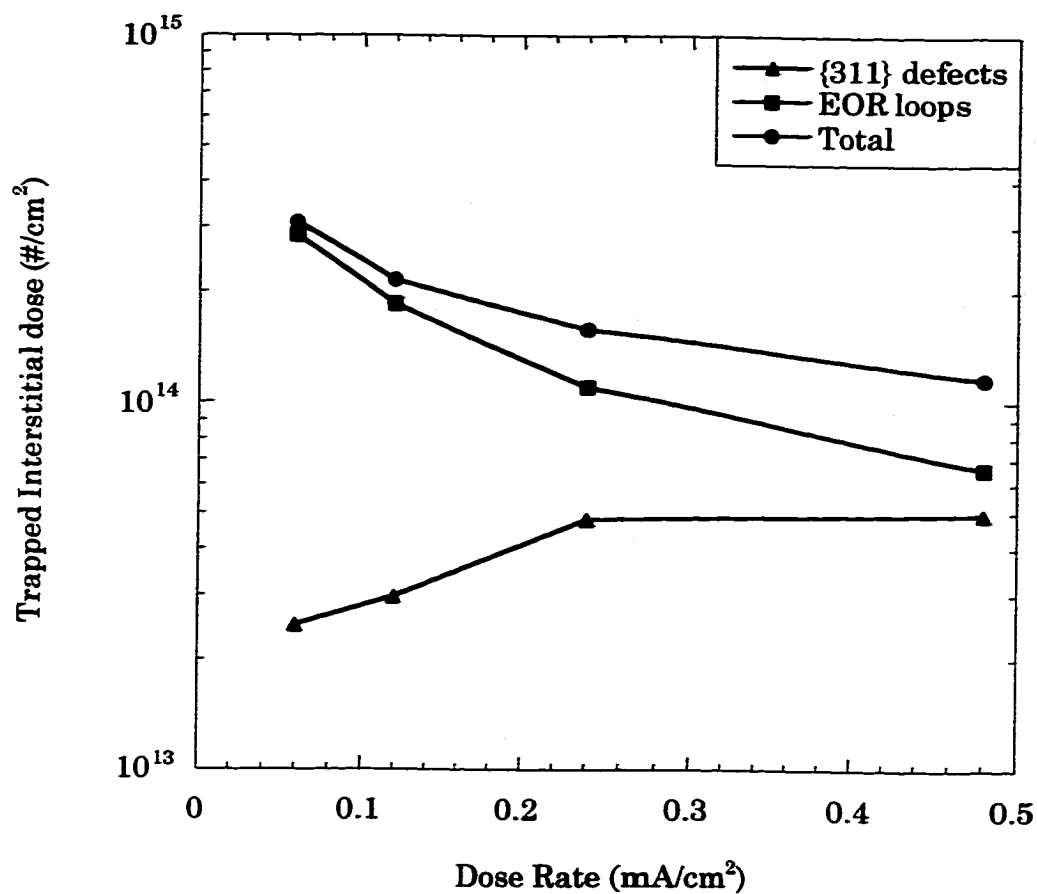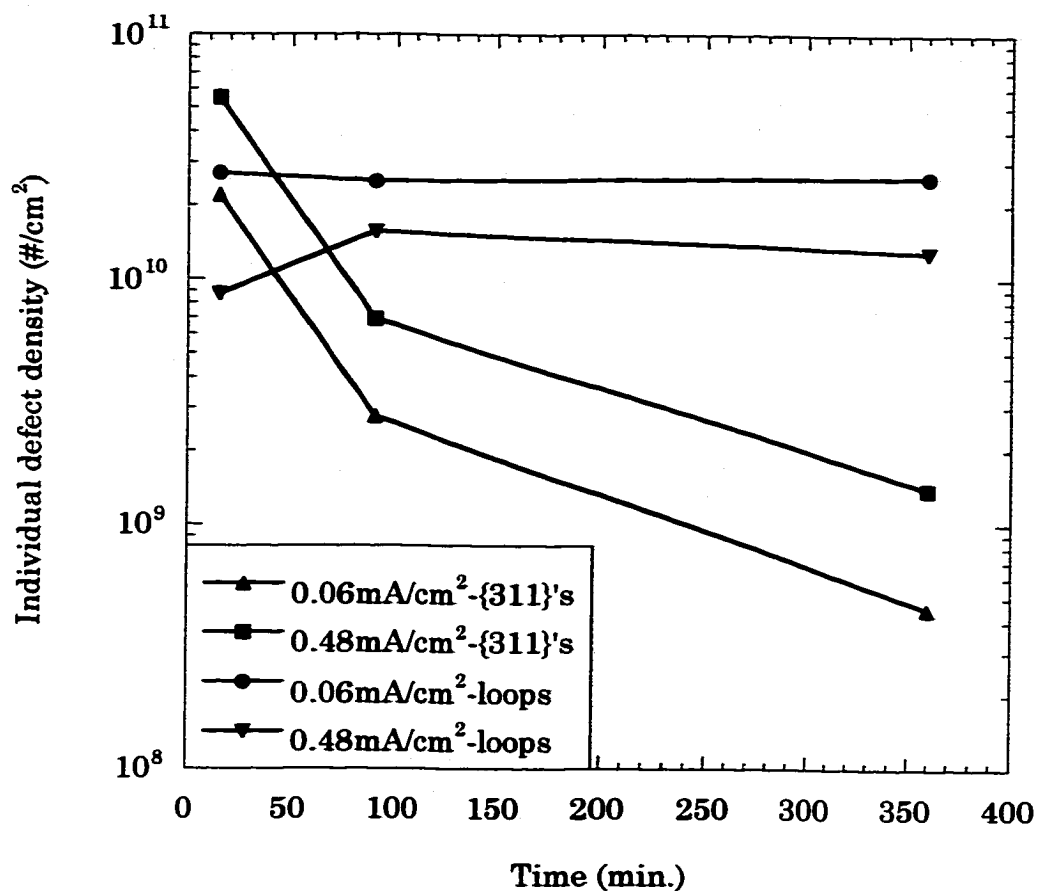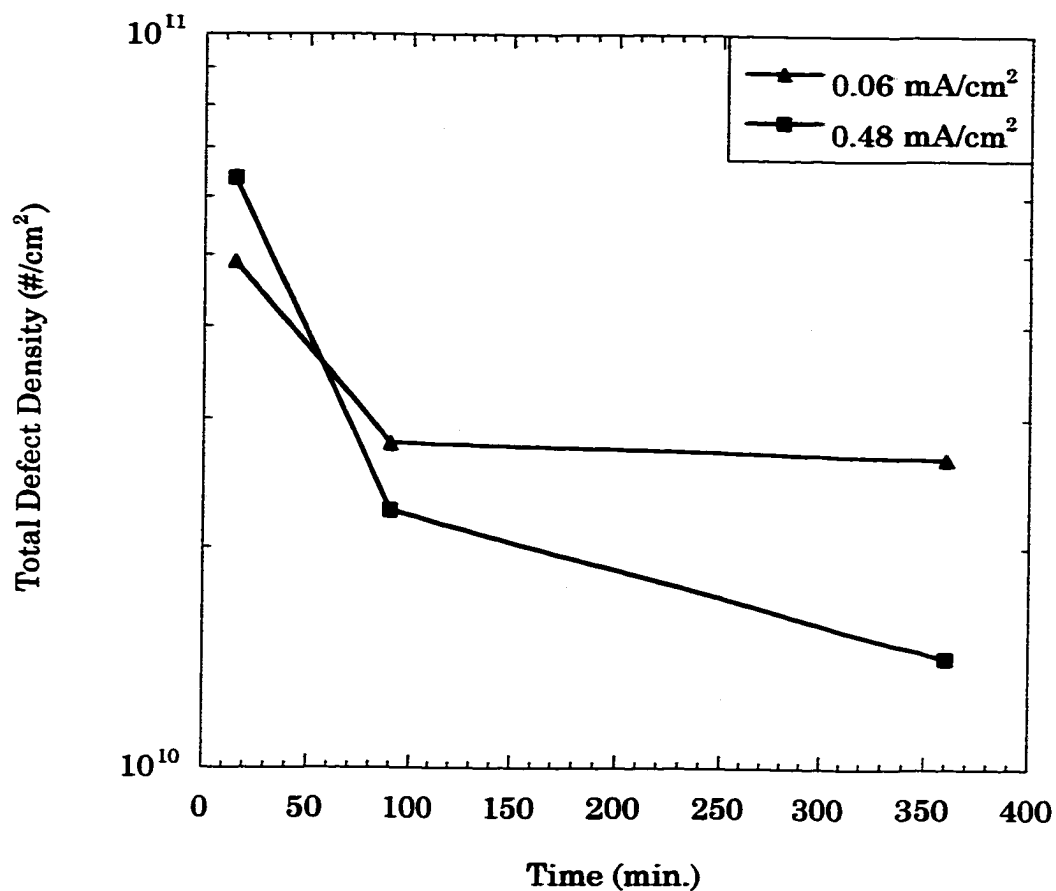
Figure 4.16 (contd.) Comparison of trapped interstitial dose as a function of time and dose rate for samples implanted at room temperature with 10 keV Si^+ ions to a dose of 1e15/cm^2 and then annealed in a flowing N_2 ambient.

CHAPTER 5
CONCLUSIONS AND RECOMMENDATIONS

The silicon IC manufacturing industry must be able to accurately predict and control dopant diffusion in order to maintain the pace of decreasing device dimensions. In order to thoroughly understand dopant diffusion phenomena in silicon, knowledge of the point defect population as well as the sources and sinks of point defects during the IC proccessing steps is required. Since IC manufacturing is becoming increasingly dependent on device design using process simulators, models based on the physical mechanisms of point defect perturbances need to be developed. This will allow the simulators to be predictive at device sizes below where current measurement is possible. These physically based models require an understanding of fundamental issues such as:

1. intrinsic point defect populations, including the formation and migration energies.

2. excess point defect evolution, including extended defect and cluster formation and dissolution.

3. thermal processing of silicon in inert and reactive ambients (e.g. oxidation and nitridation) including surface and interface recombination and point defect perturbations.

121

This dissertation has focused on gaining insight into point defect phenomena: the equilibrium concentration of silicon interstitials in a bulk crystal and effect of surface proximity on defect evolution. Since diffusion of point defects takes place through the interaction of the dopant atoms with native point defects, it is obvious that for a complete understanding the point defect parameters, such as the diffusivity and equilibrium concentration, must be known. The use of extended defects and dopant marker layers provides a way to study point defects and thus add to the information already available.

In Chapter 3 an experimental method to determine the value of the equilibrium concentration of self-interstitials (C_I^*) in silicon was studied. This experiment was based on comparing dopant diffusion of boron marker layers to the capture of interstitials in a second sample set by a type II dislocation loop layer after identical implants and anneals. Since the results of the two experiments are related to C_I/C_I^* and C_I respectively, the C_I^* value can then be calculated. By conducting this experiment at three different temperatures, 685, 750 and 815°C, and at various anneal times, a value of $2 \times 10^{27} \, e^{-2.7eV/kT} \, cm^{-3}$ was obtained for C_I^*. The assumptions that went into the determination of this value were examined by comparing the dissolution of the intermediary {311} defects in both sets of samples and also by studying quantitatively the recombination of interstitials at the sample surface. The discrepancy in the value of C_I^* between these results and the theoretical

results of Morehead[86] and Bracht et al.[65] is believed to be due to the presence of interstitial traps which lead to a reduced and thus effective diffusivity of the boron marker layers. Thus, the boron marker layers account for only a fraction of the interstitials in their vicinity leading to a C_I^* value that is larger. This value should be divided by the ratio of trapped-to-free interstitials thus reducing it to closer to the theoretical value.

Thus the nature of the material being used in the experiment can significantly influence the behavior of point defects and dopant during thermal processing. Differences in boron diffusion in silicon grown by molecular beam epitaxy (MBE) and atomspheric pressure chemical vapor deposition (APCVD) have been reported.[85] This material-dependent behavior of dopant diffusion makes it a potentially powerful tool to characterize the quality of epitaxial layers.

Surface effects on the formation and evolution of extended defects and also on transient enhanced diffusion (TED) is an important area of research for shallow junction technology. A study of the effect of amorphous layer thickness i.e. the proximity of the surface to the end-of-range damage region and implant parameters (temperature and dose rate) on extended defect evolution is presented in Chapter 4 of this dissertation. The results presented therein suggest that the variation seen in defect morphology as the amorphous layer thickness is reduced is due to a surface induced strain or image force that extends down to the damage region for the thinnest

amorphous layers. If this is the case, then changing the surface stresses prior to furnace annealing by deposition of a low temperature (<450°C so the amorphous layer dose not regrow) oxide or nitride thin film should affect the defect evolution. This experiment should be of practical and theoretical benefit to process engineers and simulators.

REFERENCES

(1) P. A. Packan, Ph.D. Dissertation, Stanford University, 1991.

(2) Semiconductor Industry Association "The National Technology Roadmap for Semiconductor Technology Needs" 1997.

(3) W. Taylor, B. P. R. Marioton, T. Y. Tan, U. Gosele, Radiation Effects and Defects in Solids, 111&112, 131, 1989.

(4) J. Zhu, L. H. Yang, C. Mailhiot, T. Diaz de la Rubia, G. H. Gilmer, Nuclear Instruments and Methods in Physics Research B, 102, 29, 1995.

(5) M. -J. Cartula, T. Diaz de la Rubia, L. A. Marques, G. H. Gilmer, Physical Review B, 54, 16683, 1996.

(6) G. H. Gilmer, T. Diaz de la Rubia, D. M. Stock, M. Jaraiz, Nuclear Instruments and Methods in Physics Research B, 102, 247, 1995.

(7) C. D. Meekison, C. Hill, C. D. Marsh, D. P. Gold, D. R. Boys, G. R. Booker, Institute of Physics Conference Series, 117, 197, 1991.

(8) M. Omri, C. Bonafos, A. Claverie, A. Nejim, F. Cristiano, D. Alquier, A. Martinez, N. E. B. Cowern, Nuclear Instruments and Methods in Physics Research B, 120, 5, 1996.

(9) E. Ganin, A. Marwick, MRS Symposium Proceedings, 147, 13, 1989.

(10) A. Agarwal, H. -J. Gossmann, D. J. Eaglesham, L. Pelaz, D. C. Jacobson, T. E. Haynes, Yu. E. Erokhin, Applied Physics Letters, 71, 3141, 1997.

(11) K. Moller, K. S. Jones, M. E. Law, Applied Physics Letters, 72, 2547, 1998.

(12) K. S. Jones, Ph. D. Dissertation, University of California, 1987.

(13) M. D. Giles, Journal of the Electrochemical Society, 138, 1160, 1991.

(14) P. M. Fahey, P. B. Griffin, J. D. Plummer, Reviews of Modern Physics, 61, 289, 1989.

(15) W. Frank, U. Gösele, H. Mehrer, A. Seeger In *Diffusion in Crystalline Solids*; A. S. Nowick and G. G. Libowitz, eds.; Academic Press, pp. 63, 1984.

(16) T. Y. Tan, U. Gosele, Applied Physics A, 37, 1, 1985.

(17) S. M. Hu, Materials Science and Engineering, R13, 105, 1994.

(18) N. E. B. Cowern, Applied Physics Letters, 64, 2646, 1994.

(19) K.S. Jones, G.A. Rozgonyi In *Rapid Thermal Processing Science and Technology*; Academic Press, pp. 123, 1993.

(20) W. Vandervorst, D. C. Houghton, F. R. Shephard, M. L. Swanson, H. H. Plattner, G. J. C. Carpenter, Canadian Journal of Physics, 63, 863, 1985.

(21) K.S. Jones, D.K. Sadana, S. Prussin, J. Washburn, E.R. Weber, W.J. Hamilton, Journal of Applied Physics, 63, 1414, 1988.

(22) D. Venables, K. S. Jones, Nuclear Instruments and Methods in Physics Research B, 59/60, 1019, 1991.

(23) D. J. Eaglesham, A. Agarwal, T. E. Haynes, H. -J. Gossmann, D. C. Jacobson, J. M. Poate, Nuclear Instruments and Methods in Physics Research B, 120, 1, 1996.

(24) A. Claverie, L. Laanab, C. Bonafos, C. Bergaud, A. Martinez, D. Mathiot, Nuclear Instruments and Methods in Physics Research B, 96, 202, 1995.

(25) J.K. Listebarger, K.S. Jones, J.A. Slinkman, Journal of Applied Physics, 73, 4815, 1993.

(26) H. S. Chao, Ph. D. Dissertation, Stanford University, 1997.

(27) K. S. Jones, L. H. Zhang, V. Krishnamoorthy, M. Law, D. S. Simons, P. Chi, L. Rubin, R. G. Elliman, Applied Physics Letters, 68, 2672, 1996.

(28) J. K. Listebarger, M. S. Thesis, University of Florida, 1994.

(29) K.S. Jones, J. Liu, L. Zhang, V. Krishnamoorthy, R.T. DeHoff, Nuclear Instruments and Methods in Physics Research B, 106, 227, 1995.

(30) S. Takeda, M. Kohyama, Institute of Physics Conference Series, 134, 33, 1993.

(31) I.G. Salisbury, M.H. Loretto, Philosophical Magazine A, 39, 317, 1979.

(32) E. Nes, J. Washburn, Journal of Applied Physics, 42, 3559, 1971.

(33) J. Narayan, J. Fletcher, MRS Symposium Proceedings, 2, 191, 1981.

(34) M. D. Matthews, S. J. Ashby, Philosophical Magazine A, 27, 1313, 1973.

(35) K. Seshan, J. Washburn, Radiation Effects, 14, 267, 1975.

(36) J. Desroches, M. S. Thesis, University of Florida, 1997.

(37) J. Liu, V. Krishnamoorthy, H. -J. Gossmann, L. Rubin, M. E. Law, K. S. Jones, Journal of Applied Physics, 81, 1656, 1997.

(38) D.J. Eaglesham, P.A. Stolk, H.-J. Gossmann, J.M. Poate, Applied Physics Letters, 65, 2305, 1994.

(39) C. A. Ferreira Lima, A. Howie, Philosophical Magazine, 34, 1057, 1976.

(40) C. Carter, W. Maszara, D. K. Sadana, G. A. Rozgonyi, J. Liu, J. J. Wortman, Applied Physics Letters, 44, 459, 1984.

(41) T. Sands, J. Washburn, R. Gronsky, W. Maszara, D. K. Sadana, G. A. Rozgonyi, Applied Physics Letters, 45, 982, 1984.

(42) D. K. Sadana, J. Washburn, G. R. Booker, Philosophical Magazine B, 46, 611, 1982.

(43) B. J. Masters, J. M. Fairfield, B. L. Crowder, Radiation Effects, 6, 57, 1970.

(44) D. K. Brice, Journal of Applied Physics, 62, 4421, 1987.

(45) N. R. Wu, D. K. Sadana, J. Washburn, Applied Physics Letters, 44, 782, 1984.

(46) P. A. Stolk, H. -J. Gossmann, D. J. Eaglesham, J. M. Poate, Nuclear Instruments and Methods in Physics Research B, 96, 187, 1995.

(47) A. N. Larsen, P. Kringhøj, J. L. Hansen, S. Y. Shiryaev, MRS Symposium Proceedings, 378, 285, 1995.

(48) D. J. Eaglesham, P. A. Stolk, H. -J. Gossmann, T. E. Haynes, J. M. Poate, Nuclear Instruments and Methods in Physics Research B, 106, 191, 1995.

(49) S. Bharatan, J. Desroches, K. S. Jones In *Materials and Process Characterization of Ion Implantation*; 1st ed.; M. I. Current and C. B. Yarling, eds., Ion Beam Press, Austin, TX, pp. 488, 1997.

(50) L. Laanab, C. Bergaud, M. M. Faye, J. Faure, A. Martinez, A. Claverie, MRS Symposium Proceedings, 279, 381, 1993.

(51) P. Boher, J. L. Stehle, J. P. Piel, M. Fried, T. Lohner, O. Polgar, N. Q. Khanh, I. Barsony, Nuclear Instruments and Methods in Physics Research B, 112, 160, 1996.

(52) T. Lohner, M. Fried, J. Gyulai, K. Vedam, N. V. Nyugen, L. J. Hanekamp, A. van Silfhout, Thin Solid Films, 223, 117, 1993.

(53) S. B. Herner, B. P. Gila, K. S. Jones, H. -J. Gossmann, J. M. Poate, H. S. Luftman, Journal of Vacuum Science and Technology B, 14, 3593, 1996.

(54) R. Raman, M. E. Law, V. Krishnamoorthy, K. S. Jones, Applied Physics Letters, 74, 700, 1999.

(55) M. E. Law, Florida Object Oriented Process Simulator, Gainesville, FL, 1999.

(56) J. A. Woollam Co. Inc. "Guide to Using WVASE32™".

(57) P.A. Packan, J. D. Plummer, Appl. Phys. Lett., 56, 1787, 1990.

(58) P. A. Stolk, H. -J. Gossmann, D. J. Eaglesham, D. C. Jacobson, J. M. Poate, H. S. Luftman, Applied Physics Letters, 66, 568, 1995.

(59) H. -J. Gossmann, C. S. Rafferty, P. A. Stolk, D. J. Eaglesham, G. H. Gilmer, J. M. Poate, H. -H. Vuong, T. K. Mogi, M. O. Thompson, MRS Symposium Proceedings, 389, 3, 1995.

(60) B. J. Masters, J. M. Fairfield, Applied Physics Letters, 8, 280, 1966.

(61) C. Boit, F. Lau, R. Sittig, Applied Physics A, 50, 197, 1990.

(62) G. B. Bronner, J. D. Plummer, Journal of Applied Physics, 61, 5286, 1987.

(63) S. Mantovani, F. Nava, C. Nobili, G. Ottaviani, Physical Review B, 33, 5536, 1986.

(64) H. Zimmermann, H. Ryssel, Applied Physics A, 55, 121, 1992.

(65) H. Bracht, N. A. Stolwijk, H. Mehrer, Physical Review B, 52, 16542, 1995.

(66) H. G. A. Huizing, Ph.D. Dissertation, 1996.

(67) National Institutes of Health, NIH Image v 1.62 developed at the U. S. National Institutes of Health and available at http://rsb.info.nih.gov/nih-image

(68) J. Liu, M.E. Law, K.S. Jones, Solid State Electronics, 38, 1305, 1995.

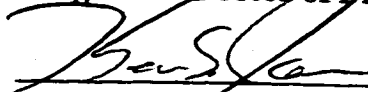(69) K.S. Jones, D. Venables, Journal of Applied Physics, 69, 2931, 1991.

(70) L. Lanaab, C. Bergaud, M. M. Faye, J. Faure, A. Martinez, MRS Symposium Proceedings, 279, 381, 1993.

(71) M. Servidori, Z. Sourek, S. Solmi, Journal of Applied Physics, 62, 1723, 1987.

(72) R. Y. S. Huang, Ph. D. Dissertation, Stanford University, 1994.

(73) H.L. Meng, S. Prussin, M.E. Law, K.S. Jones, Journal of Applied Physics, 73, 955, 1993.

(74) K. S. Jones, J. Chen, S. Bharatan, J. Jackson, L. Rubin, M. Puga-Lambers, D. Venables, Journal of Electronic Materials, 26, 1361, 1997.

(75) J. Liu, Ph.D. Dissertation, University of Florida, 1996.

(76) N. A. Stolwijk, B. Schuster, J. Hölzl, Applied Physics A, 33, 133, 1984.

(77) U. Gösele, F. F. Morehead, W. Frank, A. Seeger, Applied Physics Letters, 38, 157, 1981.

(78) T. Y. Tan, U. Gösele, F.F. Morehead, Applied Physics A, 42, 690, 1983.

(79) U. Gösele, A. Plößl, T. Y. Tan, Proceedings of the Electrochemical Society, 96-4, 309, 1996.

(80) S. Chakravarthi, S. T. Dunham, MRS Symposium Proceedings, 469, 47, 1997.

(81) K. Taniguchi, D. A. Antoniadis, Y. Matsushita, Applied Physics Letters, 42, 961, 1983.

(82) D. A. Antoniadis, Journal of the Electrochemical Society, 129, 1093, 1982.

(83) S. M. Hu, Applied Physics Letters, 43, 449, 1983.

(84) P. A. Stolk, D. J. Eaglesham, H. -J. Gossmann, J. M. Poate, Applied Physics Letters, 66, 1370, 1995.

(85) K. J. van Oostrum, P. C. Zalm, W. B. de Boer, D. J. Gravesteijn, J. W. F. Maes, Applied Physics Letters, 61, 1513, 1992.

(86) F. F. Morehead, MRS Symposium Proceedings, 104, 99, 1988.

(87) H. -J. Gossmann, G. H. Gilmer, C. S. Rafferty, F. C. Unterwald, T. Boone, J. M. Poate, H. S. Luftman, W. Frank, Journal of Applied Physics, 77, 1948, 1995.

(88) J. Narayan, K. Jagannadham, Journal of Applied Physics, 62, 1694, 1987.

(89) J. Thornton, C. Hill, Semiconductor Science and Technology, 4, 53, 1989.

(90) A. Agarwal, T. E. Haynes, D. J. Eaglesham, H. -J. Gossmann, D. C. Jacobson, J. M. Poate, Yu E. Erokhin, Applied Physics Letters, 70, 3332, 1997.

(91) S. Prussin, G. Z. Pan, P. F. Zhang, Proceedings of the Electrochemical Society, 96-4, 379, 1996.

(92) S. Prussin, personal communication, 1999.

(93) C. Prunier, E. Ligeon, A. Bourret, A. C. Chami, J. C. Oberlin, Nuclear Instruments and Methods in Physics Research B, 17, 227, 1986.

(94) B. Obradovic, G. Wang, Y. Chen, D. Li, C. Snell, A. F. Tasch, UT-MARLOWE 5.0, University of Texas, Austin; Los Alamos National Laboratory, 1999.

(95) L. S. Robertson, A. Lilak, M. E. Law, K. S. Jones, P. Kringhøj, L. M. Rubin, J. Jackson, D. S. Simons, P. Chi, Applied Physics Letters, 71, 3105, 1997.

(96) P. J. Bedrossian, M. -J. Cartula, T. Diaz de la Rubia, Applied Physics Letters, 70, 176, 1997.

BIOGRAPHICAL SKETCH

Sushil Bharatan received his bachelor of technology degree in metallurgical engineering from the Indian Institute of Technology, Bombay, India, in May 1992. He then proceeded to the University of Florida, where he earned a master of science degree in the department of materials science and engineering. His thesis was on the structural characterization of GaN and InGaN alloys grown by metalorganic molecular beam epitaxy. He then continued his education and research at the University of Florida and earned his doctor of philosophy degree in December, 1999.

I certify that I have read this study and that in my opinion it conforms to acceptable standards of scholarly presentation and is fully adequate, in scope and quality, as a dissertation for the degree of Doctor of Philosophy.

Kevin S. Jones, Chairman
Professor of Materials Science
and Engineering

I certify that I have read this study and that in my opinion it conforms to acceptable standards of scholarly presentation and is fully adequate, in scope and quality, as a dissertation for the degree of Doctor of Philosophy.

Robert T. DeHoff
Professor of Materials Science
and Engineering

I certify that I have read this study and that in my opinion it conforms to acceptable standards of scholarly presentation and is fully adequate, in scope and quality, as a dissertation for the degree of Doctor of Philosophy.

Cammy R. Abernathy
Professor of Materials Science
and Engineering

I certify that I have read this study and that in my opinion it conforms to acceptable standards of scholarly presentation and is fully adequate, in scope and quality, as a dissertation for the degree of Doctor of Philosophy.

Stephen J. Pearton
Professor of Materials Science
and Engineering

I certify that I have read this study and that in my opinion it conforms to acceptable standards of scholarly presentation and is fully adequate, in scope and quality, as a dissertation for the degree of Doctor of Philosophy.
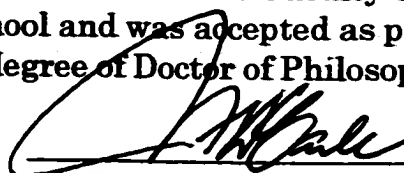
Mark E. Law
Professor of Electrical and
   Computer Engineering

This dissertation was submitted to the Graduate Faculty of the College of Engineering and to the Graduate School and was accepted as partial fulfillment of the requirements for the degree of Doctor of Philosophy.

December 1999

M. J. Ohanian
Dean, College of Engineering

Winfred M. Phillips
Dean, Graduate School